Structure and magnetocrystalline anisotropy of interlayer modified ultrathin epitaxial magnetite films on MgO(001)

Dissertation (kumulativ)

zur Erlangung des Grades Doktor der Naturwissenschaft (Dr. rer. nat.)
dem Fachbereich Physik der Universität Osnabrück
vorgelegt von

Tobias Schemme, M.Sc.

Osnabrück, November 2016

Contents

1 Introduction

The ongoing miniaturization of charge-based computing devices in accordance with Moore's law leads to an excessive heat generation in such devices due to the high switching currents. A possible solution of these problems are spintronic devices which are not only charge-based but also use the spin degree of freedom of electrons to encode digital bit information [1]. The advantages of these new components would be nonvolatility, increased data processing speed, decreased electric power consumption, and increased integration densities compared with conventional semiconductor devices [2]. One example for such spintronic component is a magnetic tunnel junction (MTJ) [3–6] which primarily consists of two ferro(i)magnetic conducting electrodes, which are separated by a non-magnetic insulating tunnel barrier as illustrated in Fig. 1.1. The tunnel probability through this barrier depends strongly on the relative alignment of

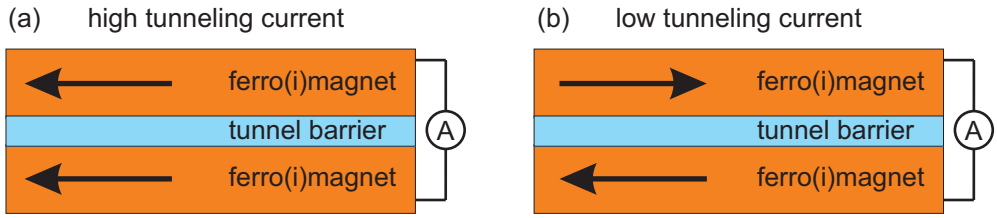

Fig. 1.1: Schematic drawing of a magnetic tunnel junction consisting of two ferrimagnetic electrodes separated by a thin insulating tunnel barrier. If the magnetization in both electrodes is (a) parallel aligned there is a high tunneling probability and thus a high tunneling current. The change to an antiparallel magnetization alignment (b) leads to a low tunneling probability with a low tunneling current.

the magnetization in the magnetic films. If the magnetization in these two films is parallel to each other, there is a high tunneling current for positive tunnel magnetoresistance (TMR) [7], while there is a low tunneling current if the magnetization is antiparallel to each other. Since the magnetization is correlated with the spin orientation of the electrons, the different tunneling probabilities can be explained by the spin preservation during the tunneling process between the electrodes [8].

In case both ferro(i)magnetic films are comprised of the same material, it is essential to modify the coercive field of one of the films. One way of doing this is to deposit one of the ferro(i)magnetic films on an antiferromagnetic film. The exchange coupling between the ferro(i)magnetic and the antiferromagnetic film induces an exchange bias which shifts the switching field of the ferro(i)magnetic film. Thus, both ferro(i)magnetic films have two different switching fields and the magnetization of the films can be manipulated separately and hence an alternation of the alignment of the magnetization between parallel and antiparallel is possible.

Especially, magnetite is a promising electrode material in MTJs due its half-metallic [9, 10] character and a predicted 100% spin polarization [10] at the Fermi level. An ideal substrate

to grow thin magnetite films with high crystalline quality is magnesium oxide because of the small lattice mismatch of only 0.3 %. In addition, the insulating non-ferromagnetic magnesium oxide can be used as tunnel barrier in a MTJ [11].
Prior studies of the group 'Thin films and interfaces' focused on enhancing the growth and the structural quality of single iron oxide films on magnesium oxide [12–14]. Since the magnetic properties are crucial for spintronic applications, in this thesis the influence of the structure of iron oxides on the magnetic properties has been investigated. Therefore, iron oxide films with different thicknesses grown on iron and NiO interlayers have been prepared to vary the structural properties. Subsequently, the structural and magnetic properties of magnetite have been analyzed.
This cumulative thesis comprises three studies which are published in different scientific journals and one study which will be published soon. The magnetic anisotropy of magnetite thin films related to strain and stoichiometry is presented in Chap. 5. The structure and morphology of epitaxially grown Fe_3O_4/NiO bilayers on magnesium oxide are investigated in Chap. 6. In Chap. 7 the results of the modification of the magnetic properties of magnetite films grown on iron pre-covered magnesium oxide are shown. The last study in Chap. 8 discusses the magnetic properties of an partially oxidized iron system on magnesium oxide.

2 Theoretical background

2.1 Crystals and epitaxy of crystalline thin films

Since the structure of epitaxial thin films is one of the main topics in this thesis, a briefly survey about the structural properties of single crystals and crystalline thin films is given. A detailed description can be found in Refs. [15–17].

2.1.1 Single crystals

A crystal is a solid whose components are periodically arranged in all three spatial directions forming a uniform homogeneous crystal lattice. Due to the periodicity only a repeating basic arrangement of atoms, the unit cell, has to be considered to describe the whole crystal.

The positions of the atoms in the unit cell and the three linear independent translation vectors $\boldsymbol{a}$, $\boldsymbol{b}$, and $\boldsymbol{c}$ describe the crystal structure by giving the spatial repetition of the unit cell. These vectors are also called lattice vectors since they define the shape and spacing of the crystal lattice. The position $\boldsymbol{r_{atom}}$ of any atom in the crystal can be calculated by the sum of its position $\boldsymbol{r_j}$ in the unit cell and a linear combination $\boldsymbol{r_n}$ of the three lattice vectors

$$\boldsymbol{r_{atom}} = \boldsymbol{r_j} + \boldsymbol{r_n} = \boldsymbol{r_j} + u \cdot \boldsymbol{a} + v \cdot \boldsymbol{b} + w \cdot \boldsymbol{c} \ . \tag{2.1}$$

Here, u, v, and w are integer numbers. An example of the positioning of an atom in a two dimensional crystal is shown in Fig. 2.1. Instead of using the lattice vectors the unit cell can be described by the length of the lattice vectors $\boldsymbol{a}$, $\boldsymbol{b}$, and $\boldsymbol{c}$ and the angles α, β, and γ between them.
Crystal symmetries are important to distinguish between different types of crystals. By considering symmetry axes and inversion operations Bravais has shown that there are only 14 types of crystal lattices [18]. The so-called Bravais lattices can be designated to seven crystal systems (cubic, tetragonal, rhombohedral, orthorhombic, hexagonal, monoclinic and triclinic). These crystal systems are explicitly described in literature [19].

Lattice planes

A crystal has different lattice planes which can be indexed by the three Miller indices h, k, l, which are integer values. The Miller indices indicate that the lattice planes intercept the three crystallographic axes defined by the lattice vectors at a/h, b/k, and c/l. If any of the three values is not an integer, all values are multiplied by the smallest common integer multiple (e.g. $(\frac{1}{2}\ \frac{1}{4}\ \frac{1}{2})$ becomes (212). Negative values are usually not preceded by a minus sign but by a bar above the value (e.g. -3 becomes $\bar{3}$).

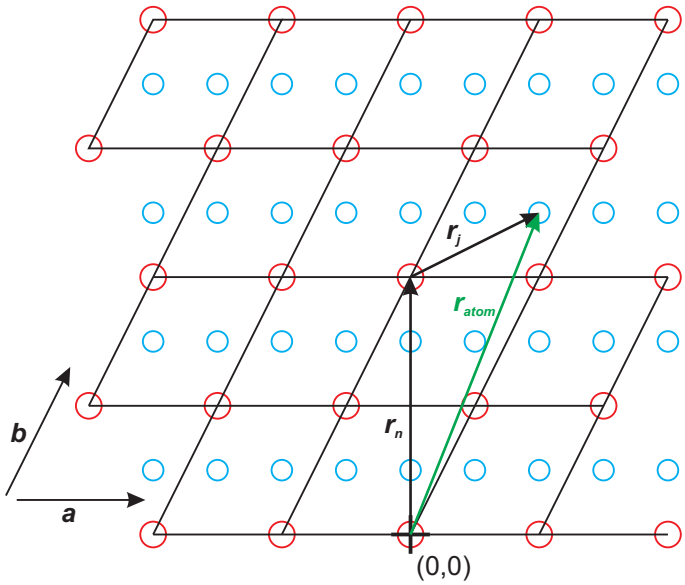

Fig. 2.1: Example of a two dimensional crystal. The position r_{atom} of each atom in the crystal can be simply calculated by summing up the position vector r_n of the unit cell and the position vector r_j of the atom within the unit cell.

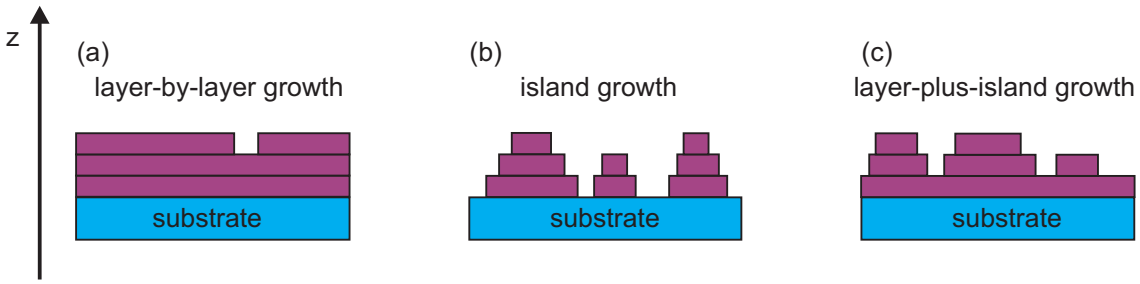

Fig. 2.2: Diagram of the three different possible growth modes: (a) layer-by-layer, (b) island, and (c) layer-plus-island growth.

2.1.2 Epitaxial films

If an overlayer grown on a single crystalline substrate is a crystallographically oriented single crystal it is called epitaxial film. The epitaxial film growth can occur in three different growth modes [17] (cf. Fig. 2.2) described in the following:

- **Layer-by-layer (or Frank-van der Merve) growth:**
  In the case of layer-by-layer growth the bond of the adatoms to the substrate surface is stronger than to other adatoms. Thus, the first atomic layer is completed before a new layer grows on top. If is no critical film thickness the growth mode does not change.
- **Island (or Vollmer-Weber) growth:**
  If the bonds between the adatoms are stronger than between adatoms and the substrate surface, three dimensional islands are formed on the substrate.
- **Layer-plus-island (or Stranski-Krastanov) growth:**
  The layer-plus-island growth is a combination of an initial layer-by-layer growth and an

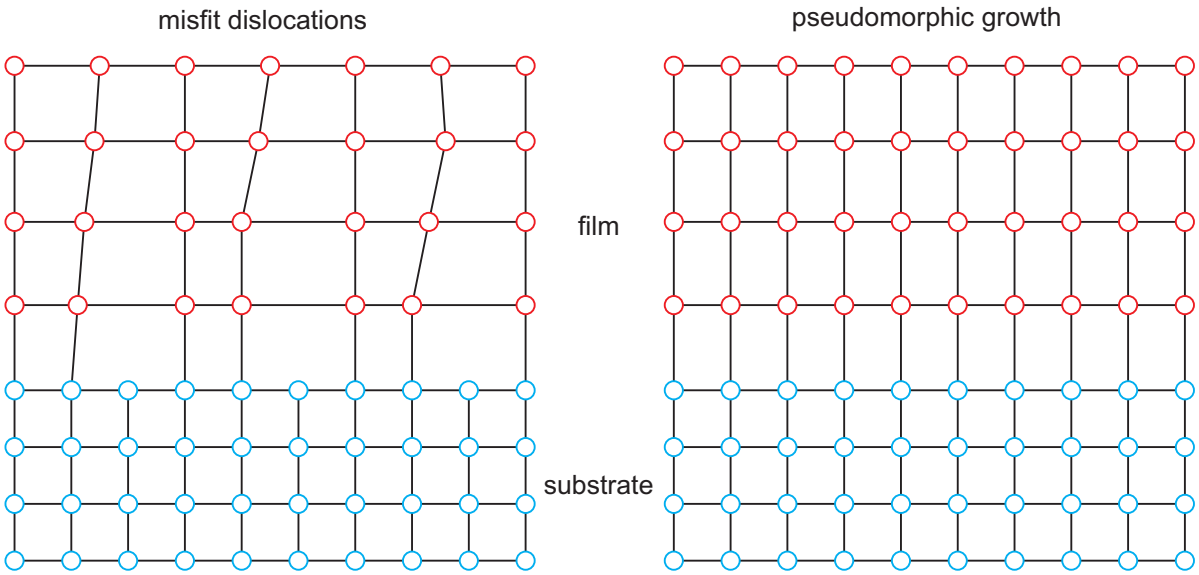

Fig. 2.3: Diagram of two different relaxation processes which can occur during film growth: (a) misfit dislocation and (b) pseudomorphic growth.

subsequent island growth. The critical thickness of the initial atomically flat layer at which the growth mode changes depends on different influences like growth temperature and lattice strain.

Lattice mismatch and relaxation

Usually the lattice constants of the crystalline materials to be grown are not equal to the lattice constant of the substrate. This leads to a lattice mismatch between the grown film and the substrate. Thus, strain effects are induced which are of special interest in thin film epitaxy. Many properties of the grown film like the magnetic anisotropy are influenced by these strain effects. Assuming similar crystal structures the lattice mismatch can be calculated with

$$\epsilon = \frac{a_{film} - a_{substrate}}{a_{substrate}} \tag{2.2}$$

using the lattice constants a_{film} and $a_{substrate}$ of the film and the substrate, respectively. The lattice mismatch is usually not the same in different crystallographic directions. In Fig. 2.3 two relaxation processes are presented which can occur to compensate the lattice mismatch. In the case of pseudomorphic growth the lattice of the film is stretched or compressed to in lateral direction to adopt the lateral lattice constant of the substrate (cf. Fig. 2.3(b)). Due to the energy minimization the vertical lattice constant of the film is expanded for in-plane compression and compressed for in-plane expansion. The relation between lateral and vertical strain can be determined for tetragonally distorted films [20] with

$$\frac{\Delta c}{c} = \frac{2\nu}{\nu - 1}\frac{\Delta a}{a} \quad . \tag{2.3}$$

Here, Δa and Δc are the deviation from the unstrained lateral and vertical lattice constant a and c, respectively. For each specific material the Poisson ratio ν can be calculated from the elastic constants given in literature [21–23]. The pseudomorphic growth is common in systems where the lattice mismatch is relative small.
The formation of misfit dislocation in the film is another possibility to compensate the lattice mismatch. This process is typical for systems with a large lattice mismatch (cf. Fig. 2.3(a)). In both cases the film relaxes with increasing film thickness towards the bulk properties.

Molecular beam epitaxy

Almost every film presented in this thesis was prepared using molecular beam epitaxy (MBE). It is one of the most common techniques to grow epitaxial thin films. An atomic or molecular beam is directed on the substrate surface. MBE normally has to be performed in a high vacuum (HV) or ultra high vacuum (UHV) chamber due to the insufficient free mean path of such atomic or particle beams under ambient conditions. In order to generate a molecular beam the source material is heated until it starts to evaporate or sublimate (depending on the used material). The heating is usually achieved by electron beam bombardment. Therefore, high voltage of $\approx 1000\,\mathrm{V}$ is applied to the source material which is, e.g., placed in a crucible. The electron source is an electrical filament which emits electrons. They are accelerated by the high voltage towards the source material. The source material or crucible is heated by absorbing the kinetic energy of the hitting electrons. Many metals like iron can be usually evaporated by applying the high voltage directly to a metal rod, while for silicon or gold a crucible is needed since the sublimation temperature is higher than the melting temperature at the given pressure.
Metal oxides films can be grown more simply by evaporating the pure metal in a low oxygen atmosphere instead of the corresponding metal oxide, since the required evaporation temperature is usually much lower. The oxidation state of the oxide phase can be adjusted by changing the oxygen partial pressure during the growth process. The evaporation of a source in an oxygen atmosphere is called reactive molecular beam epitaxy [12–14, 24–26] (RMBE). It is called plasma assisted MBE if oxygen plasma is used instead of oxygen gas [27]. It is also possible to use other reactive oxygen containing gases as oxygen source like NO_2 [28]. There are other common techniques to grow epitaxial films which are pulsed laser deposition [29] (PLD) and sputter deposition [30, 31]. During the PLD the source material is evaporated by an intense pulsed laser beam, while during the sputter deposition the atoms of the source material are ejected by ion bombardment (sputtering).

2.2 X-ray scattering

In order to determine the structure of the prepared samples X-ray scattering techniques are used which are important tools for the material science. The scattered intensity of an X-ray beam which is hitting a sample can be detected as function of incidence angle and scattered angle, polarization, and wavelength.
The main part of the X-rays are scattered at electrons instead of atom nuclei since the cross section of electrons is orders of magnitude bigger than the cross section of the atomic nuclei. Thus, the contribution of the X-rays scattered at nuclei is usually neglected. The Thomson formula provides the amplitude of an X-ray wave scattered at an electron at the position $\boldsymbol{r_e}$

$$A(\boldsymbol{q}) = A_0 \frac{e^2}{m_e\, c^2\, R_0}\, e^{\,i\boldsymbol{q}\cdot\boldsymbol{r_e}} \quad . \tag{2.4}$$

Here, the Amplitude of the incoming X-ray wave is A_0. m_e and e are mass and charge of an electron, c is the speed of light and R_0 is the distance between the electron and the observer. The amplitude $A(\boldsymbol{q})$ is depending on the scattering vector $\boldsymbol{q} \equiv \boldsymbol{k_f} - \boldsymbol{k_i}$ which is the difference of the wave vectors of the scattered ($\boldsymbol{k_f}$) and the incoming wave ($\boldsymbol{k_i}$). Since m_e, e, c, and R_0 are all constant they can be summarized to a constant prefactor $C \equiv \frac{e^2}{m_e\, c^2\, R_0}$ which simplifies Eq. (2.4) to

$$A(\boldsymbol{q}) = A_0\, C\, e^{\,i\boldsymbol{q}\cdot\boldsymbol{r_e}} \quad . \tag{2.5}$$

Sine the polarization of the incident beam is not considered in the Thomson formula, the measured intensity has to be revised by a correction factor which depends on the used scattering geometry.

2.3 X-ray diffraction

The theoretical description of X-ray diffraction (XRD) phenomenon was made by Laue [32] in 1912 and Bragg [33] in 1913. X-ray diffraction is the scattering of X-rays at long range ordered periodic systems which are typically crystals. Scattering at these systems cause constructive and destructive interference of the scattered waves which results in spots of very high intensity, the so called Bragg peaks or Bragg reflections.

2.3.1 The Bragg condition

According to Bragg the diffraction of X-rays at a crystal lattice can be interpreted as reflection of the incident beam at lattice planes. Fig. 2.4 shows the reflection of X-rays at a family of lattice planes which results in an interference pattern. The appearance of Bragg peaks can be described by Bragg's law

$$2\, d_{hkl}\, \sin\theta = n\, \lambda \quad . \tag{2.6}$$

Here, d_{hkl} is the distance between two lattice planes, θ is the angle between the lattice planes and both the incident wave and the outgoing wave. The vacuum wavelength of the incident beam is λ and n is the order of the Bragg reflection. The experimental limit for the angle θ

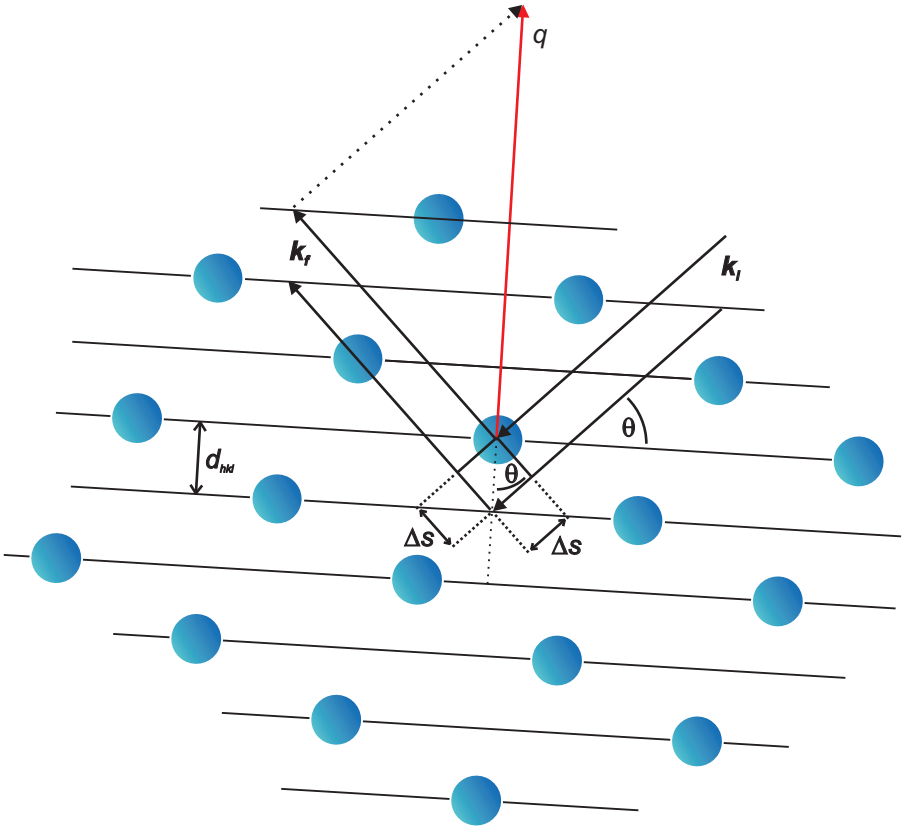

Fig. 2.4: Sketch to illustrate the Bragg condition. X-rays with the wave vector $\boldsymbol{k_i}$ are reflected at a lattice plane (solid line). The reflected X-rays $\boldsymbol{k_f}$ have a different phase due to the path difference Δs. The path difference has to be $2\Delta s = n\lambda$ to fulfill the Bragg condition for constructive interference. The scattering vector $\boldsymbol{q} = \boldsymbol{k_f} - \boldsymbol{k_i}$ is perpendicular to the lattice planes.

is 90°. Solving Eq. (2.6) for θ with $n = 1$ (first order) provides

$$\theta = \text{asin}\ \frac{\lambda}{2d_{hkl}} \quad . \tag{2.7}$$

Since $\frac{\lambda}{2d_{hkl}}$ has to be ≤ 1, this equation is only valid if $\lambda \leq 2d_{hkl}$. This condition gives a limit for the wavelength which is required to be able to study the first order Bragg peak. If the wavelength is bigger than the maximum path difference at normal incidence ($2a = 2d_{hkl}$) no diffraction can be observed.
The distance of the lattice planes in typical crystals is in the order of several Å. Thus, X-ray photons were used since their wavelength has the same magnitude. However, a too small wavelength causes very small Bragg angles which are technically difficult to observe. As a result, the resolution in reciprocal space is low.

The reciprocal space

The three Laue equations [32]

$$\boldsymbol{q} \cdot \boldsymbol{a} = 2\pi h \ , \tag{2.8}$$
$$\boldsymbol{q} \cdot \boldsymbol{b} = 2\pi k \ , \tag{2.9}$$
$$\boldsymbol{q} \cdot \boldsymbol{c} = 2\pi l \tag{2.10}$$

can also be used to identify the positions of the Bragg peaks. Whenever the Miller indices h, k, and l are integer numbers, there is constructive interference and Bragg peaks occur. The direct lattice parameters a, b, and c can not be obtained directly from X-ray diffraction experiments since it is not a direct microscopic technique which requires atomic resolution. Therefore, the reciprocal space is a useful concept to describe the measured diffraction data and to get information of the direct lattice. The reciprocal space vectors $\boldsymbol{a}^*$, $\boldsymbol{b}^*$, and $\boldsymbol{c}^*$ are related to the real space lattice vectors and are defined as

$$\boldsymbol{a}^* = 2\pi \frac{\boldsymbol{b} \times \boldsymbol{c}}{\boldsymbol{a} \cdot (\boldsymbol{b} \times \boldsymbol{c})} \ , \tag{2.11}$$
$$\boldsymbol{b}^* = 2\pi \frac{\boldsymbol{c} \times \boldsymbol{a}}{\boldsymbol{a} \cdot (\boldsymbol{b} \times \boldsymbol{c})} \ , \tag{2.12}$$
$$\boldsymbol{c}^* = 2\pi \frac{\boldsymbol{a} \times \boldsymbol{b}}{\boldsymbol{a} \cdot (\boldsymbol{b} \times \boldsymbol{c})} \tag{2.13}$$

where $\boldsymbol{a} \cdot (\boldsymbol{b} \times \boldsymbol{c})$ is the unit cell volume. In case that $\alpha = \beta = \gamma = 90°$ the length of the reciprocal lattice vectors are simplified to

$$a^* = \frac{2\pi}{a} \ , \tag{2.14}$$
$$b^* = \frac{2\pi}{b} \ , \tag{2.15}$$
$$c^* = \frac{2\pi}{c} \ . \tag{2.16}$$

It follows, that the Laue conditions for h, k, and l are automatically fulfilled if the scattering vector $\boldsymbol{q}$ is equal to or a multiple of one of the reciprocal lattice vectors $\boldsymbol{a}^*$, $\boldsymbol{b}^*$, and $\boldsymbol{c}^*$, respectively. In addition, when using these reciprocal basis vectors the Laue conditions are fulfilled at all positions in the reciprocal space defined by the coordinates (hkl) where h, k, and l are integers. This fact makes the description of diffraction phenomena by using the reciprocal space with corresponding reciprocal lattice vectors convenient.

Both Bragg condition and the Laue conditions provide only information about the periodicity of the crystal lattice. The contribution of the structure of the unit cell of the crystal is neglected. However, the inner structure of the unit cell can also influence the diffracted intensity of the Bragg peaks due to additional constructive or destructive interference conditions. Therefore, if a Bragg peak has zero intensity, it is called 'structure forbidden peak'.
The amplitude of the diffraction signal of a crystal is normally separated into its different

contributions. The structure factor $F(\boldsymbol{q})$ is the contribution of the unit cell and the lattice factor $G(\boldsymbol{q})$ is the contribution of the lattice symmetry. Thus, the amplitude $A(\boldsymbol{q})$ can be calculated with

$$A(\boldsymbol{q}) = F(\boldsymbol{q})\, G(\boldsymbol{q}) \quad . \tag{2.17}$$

Laue conditions and Bragg condition enable no quantitative analysis of the diffracted intensity. Since single crystals and other real objects are composed of many atoms and electrons, many electrons contribute to the total scattered intensity. The interaction of X-rays with matter is low, which allows to describe the X-ray scattering processes by the kinematical scattering theory. In this theory, multiple scattering, refraction and absorption are not considered and the scattered intensity of an object is given by the Fourier transformation of its electron density. In order to perform a quantitative analysis of the diffracted intensity of single crystal thin film systems grown on single crystal substrates, the following expressions are derived using the simplifications from the kinematic approximation. The theoretical descriptions of this derivation can be found in references [34–37].

2.3.2 Scattering at single atoms

If a wave is scattered at a single atom, the scattering amplitude is given by the summation of the scattering at all electrons of this atom. As mentioned in section 2.2, the scattering amplitude of each single electron is defined by the Thompson Eq. (2.4). However, the electrons are not localized at the center of an atom at the position $\boldsymbol{r_a}$. The electrons are at different positions $\boldsymbol{r}$ around the center of the atom and the distribution of the electrons is given by their density function ρ. Thus, phase differences between the scattered waves from each electron have to be considered in the summation of the scattering amplitudes. Although the distance between the electrons and observer R_0 is slightly different for each electron, this difference can be neglected since the distance between the electrons and the center of their atom $|\boldsymbol{r}|$ is orders of magnitude smaller than R_0. As a consequence, the same value of R_0 can be used for all electrons. With these assumptions the scattering amplitude of a wave scattered at an atom can be calculated with

$$A(\boldsymbol{q}) = A_0\, C \int d^3r\, \rho(\boldsymbol{r})\; e^{\,i\,\boldsymbol{q}\cdot\,(\boldsymbol{r_a}\,+\,\boldsymbol{r})} \tag{2.18}$$

$$= A_0\, C\, f(\boldsymbol{q})\; e^{\,i\,\boldsymbol{q}\,\cdot\,\boldsymbol{r_a}} \quad . \tag{2.19}$$

Here, $f(\boldsymbol{q})$ is the atomic form factor, which is defined as

$$f(\boldsymbol{q}) = \int d^3r\, \rho(\boldsymbol{r})\; e^{\,i\,\boldsymbol{q}\,\cdot\,\boldsymbol{r}} \quad , \tag{2.20}$$

which is the Fourier transform of the electron density. The atomic form factors of different atoms and ions can be found in tables in literature [38]. They have been calculated by density functional theory or quantum mechanical methods like Hartree-Fock. Spherical electron

distributions are used for the calculations of the atomic form factors used in this work. As a result, the form factor is independent of the spatial direction and changes only with the absolute value of the scattering vector $\boldsymbol{q}$. The atomic form factor can be analytically approximated by a sum of four Gaussian functions

$$f(\boldsymbol{q}) = \sum_{j=1}^{4} a_j \; e^{-b_j \left(\frac{\boldsymbol{q}}{4\pi}\right)^2} + c \quad . \tag{2.21}$$

The values for the coefficients a_j, b_j, and c are obtainable for almost all atoms and ions in literature [38].

2.3.3 Scattering at a unit cell

The scattering amplitude of X-rays scattered at a unit cell can be derived by a summation of the scattering amplitudes of each atom inside the unit cell. Similar to the derivation of the scattering amplitude of a single atom, the phase differences of the scattering waves have to be considered since each atom is at a different position $\boldsymbol{r_j}$. The position of the unit cell is denoted with $\boldsymbol{r_n}$. The scattering amplitude of a unit cell can be calculated with

$$A\,(\boldsymbol{q}) = A_0\, C \sum_j f_j(q)\, e^{i\boldsymbol{q}\cdot\,(\boldsymbol{r_n}+\boldsymbol{r_j})} \tag{2.22}$$

$$= A_0\, C\, F(\boldsymbol{q})\; e^{i\boldsymbol{q}\cdot\boldsymbol{r_n}} \quad . \tag{2.23}$$

The structure factor F of a unit cell can be determined similar to the atomic form factor f of an atom with

$$F\,(\boldsymbol{q}) = \sum_j f_j(q)\, e^{i\boldsymbol{q}\cdot\boldsymbol{r_j}} \quad . \tag{2.24}$$

However, in contrast to the atomic form factor which is only a function of the magnitude of the scattering vector $\boldsymbol{q}$, the structure factor is also a function of the direction of the scattering vector $\boldsymbol{q}$.

The Debye-Waller factor

Usually the atoms in a unit cell differ from their ideal positions due to thermal vibrations. As a consequence, the scattered intensity is damped by a factor due to the disturbed phase relation of the scattered waves. This factor is a Gaussian distribution, which models the deviation of the atoms from their ideal position. D is the Debye-Waller factor which is proportional to the temperature of the crystal and is related to the square of the displacement of the atoms.

Hence, the modified structure factor is defined by

$$F(\boldsymbol{q}, D) = e^{-D|q|^2} \sum_j f_j(q)\, e^{i\boldsymbol{q}\cdot\boldsymbol{r_j}} \tag{2.25}$$

Thus, the damping of the structure factor increases with increasing scattering vector $\boldsymbol{q}$ and with increasing atomic dislocation due to the Debye-Waller factor. A detailed derivation of the Debye-Waller factor can be found in literature [39–41].

2.3.4 Diffraction at single crystals

Single crystals are formed by an infinite number of periodically arranged unit cells. Thus, diffraction phenomena can be observed whose intensity can be calculated by summation of the diffraction amplitude of all unit cells

$$A(\boldsymbol{q}) = A_0\, C \sum_n F_n(\boldsymbol{q}, D)\; e^{i\boldsymbol{q}\cdot\boldsymbol{r_n}} \quad . \tag{2.26}$$

As is the case for the other derivations, the phase differences between the scattered waves have to be considered. For a three dimensional perfect crystal F_n is identical for all unit cells. In order to calculate the diffraction amplitude for a finite three dimensional perfect crystal with a finite number of unit cells Eq. (2.26) can be rewritten to

$$A(\boldsymbol{q}) = A_0\, C\, F(\boldsymbol{q}, D) \sum_{n_a=0}^{N_a-1} \sum_{n_b=0}^{N_b-1} \sum_{n_c=0}^{N_c-1} e^{i\boldsymbol{q}\cdot\,(n_a\boldsymbol{a} + n_b\boldsymbol{b} + n_c\boldsymbol{c})} \tag{2.27}$$

$$= A_0\, C\, F(\boldsymbol{q}, D) \sum_{n_a=0}^{N_a-1} e^{in_a\,\boldsymbol{q}\cdot\boldsymbol{a}} \sum_{n_b=0}^{N_b-1} e^{in_b\,\boldsymbol{q}\cdot\boldsymbol{b}} \sum_{n_c=0}^{N_c-1} e^{in_c\,\boldsymbol{q}\cdot\boldsymbol{c}} \quad . \tag{2.28}$$

Here, $\boldsymbol{a}$, $\boldsymbol{b}$, and $\boldsymbol{c}$ are the lattice vectors of the crystal and N_a, N_b, and N_c are the numbers of unit cells in the three corresponding dimensions.

2.3.5 Crystal truncation rods

The extension of a crystal is important for the observed diffraction pattern. For a bulk crystal with infinite size in all three directions ($N_{a,b,c} \to \infty$) Eq. (2.28) becomes a series of δ functions and the intensity peaks are at single points known as Bragg peaks (cf. Fig. 2.5 (a), see also the Laue conditions in Eq. (2.10)). In the case of an infinite 2D crystal $N_c = 1$, the diffracted intensity is only sharp in lateral direction but diffuse in vertical direction. The diffuse intensity form diffraction rods [34,35], which are perpendicular to the surface (cf. Fig. 2.5 (b)). A semi-infinite 3D crystal with $N_{a,b} \to \infty$ and $N_c \neq \infty$ features smeared out Bragg peaks resulting in crystal truncation rods (CTRs, cf. Fig. 2.5 (c)). Thin films produce oscillations between the Bragg peaks based on the number of layers N_c (cf. Fig. 2.5 (d)).

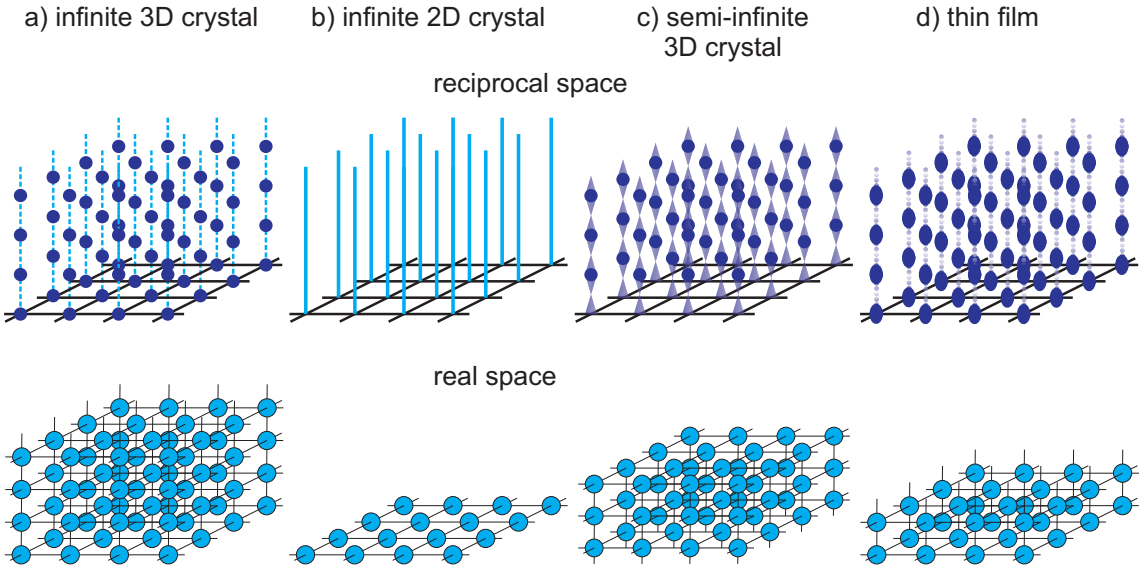

Fig. 2.5: Sketch of the reciprocal space and the corresponding real space of (a) a 3D crystal, (b) a monolayer (infinite 2D crystal), (c) a semi-infinite 3D crystal, and (d) a thin film. Three dimensional crystals produce sharp Bragg peaks. The 2D layer shows no distinct Bragg peaks but diffraction rods. A semi-infinite 3D crystal exhibits diffraction spots which are smeared out in vertical direction. Thin films feature diffraction spots and oscillations in vertical direction. The frequency of the oscillations depends on the thickness of the thin film. Taken and modified from Ref. [35]

Diffraction at semi-infinite crystals

Mathematically the diffracted amplitude of a semi-infinite crystal like an MgO substrate (A_{sub}) can be described by replacing the sum over n_c for the vertical direction in Eq. (2.28) with

$$\sum_{n_c=-\infty}^{N_c(n_a,n_b)} e^{n_c \epsilon} \, e^{i\, n_c \boldsymbol{q} \cdot \boldsymbol{c}} \quad . \tag{2.29}$$

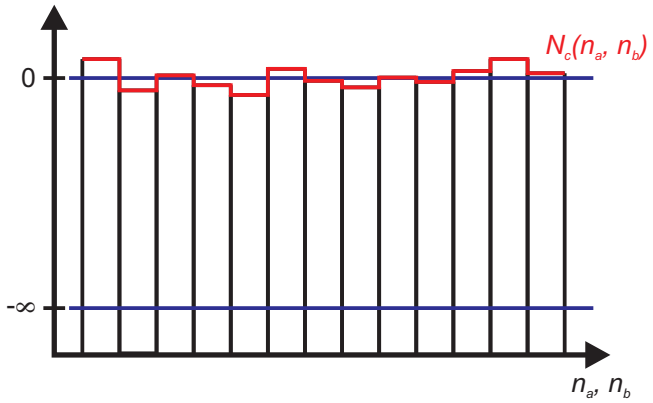

Fig. 2.6: Schematic drawing of the height profile of a semi-infinite crystal surface. The function $N_c(n_a, n_b)$ describes the step height at each individual point (n_a, n_b). The average step height is at zero level.

This leads to

$$A_{sub}\,(\boldsymbol{q}) = A_0\, C\, F\,(\boldsymbol{q}, D) \sum_{n_a=0}^{N_a-1} e^{\,i\, n_a\, \boldsymbol{q}\cdot\boldsymbol{a}} \sum_{n_b=0}^{N_b-1} e^{\,i\, n_b\, \boldsymbol{q}\cdot\boldsymbol{b}} \sum_{n_c=-\infty}^{N_c(n_a,n_b)} e^{\,i\, n_c\, \boldsymbol{q}\cdot\boldsymbol{c} + n_c\,\epsilon} \quad . \tag{2.30}$$

Here, in order to take into account the attenuation of the X-rays due to absorption within deeper crystal layers the factor $e^{\,n_c\epsilon}$ is introduced. The function $N_c(n_a, n_b)$ describes the height variation of the semi-infinite crystal in lateral direction to consider the surface roughness (cf. Fig. 2.6). The Laue conditions in lateral direction ($\boldsymbol{q}\cdot\boldsymbol{a} = 2\pi\, h$ and $\boldsymbol{q}\cdot\boldsymbol{b} = 2\pi\, k$) are fulfilled on a crystal truncation rod. Thus, Eq. (2.30) simplifies to

$$A_{sub}\,(\boldsymbol{q}) = A_0\, C\, F\,(\boldsymbol{q}, D) \sum_{n_a=0}^{N_a-1} 1 \sum_{n_b=0}^{N_b-1} 1 \sum_{n_c=-\infty}^{N_c(n_a,n_b)} e^{\,i\, n_c\, \boldsymbol{q}\cdot\boldsymbol{c} + n_c\epsilon} \tag{2.31}$$

$$= A_0\, C\, F\,(\boldsymbol{q}, D) \sum_{n_a=0}^{N_a-1} \sum_{n_b=0}^{N_b-1} \frac{e^{\,(i\,\boldsymbol{q}\cdot\boldsymbol{c} + \epsilon)\, N_c(n_a, n_b)}}{1 - e^{\,-(i\,\boldsymbol{q}\cdot\boldsymbol{c} + \epsilon)}} \quad . \tag{2.32}$$

Here, the sums over n_a and n_b corresponds to an averaging over the height function $N_c(n_a, n_b)$ with an average value at zero level. Instead we can also write

$$A_{sub}\,(\boldsymbol{q}) = A_0\, C\, F\,(\boldsymbol{q}, D)\, N_a N_b \frac{\left\langle e^{\,(i\,\boldsymbol{q}\cdot\boldsymbol{c} + \epsilon)\, N_c(n_a, n_b)} \right\rangle}{1 - e^{\,-(i\,\boldsymbol{q}\cdot\boldsymbol{c} + \epsilon)}} \quad . \tag{2.33}$$

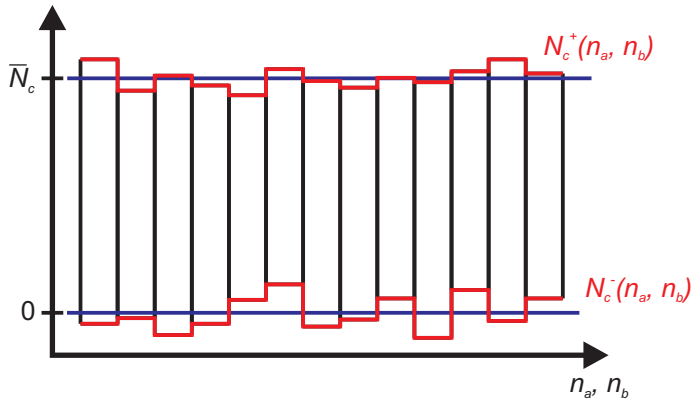

Fig. 2.7: Sketch of a thin film with a roughness at the bottom and at the top modeled with the height functions $N_c^-(n_a, n_b)$ and $N_c^+(n_a, n_b)$, respectively. The average film thickness is $\overline{N_c}$.

The height function $N_c(n_a, n_b)$ can be approximated by a Gaussian distribution [42] and we obtain

$$A_{sub}(\boldsymbol{q}) = A_0\, C\, F(\boldsymbol{q}, D)\, N_a N_b\, \frac{e^{-\sigma^2 (1 - \cos \boldsymbol{q}\cdot\boldsymbol{c})}}{1 - e^{-(i\,\boldsymbol{q}\cdot\boldsymbol{c} + \epsilon)}} \quad . \tag{2.34}$$

Here, σ is the root mean square (rms) roughness of the surface of the semi-infinite substrate.

Diffraction at thin films

With a few modifications the diffracted amplitude of a thin film (A_{film}) consisting of a few layers N_c can be calculated quite similar to the amplitude of the semi-infinite crystal. First, the attenuation factor $e^{n_c \epsilon}$ can be neglected. Second, besides the roughness at the top of the film the roughness at the bottom of the film has to be considered as well. Thus, two height functions $N_c^+(n_a, n_b)$ for the top and $N_c^-(n_a, n_b)$ for the bottom are used (cf. Fig. 2.7). Since there is no consistent number of unit cells in vertical direction the average film thickness $\overline{N_c}$ has to be used. With these modifications the diffracted amplitude is defined as

$$A_{film}(\boldsymbol{q}) = A_0\, C\, F(\boldsymbol{q}, D) \sum_{n_a=0}^{N_a-1} 1 \sum_{n_b=0}^{N_b-1} 1 \sum_{n_c=N_c^-(n_a,n_b)}^{N_c^+(n_a,n_b)} e^{i\, n_c\, \boldsymbol{q}\cdot\boldsymbol{c}} \tag{2.35}$$

$$= A_0\, C\, F(\boldsymbol{q}, D) \sum_{n_a=0}^{N_a-1} \sum_{n_b=0}^{N_b-1} \frac{e^{i\,\boldsymbol{q}\cdot\boldsymbol{c}\, N_c^-(n_a,n_b)} - e^{i\,\boldsymbol{q}\cdot\boldsymbol{c}\, N_c^+(n_a,n_b) + 1}}{1 - e^{i\,\boldsymbol{q}\cdot\boldsymbol{c}}} \quad . \tag{2.36}$$

Analogously to Eq. (2.32) the sums can be expressed by an averaging

$$A_{film}(\boldsymbol{q}) = A_0\, C\, F(\boldsymbol{q}, D)\, N_a N_b \frac{\left\langle e^{i\boldsymbol{q}\cdot\boldsymbol{c}\, u_c^-} \right\rangle - e^{i\,\boldsymbol{q}\cdot\boldsymbol{c}\,\overline{N_c}} \left\langle e^{i\boldsymbol{q}\cdot\boldsymbol{c}\, u_c^+} \right\rangle}{1 - e^{i\,\boldsymbol{q}\cdot\boldsymbol{c}}} \quad . \tag{2.37}$$

Here, u_c^+ is the top and u_c^- is the bottom deviation from the average film thickness $\overline{N_c}$. For u_c^+ and u_c^- Gaussian distributions can be assumed which leads to

$$A_{film}(\boldsymbol{q}) = A_0\, C\, F(\boldsymbol{q}, D)\, N_a N_b \frac{e^{-\sigma_-^2 (1-\cos \boldsymbol{q}\cdot\boldsymbol{c})} - e^{i\,\boldsymbol{q}\cdot\boldsymbol{c}\overline{N_c}}\, e^{-\sigma_+^2 (1-\cos \boldsymbol{q}\cdot\boldsymbol{c})}}{1 - e^{i\,\boldsymbol{q}\cdot\boldsymbol{c}}} \quad . \tag{2.38}$$

Here, σ_+ and σ_- are the rms roughnesses at the top and at the bottom of the film, respectively. If top and bottom roughness of the film are zero Eq. (2.38) reduces to an N-slit function

$$S_N(x) = \sum_{n=0}^{N-1} e^{inx} = \frac{1 - e^{ixN}}{1 - e^{ix}} \quad . \tag{2.39}$$

with $x = \boldsymbol{q}\cdot\boldsymbol{c}$ and $N = \overline{N_c}$. Up to a maximum value of N, the N-slit function exhibits maxima at $x = 2\pi m$ for $m \in \mathbb{Z}$. The N-Slit function shows also $N - 2$ smaller side maxima between the main maxima which are called fringes or Laue oscillations. Laue fringes give information about the number of coherently scattering lattice planes. The number of fringes increases with the number of slits N, while the width of the main maxima and the fringes is decreasing. If the number of slits N becomes infinite the fringes vanish and the main maxima become δ-peaks since the N-slit function becomes periodically iterated δ functions. By way of illustration, the N-slit function is plotted for $N = 10$ in Fig. 2.8.

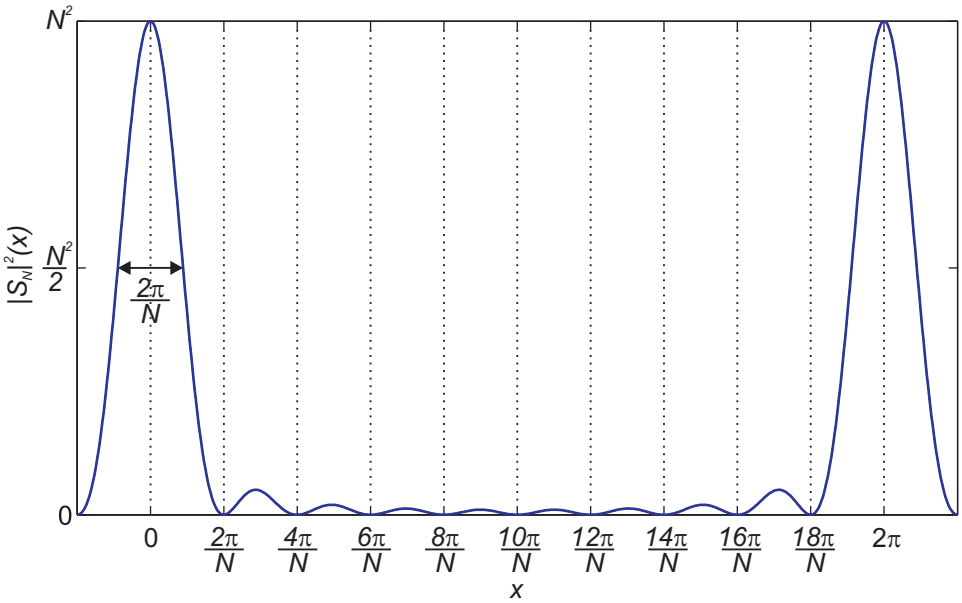

Fig. 2.8: N-slit function for $N = 10$. The main maxima are at multiples of 2π.

Calculating the diffracted intensity from a thin film layer system

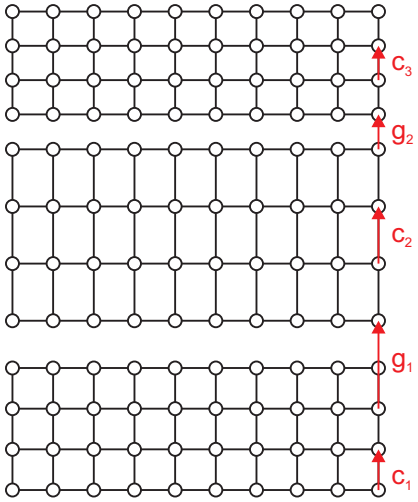

Fig. 2.9: Model of a layer system which consists of a substrate with two films.

The diffracted intensity A_{system} of a layer system shown in Fig. 2.9 which consists of a substrate and one or more films on top of it can be calculated by the sum over their diffracted intensities considering the phase differences

$$A_{system}(\boldsymbol{q}) = A_{sub}(\boldsymbol{q}) + \sum_i \Theta_i \, e^{i\,\boldsymbol{q}\cdot\boldsymbol{p_i}} \, A_{film,i}(\boldsymbol{q}) \quad . \tag{2.40}$$

Here, impurities and dislocations in the films are described by the occupation factor Θ_i. The phase differences between the substrate and the layers are taken into account with the factor $e^{i\,\boldsymbol{q}\cdot\boldsymbol{p_i}}$, where the origin of the i-th layer is defined by $\boldsymbol{p_i}$ (phase vector)

$$\boldsymbol{p_i} = \sum_{j=0}^{i-1} \boldsymbol{g_j} + \overline{N_{cj}}\boldsymbol{c_j} \quad . \tag{2.41}$$

Here, the interface vector $\boldsymbol{g_j}$ determines the distance and the lateral shift between layer j and $j+1$. The phase shift caused by the film thickness of layer j is given by the term $\overline{N_{cj}}\boldsymbol{c_j}$.

2.4 X-ray reflectivity

X-ray reflectivity or X-ray reflectometry (XRR) enables to determine film thickness, interface roughness and refractive index of every single film of a film system. With this method the intensity of the reflected beam is measured as a function of the incidence angle α_i. The incidence angle is usually kept below 6° (for hard X-rays) for such measurements and is given as angle between the incident beam and the surface. This definition is in contrast to conventional optics, where the incidence angle is defined with respect to the surface normal. The theory of X-ray reflectivity is described in more detail in the literature [43, 44].
The complex refractive index n is the principle value to describe the reflectivity of a material and for X-rays it is defined as

$$n = 1 - \delta + i\beta \quad . \tag{2.42}$$

The value δ is proportional to the electron density while β is proportional to the absorption of the analyzed material. Therefore, both δ and β are material specific constants which also depend on the wavelength of the incident light. Usually δ is of the order of 10^{-6} while β is mostly about 100 times smaller than δ. Thus, the refractive index of X-rays is smaller than 1.
With the refraction index n and Snell's law we can estimate the critical angle of total reflection

$$\alpha_c \approx \sqrt{2\,\delta} \tag{2.43}$$

Below this critical angle the incident X-rays are totally reflected. As a result, X-rays can only penetrate the material if the incidence angle is higher than α_c. The law of reflection which can be derived from the Fresnel equations provides $\alpha_i = \alpha_f$, where α_f is the angle of reflection. Thus, the reciprocal scattering vector $\boldsymbol{q}$ is perpendicular to the film surface (cf. Fig. 2.10) and can be calculated with $\boldsymbol{q} = \boldsymbol{k_f} - \boldsymbol{k_i}$. The magnitude of the wave vector is $|\boldsymbol{k}| = \frac{2\pi}{\lambda}$, where λ is the vacuum wavelength. For elastic scattering $|\boldsymbol{k_i}| = |\boldsymbol{k_i}|$ is valid.
The Fresnel coefficient

$$r_{j,j+1} = \frac{q_j - q_{j+1}}{q_j + q_{j+1}} \tag{2.44}$$

provides the reflectivity of an interface of two layers (j and $j+1$) of different composition with different refraction indexes, where $q_j = |k|\sqrt{n_j^2 - \cos^2\alpha_i}$ is the vertical component of the wave vector in layer j. Since the refraction index is $n \approx 1$, q_j can be simplified to

$$q_j = \frac{4\pi}{\lambda}\sin(\alpha_i) \quad . \tag{2.45}$$

With Eq. (2.45) every scattering angle α can be converted into a corresponding scattering vector q.

In order to calculate the reflected intensity as shown in Fig. 2.11 the recursive Parratt algorithm [45] is used, which takes into account the reflectivity and transmission of each interface. Different roughness models have been proposed when using the Parrat algorithm to consider the interface roughness which also affects the reflected intensity. For solid thin films the Névot-Croce formalism [46] is the most common model and it is also used for the

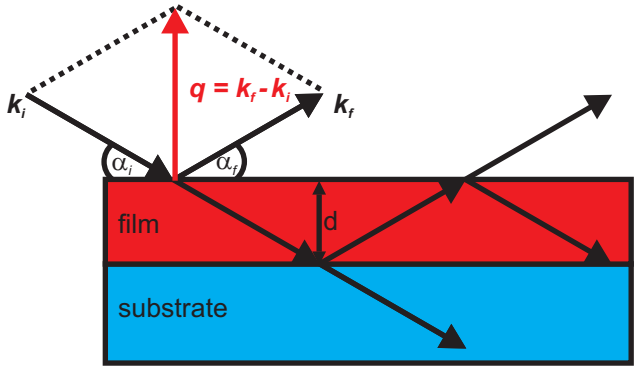

Fig. 2.10: Reflectivity of a thin film on a substrate. Transmission and reflection of the incident beam k_i occurs at each interface of the film-substrate system. The reflection k_f at the film-substrate interface is also contributing to the total reflected intensity. .

calculations in this work. In this model, the non-homogeneous thickness has a Gaussian distribution with a mean thickness d and a standard deviation σ. With this assumption, the reflectivity of the interface is reduced by an exponential $e^{-\frac{d}{2\sigma^2}}$ factor. However, this model only makes sense if the roughness is considerably smaller than the film thickness. If the interface roughness is as big as the film thickness other models have to be applied like arbitrary density model [44]. In this model the electron density profile is represented by a stack of very thin flat individual layers. Calculated reflectivity curves of 20 nm magnetite

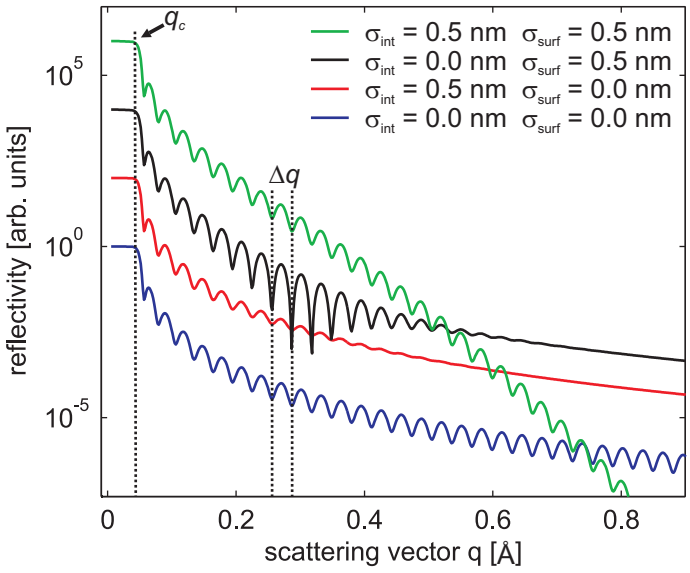

Fig. 2.11: Reflectivity curves for 20 nm magnetite films on magnesium oxide substrates with different surface (σ_{surf}) and interface (σ_{int}) roughness at 10.5 keV. There is total external reflection up to the critical scattering vector q_c. Above this critical angle the intensity is decreasing and intensity oscillations caused by the magnetite film occur. These oscillations originate from an interference between the beams reflected at the film/vacuum and the substrate/film interface. The strength of the reflectivity and the intensity oscillations depend on the Fe_3O_4/MgO interface and Fe_3O_4 surface roughness .

films on MgO(001) with different surface and interface roughness are shown in Fig. 2.11. Above the critical scattering vector q_c the reflected intensity is decreasing with increasing scattering vector by a factor of $1/q^4$. The 20 nm magnetite film causes intensity oscillations which originate from the interference between the X-rays reflected at the film/vacuum and at the substrate/film interface. The film thickness d of a single film on a substrate can be

estimated by using

$$d = \frac{2 \cdot \pi}{\Delta q} \approx \frac{\lambda}{2\Delta\alpha_i} \tag{2.46}$$

where Δq or $\Delta\alpha_i$ are the distances between two minima (or maxima). The interface σ_{int} and surface σ_{surf} roughness affect the strength of the intensity oscillations and the reflectivity. While a high interface roughness attenuates the amplitude of the oscillation, the surface roughness also slightly weakens the reflectivity and causes a beat. A combination of both a high interface roughness and a high surface roughness leads to a drastic attenuation of the reflectivity. However, the intensity oscillations are hardly attenuated.

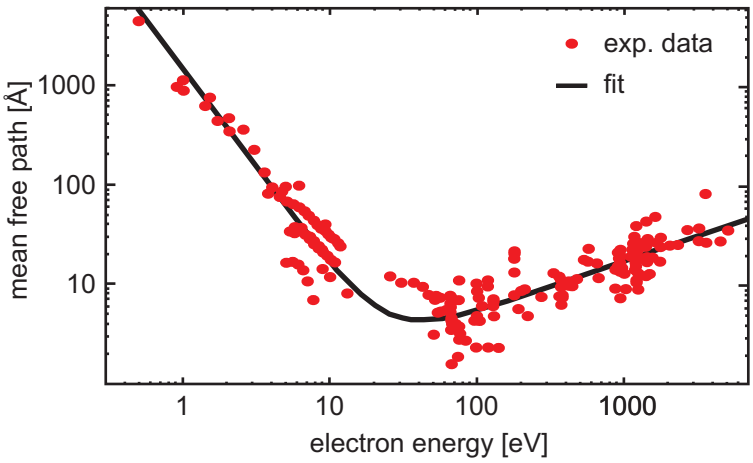

Fig. 2.12: Inelastic mean free path of electrons plotted against kinetic energy.

2.5 Low energy electron diffraction

Low energy electron diffraction (LEED) is one of the most important techniques for the characterization of structural properties of surfaces. Instead of X-ray photons low kinetic energy electrons ($E_{kin} < 1000\,\text{eV}$) are used which have a similar wavelength. The wavelength of particles λ is called De Broglie wavelength and for electrons it is given by

$$\lambda_{\text{De Broglie}} = \frac{h}{\sqrt{2m_e E_{kin}}} \tag{2.47}$$

using the mass of an electron m_e, the Planck constant h and the kinetic Energy E_{kin}. Due to the higher interaction of electrons with matter the penetration depth of electrons is small compared to X-ray photons (cf. Fig. 2.12). Thus, the surface sensitivity is considerably higher but only the surface near region can be analyzed ($\approx 1\,\text{nm}$). As a result the Bragg peaks observed in reciprocal space are broadened in vertical direction and become Bragg rods (cf. Fig. 2.5). This observation is similar to the surface scattering in the X-ray case. Thus, almost no bulk information contributes when using electron diffraction due to the small penetration depth of the electrons and the observed diffraction rods originates only from the surface. Small bulk contributions as well as atomic steps on the surface can be seen as modulations of the intensity along the vertical rods. The Ewald construction in Fig. 2.13 helps to determine whether diffraction can be observed or not. The surface of the Ewald sphere is given by all possible exiting wave vectors $\boldsymbol{k_f}$ and its radius is the length the wave vector $|\boldsymbol{k_f}| = |\boldsymbol{k_i}|$ (elastic scattering). Diffraction occurs every time the Ewald sphere is intersecting a Bragg rod.

The fluorescent screen covers a large segment of the hemisphere above the sample, therefore, all reflexes originating from wave vectors pointing in the direction of the detector are visible. The fluorescent spots on the screen display the symmetry of the reciprocal space in lateral direction. In order to attain preferably sharp peaks the electrons beam can be focused on the fluorescent screen.

If the incidence angle of the electron beam is fixed the wavelength (kinetic energy) of the electrons is the only possibility to change the scattering condition. The modification of the

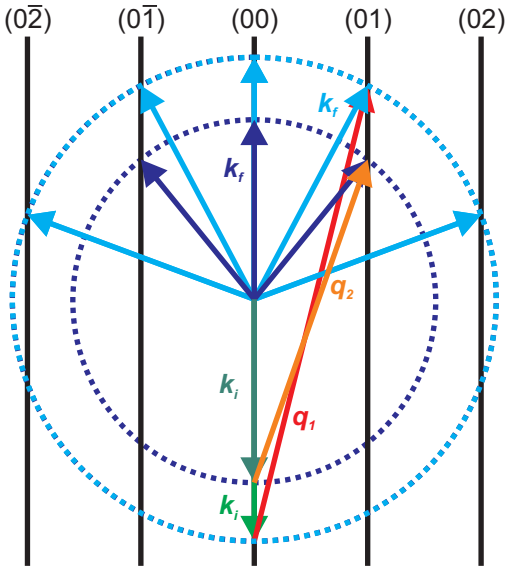

Fig. 2.13: Ewald construction for a LEED setup with normal incidence. The Ewald sphere (blue dotted line) is defined by all possible positions for the wave vector $\boldsymbol{k_f}$, thus, it has the radius $—\boldsymbol{k_f}—$. Diffraction spots can be observed with LEED whenever the Ewald sphere is intersecting a Bragg rod (solid lines).

electron wavelength changes the radius of the Ewald sphere, thus, the intersections of the Ewald sphere with the Bragg rods also vary (cf. Fig. 2.13).

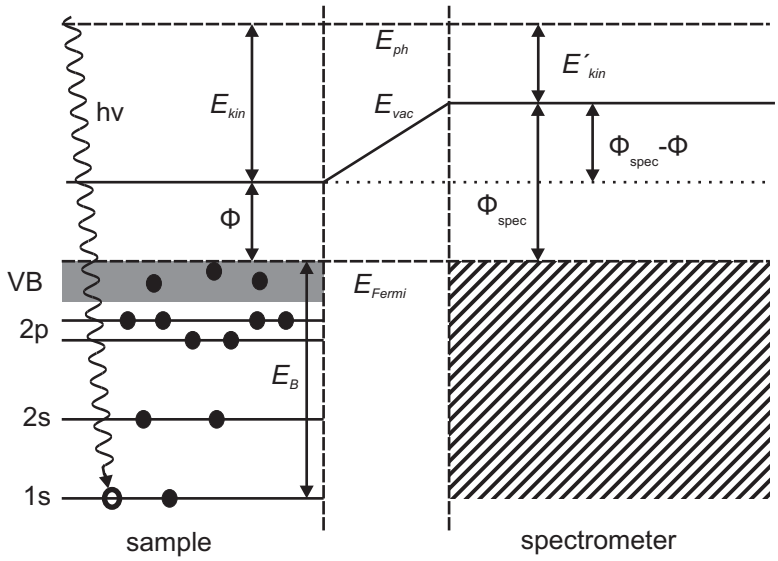

Fig. 2.14: Schemetical drawing of an energy level diagram. An electron is excited by incoming photons with the energy $E_{ph} = h\nu$. With the absorbed energy the photoelectron can overcome the binding Energy E_B and the work function ϕ in order to leave the sample with the kinetic energy E_{kin}. Above the vacuum level E_{vac}, the photoelectron with a kinetic energy of E'_{kin} reach the analyzer with the work function ϕ_{spec}.

2.6 X-ray photoelectron spectroscopy

X-ray photoelectron spectroscopy (XPS) is one of the most important surface-sensitive spectroscopic techniques for the non-destructive analysis of the stoichiometry, chemical state and electronic state of the elements that exist within a material. XPS is based on the photoelectric effect, which is described in the following. An electron in a state with the binding energy E_B relative to the Fermi level E_F absorbs the energy of a photon of the incident radiation (cf. Fig. 2.14). With this energy, the electron can overcome its binding energy E_B and the work function $\phi = E_{vac} - E_F$ to leave the solid. The emitted electron has a kinetic energy of

$$E_{kin} = h\nu - E_B - \phi \ . \tag{2.48}$$

Thus, knowing the work function ϕ and the excitation energy $h\nu$, E_{kin} can be used to determine E_B. The higher the binding Energy E_B of the electron, the higher the photon energy $h\nu$ has to be to generate a photoelectron. In order to excite electrons from the core level of an atom, X-ray photons are necessary while electrons from the valence band can be also excited by ultra violet light which is advantageous due to the larger cross section. The binding energy E_B of a certain electron state depends on the Coulomb potential of the nucleus. Therefore, the E_B of a photoelectron is like a fingerprint of the corresponding atom, which allows an identification of the atoms inside the analyzed material. The binding energy of an electron is also influenced by the chemical environment of the corresponding atom since the chemical environment exerts additional forces on the electron. As a consequence, the measured binding energies of the photoelectrons can differ from the characteristic values of electrons of a free atom by several eV.

Besides the main peaks there are also satellite peaks which have different origins. Shake-up and shake-off satellites are caused by the excitation of an electron from the valence band by photoelectrons. While shake-up satellites occur when a valence band electron is excited to a higher energy level, shake-off satellites arise when the excited valence band electron leaves the atom. In both cases the photoelectrons loses kinetic energy, thus, the shake-up and the shake-off satellites are shifted by a few eV to higher binding energies compared to the main line.
The photoemission spectra of transition metal (TM) oxides exhibit so called charge transfer satellites. These satellites emerge for example if an electron from the 2p orbital of the oxygen can transfer to the 3d orbital of the TM. In this case the binding energy of this electron is increased by

$$\Delta E = E(3d^{n+1}L^{-1}) - E(3d^{n}L) \ . \tag{2.49}$$

Here, L denotes the corresponding oxygen ligand, which transfers an electron to the $3d^n$ orbital of TM. Thus, the satellites due to charge transfer are always shifted to higher binding energies.
Another reason for the occurrence of satellites is the usage of non-monochromatized X-ray radiation. In this case, there are additional excitation energies, since the characteristic X-ray spectrum of aluminum features besides the dominant K$\alpha_{1,2}$ peaks also the weaker K$\alpha_{3,4}$ peaks at $\approx 10\,\text{eV}$ higher photon energy. Thus, this additional excitation energy causing an additional satellite peak at $\approx 10\,\text{eV}$ lower binding energy next to every peak in the XP spectra which is generated by the K$\alpha_{3,4}$ radiation. However, this satellite peak has only 10 % of the intensity of the main peak caused by the K$\alpha_{1,2}$ radiation.
Another effect during an XPS experiment is the positive static charging of insulating samples like magnesium oxide, which increases the binding energy of the photoelectrons due to the additional attractive electric field. Thus, the measured spectra have to calibrated by shifting the whole spectra by the amount of static charge which can be figured out by comparing the binding energy of known peaks with the literature. So it may happen that a charged spectrum and an uncharged spectrum of a sample are measured simultaneously if one part of the sample is more conductive than another. Since the charged spectrum is usually more intensive than the uncharged version, the uncharged version occurs also as satellites in the charged version.
XPS measurements are performed under ultra high vacuum conditions due to the small mean free path of electrons at ambient conditions. The penetration depth of X-ray photons into a solid sample is in a range of $1-10\,\mu m$, however, due to the small mean free path λ of electrons in a solid the information depth of XPS is limited to some Ångströms up to a few nanometer. Thus, XPS like LEED is a very surface-sensitive technique. In order to even increase the surface-sensitivity, it is possible to illuminate the sample at grazing incidence below the angle of total external reflection and/or to collect photoelectrons at grazing exit. In this case the angle dependent information depth d is given by

$$d = 3 \cdot \lambda \cos(\theta) \tag{2.50}$$

where θ is the collecting angle and λ is the mean free path.
In order to achieve a higher bulk sensitivity HAXPES (hard X-ray photoemission spectroscopy) is used to increase the kinetic energy of the photoelectrons by the higher photon

energy. It is also necessary to use HAXPES to analyze the core level of heavier atoms which have a binding energy above the excitation energy of Al Kα.

2.7 Matter in magnetic fields

In order to describe matter in magnetic fields the magnetic field strength $\boldsymbol{H}$ and the resulting magnetic magnetic flux density $\boldsymbol{B}$ are used. Both are related to each other by the magnetic field constant (vacuum permeability) μ_0 and the material related permeability tensor $\hat{\mu}_r$ according to the following equation

$$\boldsymbol{B} = \mu_0 \hat{\mu}_r \boldsymbol{H} \quad . \tag{2.51}$$

The magnetization $\boldsymbol{M}$ in the sample is influenced by the magnetic field $\boldsymbol{H}$. The type and strength of the magnetization $\boldsymbol{M}$ depends on the magnetic susceptibility $\hat{\chi}$ of the material. This leads to

$$\boldsymbol{M} = \hat{\chi} \boldsymbol{H} \quad . \tag{2.52}$$

The magnetic flux density is given by

$$\boldsymbol{B} = \mu_0 (\boldsymbol{H} + \boldsymbol{M}) \tag{2.53}$$

as the sum of the magnetic field strength $\boldsymbol{H}$ and the magnetization $\boldsymbol{M}$ in consideration of the magnetic field constant μ_0.

Combining the Eqs. (2.51), (2.52), and (2.53) we obtain the equation

$$\hat{\mu}_r = \mathbb{1} + \hat{\chi} \tag{2.54}$$

which provides a direct relation between the permeability tensor $\hat{\mu}_r$ and the magnetic susceptibility $\hat{\chi}$, which is a dimensionless measure of the magnetizability.

The susceptibility χ can be used to separate magnetic materials into three types of magnetism. These types are diamagnetism ($\chi < 1$), paramagnetism ($\chi > 1$), and collective magnetism ($\chi \gg 1$). Since there is no unified theory to describe all magnetic phenomena, different models are used which are explained in the following.

Collective magnetism

The collective magnetism is a many-body phenomenon based on the exchange interaction of permanent magnetic moments, which causes a spontaneous magnetic order without applying an external magnetic field. This magnetic order collapses above a critical temperature and a phase transition to paramagnetism occurs.
The exchange interaction can only be accounted for by quantum mechanics. The cause of the exchange interaction is the indistinguishability of identical particles and the consequent symmetry requirements of possible multi-particle wave functions. For fermions like electrons only antisymmetric total wave functions are allowed (Pauli's exclusion principle), which are products of the orbital and the spin wave functions. Thus, products of symmetric orbital and asymmetric spin wave functions and reverse are valid. This can basically be considered

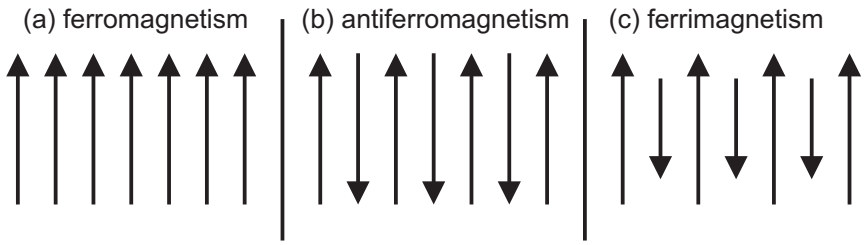

Fig. 2.15: Sketch presenting the order of neighboring magnetic dipole moments of (a) a ferromagnet, (b) an antiferromagnet, and (c) a ferrimagnet.

as a competition between the kinetic and potential energy. An antisymmetric wave function which means that the electron spins are antiparallel aligned requires a symmetric orbital wave function. This way the electrons are in the same orbital but have a high potential energy due to the Coulomb interaction. If the spins are parallel aligned the electrons have to be in different orbitals since the symmetric spin wave function requires an antisymmetric orbital wave function. As a result, the electrons occupy states in the $\boldsymbol{k}$ space (momentum space) with higher kinetic energy. Thus, the Coulomb interaction of the electrons is lower for parallel alignment but their kinetic energy is higher. The overlap of neighboring single-electron wave functions determines which is the dominating energy contribution and whether parallel or antiparallel spin alignment is preferred. Depending on the coupling, the collective magnetism can be separated into three more types. If all spins are parallel aligned to each other, this is called ferromagnetism (cf. Fig. 2.15 (a)). Below the Curie temperature, there is a macroscopic magnetization without an applied external magnetic field. In this case the magnetic susceptibility χ is much greater than one ($\chi \gg 1$) and Eq. (2.53) can be simplified to

$$\boldsymbol{B} = \mu_0 \boldsymbol{M} \quad . \tag{2.55}$$

In a solid, where the discreet energy states of atoms form bands, the spontaneous magnetization can be explained by reference to the density of states. The exchange interaction causes an energy shift of the energy bands, where the shift depends on the spin orientation (up, down). Thus, two energy bands are formed which have a common Fermi energy so that one kind of spin prevails the other kind (cf. Fig. 2.16). The only elements which feature ferromagnetic behavior at room temperature are iron, cobalt and nickel.

Antiferromagnetic substances have also a magnetic order, but the two sublattices of parallel aligned magnetic moments with equal magnitude balance out and the resulting magnetization is zero (cf. Fig. 2.15 (b)). The critical temperature for the phase transition to paramagnetism is called Néel temperature.
If there is a resulting magnetization despite the antiparallel alignment of the two sublattices of parallel aligned magnetic moments, it is called ferrimagnetism. In this case the sublattices have different magnetic magnitudes and a spontaneous magnetization is preserved (cf. Fig. 2.15 (c)). Ferrimagnets have also a Curie temperature.

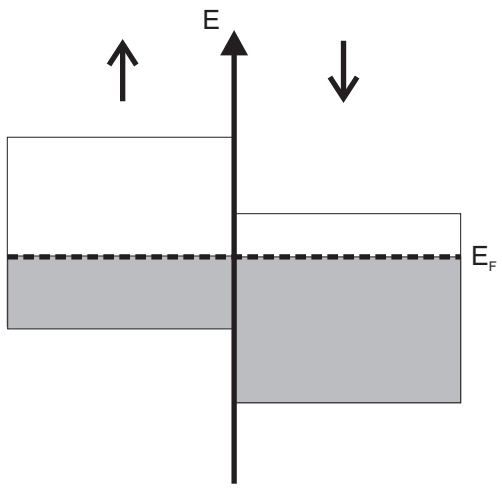

Fig. 2.16: Sketch of the energy bands for spin up and spin down of a ferromagnetic material. The shifted bands for different spins lead to a majority of one spin state if the Fermi level is adequate positioned.

Domain structure and magnetization curve

The consideration of the ferromagnetic coupling was limited so far to the quantum mechanic exchange interaction. The indeed long-range magnetic dipole-dipole interaction can not explain the spontaneous order of neighboring spins since it is weaker than the exchange interaction. However, the dipole-dipole interaction can not be neglected in a solid due to the large number of spins. Thus, a homogeneous spin orientation in the whole solid is unfavorable. Although the short-range exchange interaction can locally induce a ferromagnetic order, the dipole-dipole interaction dominates on a large scale. As a result, many small domains of homogeneous spin orientation are formed whose magnetic magnitudes offset each other to minimize the total energy. The minimizing of the dipole energy of all spins compensates the increase of the exchange energy of the few spins at the border of the domains. In this way, there is no macroscopic magnetization for paramagnetic and diamagnetic materials. The total energy depends substantially on the size of the domains and the structure of the interface. Since an antiparallel alignment of the spins at the transition from domain to domain causes an increase of the exchange energy, the transition is continuous and the domain wall has a finite thickness.
Adding an external magnetic field leads to restructuring of the magnetic domains in the solid. Weak magnetic fields can slightly shift the domain walls, thereby changing the domain size reversibly. However, strong magnetic fields are capable of extending the domains beyond crystallographic defects, which prevent a return to the initial state. Thus, a hysteric behavior if the magnetization curve is observable (cf. Fig. 2.17). Consequently, the magnetization is not just determined by external parameters, but also influenced by its previous history. If the solid is initially demagnetized and then an external magnetic field is applied domain borders shift and domain orientations rotate until a saturation magnetization M_{sat} is reached and all magnetic moments are aligned along the external magnetic field. The irreversibility of this process results in a remaining magnetization M_{rem} after switching off the magnetic field. An opposite magnetic field has to be applied to obtain again an demagnetized solid. In

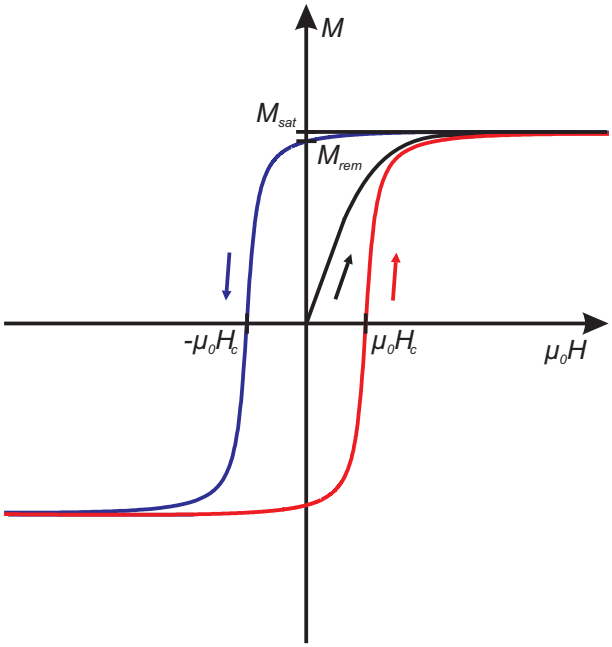

Fig. 2.17: Example of a magnetization curve of a ferromagnet. The magnetization M is plotted against the applied magnetic field strength H. The magnetization of a not magnetized sample increases until the saturation magnetization M_{sat} is reached if an external field is applied (black). If the magnetic field is reduced to zero the ferromagnet has the remanent magnetization M_{rem}. At the coercive field H_c the projection of the magnetization on the magnetic field direction is zero. A saturation value is also reached after reversing the polarity of the magnetic field and increasing its strength (blue curve). Repeated decreasing and reversing the polarity of the magnetic field results in the previous reached saturation value (red curve).

the following, the required magnetic field strength H_c for this purpose is called coercive field. If there is no anisotropy of the free energy density, the equilibrium between exchange energy and magnetic dipole-dipole energy is restored again. Also no magnetization can be detected if the used measurement method is only sensitive to one component of the magnetization (e.g. MOKE) and the magnetization vector is perpendicular to the magnetic field.

Magnetic anisotropies

In general, solids exhibit direction depending magnetic properties so that a distinction of magnetic easy and hard directions is possible. Magnetic easy directions have a large coercive field $H_{c,easy}$ and a high magnetic remanence $M_{rem,easy}$. The direction reversal of the magnetization happens in a narrow magnetic field range so that the magnetization curve has the shape of a box. The magnetic hard directions feature a small coercive field $H_{c,hard}$, a minor magnetic remanence $M_{rem,hard}$, and the magnetization increases or decreases gradually in broad magnetic field range (cf. Fig. 2.18).

A consideration of the free energy density F gives some indication of the magnetic anisotropy of solids. The free energy density consists of the Zeeman energy due to orientation of the magnetization with respect to the external field and several other anisotropy contributions and is calculated as follows

$$F = F_{Zeeman} + F_{shape} + F_{crystal} + F_{uniaxial} + \quad \dots \; . \tag{2.56}$$

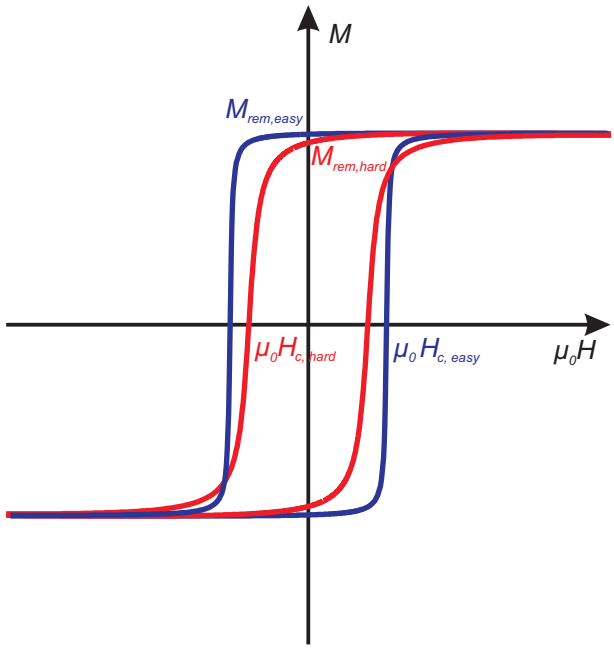

Fig. 2.18: Magnetization curves of the magnetic hard (red) and magnetic easy (blue) direction. The magnetization M is plotted versus the magnetic field strength H. A high magnetic remanence $M_{rem,easy}$ and a high coercive field $H_{c,easy}$ is typical for a magnetic easy direction. The change in magnetization occurs in a narrow magnetic field strength range. Magnetic hard directions exhibit a lower magnetic remanence $M_{rem,hard}$ and a small coercive field $H_{c,hard}$.

Magnetic easy directions are local minima of the free energy density while local maxima are responsible for magnetic hard directions. Although the free energy density possibly depends on more contributions to the magnetic anisotropy like the magnetoelastic anisotropy only the most important contributions are explained in the following.

Zeeman energy

A solid with the magnetization $\boldsymbol{M}$ in an external magnetic field has the potential energy density F_{Zeeman}, the Zeeman energy. The Zeeman energy is given by

$$F_{Zeeman} = -\boldsymbol{M} \cdot \boldsymbol{H} \tag{2.57}$$

and is minimal if the magnetization is parallel aligned to the external magnetic field. If a solid has only this energy contribution then it is magnetic isotropic. In this case, the magnetization is always able to follow the external magnetic field since $\boldsymbol{M} \| \boldsymbol{H}$ is the configuration of minimal energy.
The coordinate system shown in Fig. 2.19 is used to describe the orientation of the magnetization and the external magnetic field. Here, the direction of the magnetization is defined by the azimuthal angle φ and the polar angle ϑ, while the direction of the external magnetic field is determined by the angles φ_H and ϑ_H. The polar angles are with respect to the crystallographic [001] direction (surface normal), while the azimuthal angles are measured with respect to the crystallographic [010] direction in the (001) plane.
In this coordinate system the Zeeman energy can be described with

$$F_{Zeeman} = -M \cdot H \left[\sin\vartheta \sin\vartheta_H \cos(\varphi - \varphi_H) + \cos\vartheta \cos\vartheta_H\right] \tag{2.58}$$

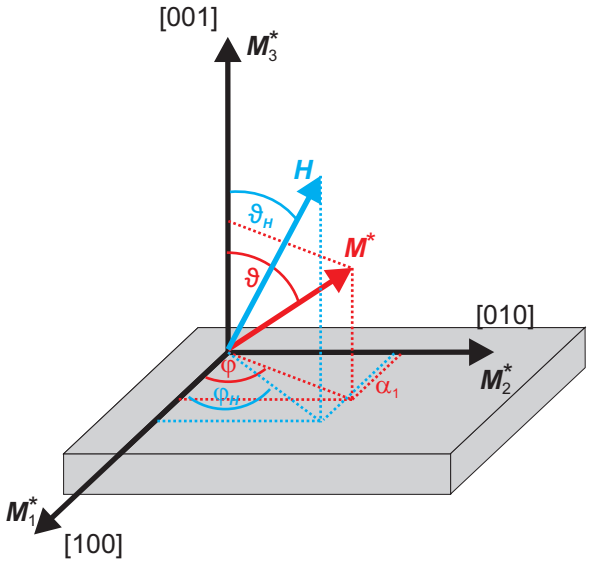

Fig. 2.19: Depiction of the direction cosine α_i (i=1,2,3). The vector $\boldsymbol{M}^* = \boldsymbol{M}/M_{sat}$ is the unit vector of the magnetization. The unit vectors $\boldsymbol{M}_j^*$ (j = 1,2,3) define the coordinate system and are used in the following sections. The direction of the external magnetic field is defined by the angles ϑ_H and φ_H while the direction of the magnetization is described by ϑ and φ.

Assuming that $\boldsymbol{M}$ is always parallel to $\boldsymbol{H}$ Eq. (2.58) can be simplified to:

$$F_{Zeeman} = -M \cdot H \left[\sin^2\vartheta \ \cos\varphi + \cos^2\vartheta\right] \quad . \tag{2.59}$$

Shape anisotropy

The interaction between magnetic dipoles in shaped solids results in the shape anisotropy. At the surface of such solids are uncompensated dipoles, which are not completely surrounded by adjacent dipoles. Thus, a stray field or degaussing field $\boldsymbol{H}_{deg}$ is created which is in opposite direction to the external magnetic field. The contribution of the degaussing field to the free energy density is through integration given by

$$F_{shape} = -\mu_0 \int \boldsymbol{H}_{deg} d\boldsymbol{M} \quad . \tag{2.60}$$

It is possible to describe the degaussing field with the degaussing tensor $\hat{N}$ with

$$\boldsymbol{H}_{deg} = -\hat{N}\boldsymbol{M} \tag{2.61}$$

where the degaussing tensor for thin films is

$$\hat{N} = N_{ij} \quad . \tag{2.62}$$

Since the lateral expansion of thin films is huge compared to its thickness, the lateral components of the degaussing field can be neglected and treated as zero. It follows that $\boldsymbol{H}_{deg} = (0, 0, M_z)$ with $M_z = M_{sat}\cos(\vartheta)$. So the contribution of the shape anisotropy to the free energy density can be simplified to

$$F_{shape} = 2\pi M^2 \cos^2\vartheta \quad . \tag{2.63}$$

If the magnetization is parallel aligned to the surface ($\vartheta = 90°$), the shape anisotropy is minimal.

Magnetocrystalline anisotropy

Due to the spin orbit coupling, the spins of the electrons are correlated to the crystal lattice. A rotation of the interconnected spins causes a torque which affects the orbital moments. If the electron distribution is anisotropic, the induced rotation of the orbital moments is energy dependent since the overlap of the wave functions changes. Thus, the symmetry of the lattice determines the magnetocrystalline anisotropy. A quantitative description is realized by a series expansion of the components of the magnetization direction related to the crystal axes and direction cosines are used for this purpose. For cubic systems, $F_{crystal}$ is given by

$$\begin{aligned} F_{crystal} &= K_4(\alpha_1^2\alpha_2^2 + \alpha_2^2\alpha_3^2 + \alpha_3^2\alpha_1^2) + K_6\alpha_1^2\alpha_2^2\alpha_3^2 \\ &\quad + K_8(\alpha_1^4\alpha_2^4 + \alpha_2^4\alpha_3^4 + \alpha_3^4\alpha_1^4) + \quad ... \end{aligned} \tag{2.64}$$

with the anisotropy constants K_j ($j = 2n{+}4$) [47]. In general, for thin films the magnetization is in the plane of the sample surface. As a result, $\alpha_3 = 0$ can be assumed. It can be seen in Fig. 2.19 that $\alpha_1 = \cos(\varphi)$ and $\alpha_2 = \sin(\varphi)$. Thus, Eq. (2.65) can be simplified to

$$F_{crystal} = K_4\alpha_1^2\alpha_2^2 + K_8\alpha_1^4\alpha_2^4 \tag{2.65}$$

$$= K_4\cos^2\varphi\sin^2\varphi + K_8\cos^4\varphi\sin^4\varphi \tag{2.66}$$

$$= \frac{1}{4}K_4\sin^2 2\varphi + \frac{1}{16}K_8\sin^4 2\varphi \qquad \ldots \ . \tag{2.67}$$

In the case of cubic crystal lattices, the magnetocrystalline anisotropy of thin magnetic films features both a magnetic fourfold symmetry with an anisotropy constant K_4 and a magnetic fourfold symmetry with an anisotropy constant K_8.

Uniaxial magnetic anisotropy

The growth process of a magnetic film on a substrate can also influence its magnetic properties. Mechanical tensions caused by the lattice mismatch and a high substrate roughness can induce an uniaxial magnetic anisotropy. Reasons can also be oblique evaporation and the presence of

a magnetic field during the film growth. The uniaxial magnetic anisotropy can be described by

$$F_{uniaxial} = K_u \sin^2(\varphi - \varphi_u) \tag{2.68}$$

where φ_u is the angle between a crystal axis and the direction of the minimal energy of the uniaxial magnetic anisotropy. K_u is the anisotropy constant of the uniaxial magnetic anisotropy.

Interface anisotropy

Due to the symmetry break of the crystal structure at the interfaces of thin films there is a interface anisotropy caused by the spin-orbit interaction. The interface anisotropy can be of various kinds. For ultra thin films it can be stronger than the shape anisotropy and generate a preferred out-of-plane magnetization. It it also possible that the interface anisotropy is stronger than the magnetocrystalline anisotropy resulting in a rotation of the magnetic easy axes. In both cases the magnetocrystalline anisotropy coefficients K (K_4 and K_8) are composed by a volume contribution K^V and an interface contribution K^S depending reciprocal on the thickness t of the film. The effective magnetocrystalline anisotropy coefficient summarizing both contributions is given by

$$K^{eff} = K^V + \frac{2}{t} K^S \quad . \tag{2.69}$$

The factor two is due the consideration of both film surface and film/substrate interface.

Exchange bias

Another possibility to modify the magnetic properties of a ferromagnetic film (FM) is the coupling to an antiferromagnetic film (AF) which can induce the exchange bias effect. In this case, the magnetic moments at the interface are pinned in one direction and the reversal process of the magnetization is asymmetric with respect to the orientation of the external magnetic field. Thus, the absolute values for positive and negative external magnetic field for reaching the magnetic saturation are shifted by an exchange bias field $\mu_0 H_{eb}$ (cf. Fig. 2.20). In addition, the coercive field is increased to $\mu_0 H_c^{eb}$. It generates a unidirectional magnetic anisotropy since this effect is unidirectional. It has to be considered that the strength of this effect depends on the orientation of the used antiferromagnetic material. While the surface plane of NiO(001) is spin compensated, the surface plane of NiO(111) is polar with a residual magnetic moment [48,49] (cf. Fig. 2.21). Therefore, it is expected that there is no pinning effect in the ferro(i)magnetic film grown on the spin compensated NiO(001). However, an exchange bias effect is here observable as well due to the usually imperfect surface structure [50,51].

The exchange bias effect also occurs in the Fe_3O_4/NiO system which is presented in this thesis since Fe_3O_4 is ferrimagnetic and NiO is antiferromagnetic. Such a bilayer system can be used in a magnetic tunnel junction (MTJ). MTJs consist basically of two ferromagnetic films (electrodes) which are separated by a non-magnetic insulating film, the tunnel barrier.

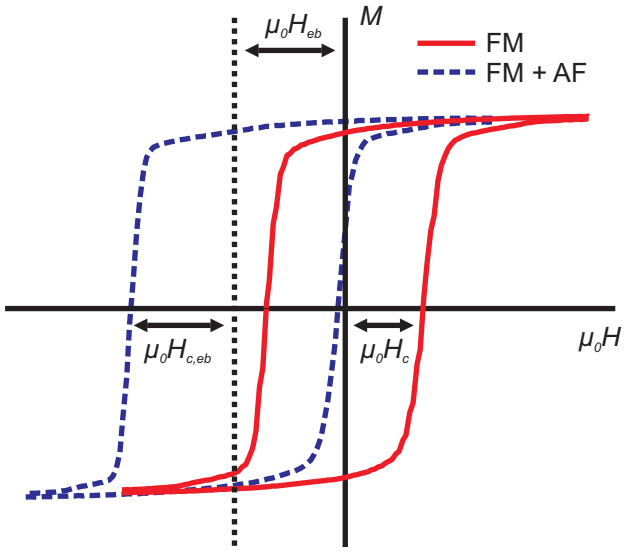

Fig. 2.20: Magnetization curves of a single ferromagnetic film and a bilayer consisting of an antiferromagnetic (AF) and a ferromagnetic (FM) film. The coercive field $\mu_0 H_{c,eb}$ of the bilayer is increased compared to the coercive field $\mu_0 H_c$ of the single ferromagnetic film and an additional exchange bias field $\mu_0 H_{eb}$ occurs.

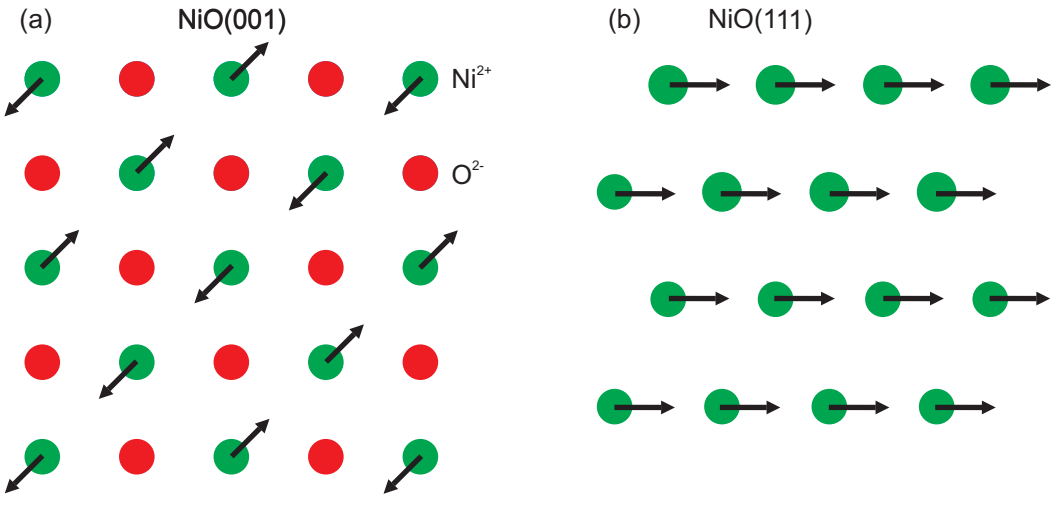

Fig. 2.21: Sketch of the (a) NiO(001) and (b) NiO(111) surface. While the NiO(001) surface is spin compensated the NiO(111) surface is spin uncompensated.

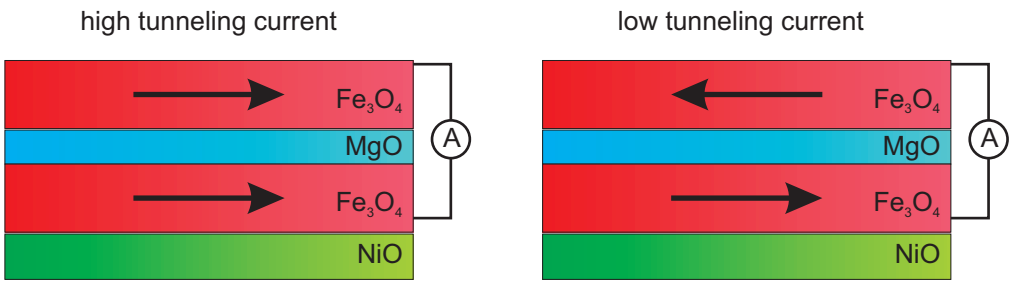

Fig. 2.22: Schematic drawing of a magnetic tunnel junction consisting of two ferrimagnetic Fe_3O_4 electrodes separated by a thin insulating MgO film. One of the Fe_3O_4 electrodes is grown on an antiferromagnetic NiO film. As a result, the exchange bias effect occurs at the interface of the electrode next to the NiO film. This effect induces an exchange bias field and an increased coercive field which stabilizes the alignment of its magnetization. Thus, the magnetization of both magnetite electrodes can be switched separately at different external magnetic field strengths. Depending on the magnetization alignment there is a high tunneling current or a low tunneling current.

The tunnel probability strongly depends on the alignment of the magnetization in the ferromagnetic films. While there is a high tunnel probability for parallel alignment, there is a low tunneling current if the magnetization is antiparallel aligned (cf. Fig. 2.22). The antiparallel and parallel alignment is usually realized by keeping the magnetization alignment of one electrode constant while switching the magnetization alignment of the other electrode. However, if both electrodes are made of the same material they also have the same switching fields. In this case, the exchange bias effect can be utilized to shift the coercive field of one of the Fe_3O_4 electrodes. Thus, it is possible to separately switch the magnetization of the two electrodes to enable an alternation of the magnetization alignment between parallel and antiparallel. In addition, the magnetization alignment in this electrode is stabilized due to the increased coercive field.

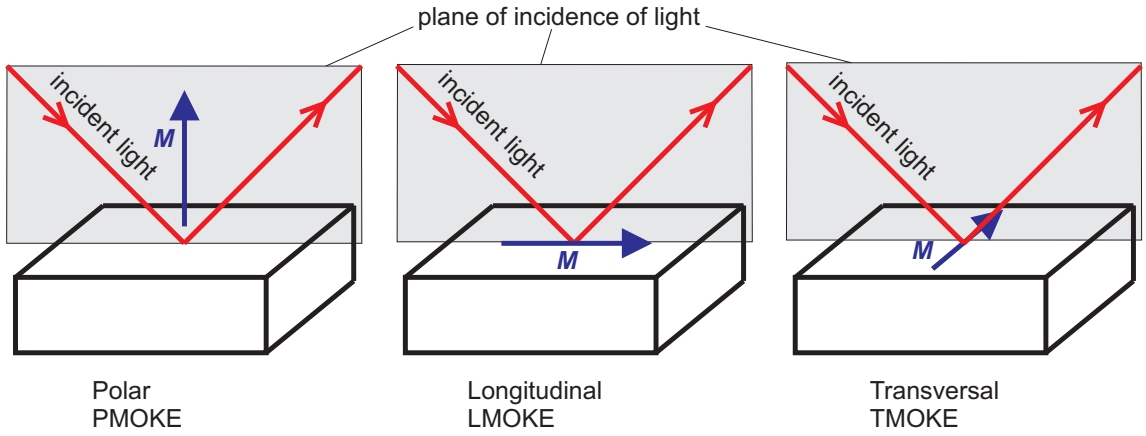

Fig. 2.23: Schematic diagram of the different types of MOKE. One distinguishes between PMOKE, LMOKE and TMOKE depending on the relative position of the magnetization to the plane of incidence of light and the sample surface.

2.8 Magnetooptic Kerr effect

The magnetooptical Kerr effect (MOKE) denotes the rotation of the polarization of linear polarized light after the reflection at a magnetized surface and was discovered by John Kerr [52] in 1876. As shown in the following sections, the rotation angle of the polarization is proportional to the strength of the magnetization. Thus, qualitative statements about the magnetization are possible using the rotation angle (Kerr angle). Furthermore, the Kerr angle can be measured as a function of the applied external magnetic field. The obtained magnetization curves can be used to determine the coercive field and the magnetic remanence.

Types of MOKE

Depending on the relative position of the magnetization to the sample surface and to the plane of incidence of light there are basically three types of MOKE geometries which are illustrated in Fig. 2.23.

- **Polar MOKE (PMOKE)**
  The polar MOKE occurs if the magnetization is perpendicular to the sample surface and parallel to the plane of incidence of light. The polarization of light is rotated (Kerr rotation) and elliptic after the reflection at the sample surface. The PMOKE increases with decreasing incidence angle regarding the surface normal.
- **Longitudinal MOKE (LMOKE)**
  In this case the magnetization is both parallel to the sample surface and parallel to the plane of incidence of light. A Kerr rotation and a change of the ellipticity of the polarization can be observed as well. However, the LMOKE decreases with decreasing incidence angle regarding the surface normal.
- **Transversal MOKE (TMOKE)**
  The transversal MOKE can be studied if the magnetization is parallel to the sample surface and perpendicular to the plane of incidence of light. In contrast to PMOKE

and LMOKE there is no modification of the polarization of light but a change of the measured light intensity.

Hybrid forms of these effects are detected if the magnetization is not exact parallel or perpendicular to the plane of incidence of light and the sample surface. The effects of the PMOKE and LMOKE which both alter the same properties of light can be separated afterwards.

MOKE geometries

In general, the described types of MOKE have to be distinguished from the so-called MOKE geometries. While the different types of MOKE are defined by the relative position of the magnetization to the sample surface and the incidence plane of light, the MOKE geometries are defined by the position of the external magnetic field $\boldsymbol{H}$. A distinction between the types of MOKE and MOKE geometries is useful since the magnetization does not necessarily follow the external magnetic field especially for weak field strengths due to existing magnetic anisotropies. Thus, it is possible that several types of MOKE can occur simultaneously while using one MOKE geometry. The nomenclature of the MOKE geometries is ensued analogously to the types of MOKE.

Kerr angle and Kerr ellipticity

The experimentally obtained measured values are the Kerr angle θ_K and ellipticity angle ϵ_K, which is a measure of the Kerr ellipticity e_K. The Kerr angle is defined as the angle between the incident linear polarized light $\boldsymbol{E_i}$ and the semi-major axis of the reflected elliptic polarized light $\boldsymbol{E_{f,max}}$ (cf. Fig. 2.24). The ellipticity of the reflected light is determined by the Kerr ellipticity with

$$e_K = \tan(\epsilon_K) = \frac{\boldsymbol{E_{f,min}}}{\boldsymbol{E_{f,max}}} \tag{2.70}$$

where $E_{f,min}$ and $E_{f,max}$ constitute the half axes of the ellipse. For very small angles $e_K = \epsilon_K$ is approximately valid. The combination of the Kerr angle θ_K and the Kerr ellipticity e_K results in the complex Kerr angle

$$\phi_K = \theta_K + ie_K \tag{2.71}$$

which is proportional to the magnetization of the sample [53,54]. With the Jones-matrix formalism [55] the reflection of the light at the sample can be described by the following matrix

$$\hat{R} = \begin{pmatrix} r_{ss} & r_{sp} \\ r_{ps} & r_{pp} \end{pmatrix} \quad . \tag{2.72}$$

The entries in the matrix are the complex reflection coefficients for perpendicular (s) and parallel (p) polarized light with respect to the plane of incidence of light. The diagonal elements describe the modification of perpendicular or parallel polarization in the same direction. The addition of a p-polarized part to a s-polarized and vice versa is realized by the non-diagonal elements. Thus, a modification of the polarization direction is describable.

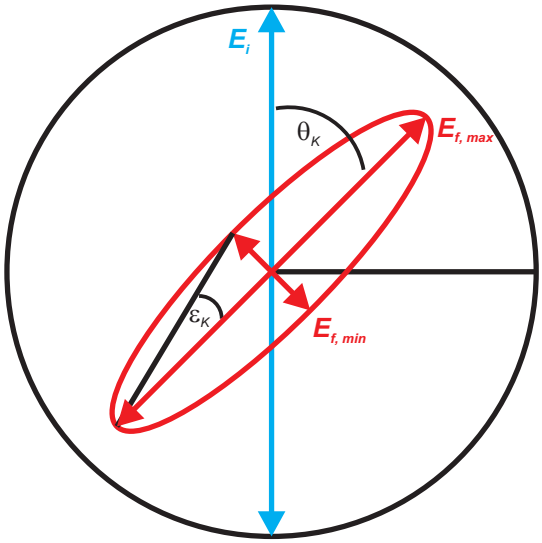

Fig. 2.24: Incident linear polarized light (blue) is modified by reflection at a surface. The polarization of the reflected light is rotated and elliptic (red). The Kerr angle θ_K corresponds to the difference of angles between the polarization axes. A measure for the ellipticity is the ellipticity angle ϵ_K.

The complex Kerr angles can be determined by [56]

$$\phi_s = -\frac{r_{ps}}{r_{ss}} \text{ or } \phi_p = \frac{r_{sp}}{r_{pp}} \ . \tag{2.73}$$

The complex reflection coefficients depend on the dielectricity tensor $\hat{\epsilon}$ which describes the interaction of matter with electromagnetic waves. The non-diagonal elements of this tensor are proportional to the magnetic flux density $\boldsymbol{B}$, which is according to Eq. (2.55) proportional to the magnetization of the sample. Thus, it applies the following

$$\phi_s = -\frac{r_{ps}}{r_{ss}} \propto \epsilon_{i,j} \propto B \propto M \text{ or } \phi_p = \frac{r_{sp}}{r_{pp}} \propto \epsilon_{i,j} \propto B \propto M \ . \tag{2.74}$$

The proportionality factor between $\phi_{s/p}$ and M is material-dependent so that the Kerr angle can not be used to compare the magnetizations of two samples.

Separation of linear and quadratic MOKE

The previous sections describe only linear dependencies on the magnetization. However, theoretical calculations in 1965 and experiments in 1990 have shown that the terms of the second order have to be considered for the correct description of the MOKE for some materials [57, 58]. The second order effects of the MOKE are referred to as quadratic MOKE (QMOKE), while the first order contributions are designated as linear MOKE (LinMOKE). The LinMOKE has to be separated from the QMOKE since the pure proportionality to the magnetization shown in section 2.8 is only valid if there is no QMOKE and the magnetization is strictly in-plane or perpendicular to the external magnetic field .

For films with the film thickness

$$D \ll \frac{\lambda}{4\pi n} \tag{2.75}$$

where λ is the wavelength of the incident light and n is the refraction index of the reflecting material, according to Hamrle et al. [56] the complex Kerr angles are given by

$$\phi_s = -\frac{r_{ps}}{r_{ss}} = A_s \left(\epsilon_{21} - \frac{\epsilon_{23}\epsilon_{31}}{\epsilon_d} \right) + B_s \epsilon_{31} \tag{2.76}$$

or

$$\phi_p = \frac{r_{sp}}{r_{pp}} = -A_p \left(\epsilon_{12} - \frac{\epsilon_{32}\epsilon_{13}}{\epsilon_d} \right) + B_p \epsilon_{13} \ . \tag{2.77}$$

The dependency of the incidence angle and the refraction index are contained in the coefficients $A_{s/p}$ and $B_{s/p}$. The $\epsilon_{i,j}$ are the elements of the dielectricity tensor. The constant ϵ_d is the diagonal element of the zero order tensor. A detailed description of the second order tensor for cubic systems can be found in Ref. [59]. The relations for $\phi_{s/p}$ shown in Ref. [56] are generalized for tetragonal systems and any orientation of the magnetization by Kuschel et al. [60] into

$$\begin{aligned} \phi_{s/p} = &\pm B_{s/p} K_{31} M_2 - A_{s/p} K_{12} M_3 \\ &\pm A_{s/p} \left(2G_{66} + \frac{\Delta G}{2}(1 - \cos(4\alpha)) - \frac{K_{31}^2}{\epsilon_d} \right) M_1 M_2 \\ &\mp A_{s/p} \frac{\Delta G}{4} \sin(4\alpha)(M_2^2 - M_1^2) + B_{s/p} G_{44} M_3 M_1 \ . \end{aligned} \tag{2.78}$$

Here, the angle α is between the applied magnetic field and a magnetic easy axis of the cubic or tetragonal crystal. The magnetooptic anisotropy parameter is given by $\Delta G = G_{11} - G_{12} - 2G_{44}$. The constants K and G correspond to the first order and second order terms of the dielectricity tensor. According to Ref. [59] for cubic crystal systems $K_{12} = K_{31}$, $G_{12} = G_{13} = G_{31}$, and $G_{44} = G_{66}$ apply. The linear terms which are proportional to M_2 and M_3 cause the LMOKE and PMOKE, respectively, so that the proportionality between the Kerr angle and the magnetization shown in Eq. (2.74) is only partly valid.
The symmetry of the magnetization reversal can be describes by $\boldsymbol{M}_{incr.}(\boldsymbol{H}) = -\boldsymbol{M}_{decr.}(-\boldsymbol{H})$ where $\boldsymbol{M}_{incr.}(\boldsymbol{H})$ and $-\boldsymbol{M}_{decr.}(-\boldsymbol{H})$ are the magnetization vectors for an increasing or decreasing magnetic field. A symmetrizing or antisymmetrizing of the measured curve of the Kerr angle in dependence of the external magnetic field can be achieved with

$$\phi^{lin/quad} = \frac{\phi_{incr}(\boldsymbol{H}) \mp \phi_{decr}(-\boldsymbol{H})}{2} \ . \tag{2.79}$$

With Eq. (2.79), Eq. (2.78) can be separated into the LinMOKE part (subtraction)

$$\phi_{s/p}^{lin}(H) = \pm B_{s/p} K_{31} M_2 - A_{s/p} K_{12} M_3 \tag{2.80}$$

and the QMOKE part (summation)

$$\begin{aligned}\phi_{s/p}^{quad}(H) = &\pm A_{s/p}\left(2G_{66} + \frac{\Delta G}{2}(1-\cos(4\alpha)) - \frac{K_{31}^2}{\epsilon_d}\right) M_1 M_2 \\ &\mp A_{s/p}\frac{\Delta G}{4}\sin(4\alpha)(M_2^2 - M_1^2) + B_{s/p} G_{44} M_3 M_1 \quad .\end{aligned} \tag{2.81}$$

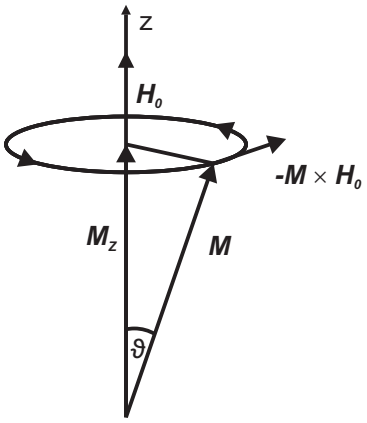

Fig. 2.25: Precession cone of the magnetization with driving field $\boldsymbol{H}_0$. The opening angle ϑ is magnified for a better view.

2.9 Ferromagnetic resonance

The ferromagnetic resonance (FMR) is based on the same principles as the electron paramagnetic resonance (EPR), but instead of paramagnetic materials ferromagnetic materials are investigated. First, for the simplified explanation, there are no internal magnetic fields ($\boldsymbol{H}_{int}$=0) and no anisotropy fields ($\boldsymbol{H}_K$=0). If a static external magnetic field is applied to a sample, a torque is exerted to the magnetic moments $\boldsymbol{\mu}$ in the sample so that they start to precess like gyroscopes around the axis of the magnetic field ($\boldsymbol{H}_0$) (Larmor precession). Here, the change of the magnetic field when switching on is already the trigger. In thin ferromagnetic films all magnetic moments are arranged parallel to each other so that the sum of all magnetic moments in the volume are given by the magnetization $\boldsymbol{M}$. The precession of the magnetization $\boldsymbol{M}$ around the axis of the magnetic field is shown in Fig. 2.26. It will not stop without any damping. The corresponding equation of motion without damping is given by

$$\frac{\partial \boldsymbol{M}}{\partial t} = -\gamma \left[\boldsymbol{M} \times \boldsymbol{H}_0\right] \quad \text{with} \quad \gamma = \frac{g\mu_B}{\hbar} = g\frac{e}{2mc} \tag{2.82}$$

where g is the Landé g-factor and γ the gyromagnetic ratio [61]. The solution of the equation of motion leads to the Larmor frequency $\omega = \gamma \boldsymbol{H}_0$ at which the magnetization $\boldsymbol{M}$ rotates around the z-axis defined by $\boldsymbol{H}_0$.
Quantum mechanically, the external magnetic field causes also a splitting of the energy levels in the atom (Zeeman effect) which is shown schematically for a twofold degenerated energy level with $S = \frac{1}{2}$ in Fig. 2.26. The size of the splitting depends on the strength of the external magnetic field $\boldsymbol{H_0}$ and is given by $\Delta E = g\mu_B \boldsymbol{H_0}$. Between these splitted energy levels inside a multiplet magnetic dipole transition (M1) can be excited. Considering the selection rule for magnetic transitions $\Delta m = \pm 1$, the exciting electromagnetic wave has to be polarized in one plane perpendicular to the static magnetic field. For typical magnetic fields of an electromagnet in the laboratory, the transition frequencies have to be in the microwave range (1 to 100 GHz). Thus, if a microwave is radiated perpendicular to the magnetic field and the resonance condition

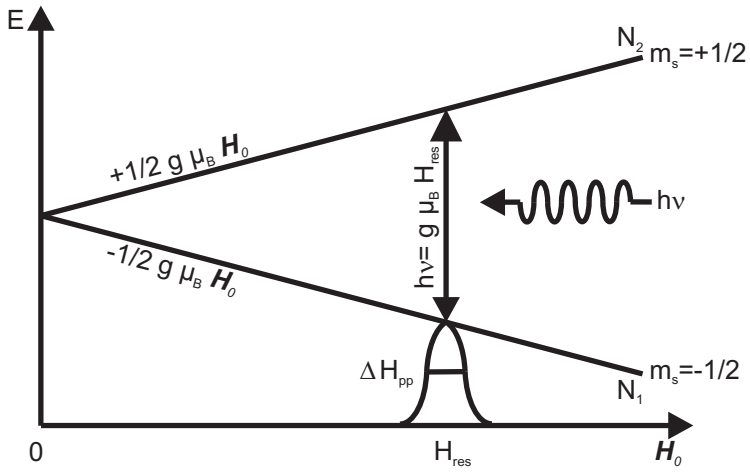

Fig. 2.26: Schematic principle of the FMR. An degenerated energy level is split into two spin levels m_s. Microwave radiation can be used to excite magnetic dipole transitions.

$$h\nu = g\mu_B(H_0 + h_{rf}) \tag{2.83}$$

is fulfilled, absorption can occur (ESR). Here, the magnetic field component $\boldsymbol{h}_{rf}$ of the microwave is also considered. The magnetic field at which the resonance absorption takes place is denoted by H_{res}. This implies for the precession of $\boldsymbol{M}$ an increasing of the angle ϑ. It can be easily seen, that Eq. (2.83) is equivalent to the Larmor frequency.
The resonance condition is more complicated for ferromagnetic materials since additional internal fields are induced by anisotropy fields $\boldsymbol{H}_K$ and the exchange coupling $\boldsymbol{H}_{int}$. Landau and Lifschitz [62] have shown that in this case the expression $\boldsymbol{H}_0 + \boldsymbol{h}_{rf}$ has to be replaced by the effective magnetic field $\boldsymbol{H}_{eff} = \boldsymbol{H}_0 + \boldsymbol{h}_{rf} + \boldsymbol{H}_K$. Thus, the magnetization does not precess around the external magnetic field but around the effective magnetic field. If $\boldsymbol{M} \nparallel \boldsymbol{H}_{int}$, $\boldsymbol{H}_{int}$ modifies as well the effective magnetic field. Since Eq. (2.83) is no longer valid to describe the resonance frequency, a new solution has to be found for Eq. (2.82).
An easy way to calculate the resonance frequency is the approach of Smit and Beljers [63]. This approach was also independently deduced by Suhl [64] and Gilbert [65]. To do this, Eq. (2.82) is converted into spherical coordinates (cf. Fig. 2.19) assuming a constant saturation magnetization M_S=const. and can be described by

$$\frac{d\vartheta}{\partial t} = \gamma \frac{\partial H}{\partial \varphi} \quad \text{and} \quad \frac{d\varphi}{\partial t}\sin(\vartheta) = -\gamma \frac{\partial H}{\partial \vartheta} \tag{2.84}$$

In the thermodynamic equilibrium $\boldsymbol{M}$ is parallel to $\boldsymbol{H}_{eff}$. H_{eff} can be expressed by the free energy density F with

$$H_{eff} = -\frac{\partial F}{\partial M_S}. \tag{2.85}$$

Eq. (2.85) can be used to determine the equilibrium orientation of $\boldsymbol{M}$ which is defined by

the polar angle ϑ and the azimuthal angle φ for which F is minimal using

$$\left.\frac{\partial F}{\partial \vartheta}\right|_{\vartheta} \stackrel{!}{=} 0 \quad \text{and} \quad \left.\frac{\partial F}{\partial \varphi}\right|_{\varphi} \stackrel{!}{=} 0 \ . \tag{2.86}$$

The Eqs. (2.86) are not valid if $\boldsymbol{M}$ differs from the equilibrium position (ϑ, φ) by small deflections

$$\delta\vartheta(t) = \vartheta(t) - \vartheta \quad \text{with} \quad \delta\vartheta \ll \vartheta \ \text{ and} \tag{2.87}$$

$$\delta\varphi(t) = \varphi(t) - \varphi \quad \text{with} \quad \delta\varphi \ll \varphi \ . \tag{2.88}$$

Consequently, $\boldsymbol{M}$ is distracted by a torsional moment caused by the effective magnetic field $\boldsymbol{H}_{eff}$. The linear development of $\frac{\partial F}{\partial \vartheta}$ and $\frac{\partial F}{\partial \varphi}$ gives

$$\frac{\partial F}{\partial \vartheta} = \frac{\partial^2 F}{\partial^2 \vartheta}\delta\vartheta + \frac{\partial^2 F}{\partial\vartheta\partial\varphi}\delta\varphi \tag{2.89}$$

$$\frac{\partial F}{\partial \varphi} = \frac{\partial^2 F}{\partial\varphi\partial\vartheta}\delta\vartheta + \frac{\partial^2 F}{\partial^2 \varphi}\delta\varphi \quad . \tag{2.90}$$

With Eq. (2.82) a linear equation system is given which describes the small oscillations of $\boldsymbol{M}$ around the equilibrium condition

$$-\frac{M}{\gamma}\sin(\vartheta)\frac{\partial(\delta\vartheta)}{\partial t} = \frac{\partial^2 F}{\partial\varphi\partial\vartheta}\delta\vartheta + \frac{\partial^2 F}{\partial^2 \varphi}\delta\varphi \tag{2.91}$$

$$\frac{M}{\gamma}\sin(\vartheta)\frac{\partial(\delta\varphi)}{\partial t} = \frac{\partial^2 F}{\partial^2 \vartheta}\delta\vartheta + \frac{\partial^2 F}{\partial\vartheta\partial\varphi}\delta\varphi \ . \tag{2.92}$$

This homogeneous system of equations has periodic solutions of the form $\delta\vartheta$, $\delta\phi \propto e^{i\omega t}$ if the determinant is zero

$$\frac{\partial^2 F}{\partial\vartheta\partial\varphi}^2 - \frac{\partial^2 F}{\partial^2 \vartheta}\frac{\partial^2 F}{\partial^2 \varphi} + \left(\frac{\omega}{\gamma}\right)^2 M^2 \sin^2(\vartheta) = 0 \ . \tag{2.93}$$

From this equation we obtain the searched resonance equation in the form from Smit and Beljers [63]

$$\omega = \gamma H_{res} = \frac{\gamma}{M\sin(\vartheta)}\left\{\frac{\partial^2 F}{\partial^2 \vartheta}\frac{\partial^2 F}{\partial^2 \varphi} - \frac{\partial^2 F}{\partial\vartheta\partial\varphi}^2\right\}^{\frac{1}{2}} \tag{2.94}$$

Depending on the analyzed material some anisotropy contributions of F can be neglected. Thus, for the data evaluation one has to consider which anisotropy contributions play a role in the investigated system.

3 Material system

3.1 Magnesium oxide

Magnesium oxide (MgO) is a colorless hygroscopic solid mineral. It crystallizes in the rock salt structure with a lattice constant of a_{MgO}=421.17 pm and a density of 3.58 g/cm^3. Both the Mg^{2+} ions and the O^{2-} ions form a face-centered-cubic (fcc) sublattices in this rock salt structure which are shifted by half a lattice constant against each other. Hence, the Mg^{2+} ions are in the octahedral sites of the O^{2-} fcc lattice so that a Mg^{2+} ion is surrounded by six O^{2-} ions and vice versa (cf. Fig. 3.1). The primitive surface unit cell of MgO in the (001) plane is rotated by 45° compared to the bulk unit cell and has a lattice constant of $a_{s,MgO}$=$a_{MgO}/\sqrt{2}$. The vertical layer distance of MgO is $a_{MgO}/2$.
Furthermore, MgO is an insulator with a band gab of 7.8 eV and consequently transparent to visible light. It is diamagnetic and the melting point of MgO is at 2852° C. MgO with an orientation of (001) is used as the substrate for all films presented in this thesis.

3.2 Nickel oxide

Nickel(II) oxide (NiO, cf. Fig. 3.1) has basically the same rock salt structure as MgO, but instead of Mg^{2+} ions there are Ni^{2+} ions in the octahedral sites of the the O^{2-} fcc lattice (cf. Fig. 3.1). NiO has a lattice constant of a_{NiO}=417.69 pm and a density of 6.67 g/cm^3. The surface unit cell of NiO is $a_{s,NiO}$=$a_{NiO}/\sqrt{2}$ and the vertical layer distance of NiO is $a_{NiO}/2$. In principle, NiO is an insulator (band gap between 3.6 eV to 4.0 eV) like MgO and transparent to visible light [66]. In fact, NiO is non-stoichiometric and its color depends on the Ni:O ratio. Stoichiometrically correct NiO is green, while the non-stoichiometric NiO is black. NiO is antiferromagnetic up to the Néel temperature of T_N= 523 K and the melting point is at 1955° C.

3.3 Iron

Iron (Fe) is a transition metal with the symbol Fe and atomic number 26. It belongs to the 8th subgroup of the periodic system of elements and has an electronic configuration of [Ar]3d^{6}4s^2. Pure iron occurs in the three different modifications α-, γ-, and δ-iron. The α-Fe is the thermodynamic most stable modification up to a temperature of T_α = 911° C. It crystallizes in the body-centered cubic crystal structure with a lattice constant of a_{Fe} = 286.65 pm and a vertical layer distance of $a_{Fe}/2$. The lattice constant of the primitive surface unit cell of iron conforms to the lattice constant of its crystal structure. The melting point of α-Fe is at 1538° C, while its density is 7.87 g/cm^3. The ferromagnetic α-Fe becomes paramagnetic above a Curie temperature of T_C = 768° C. The color of iron is lustrous metallic

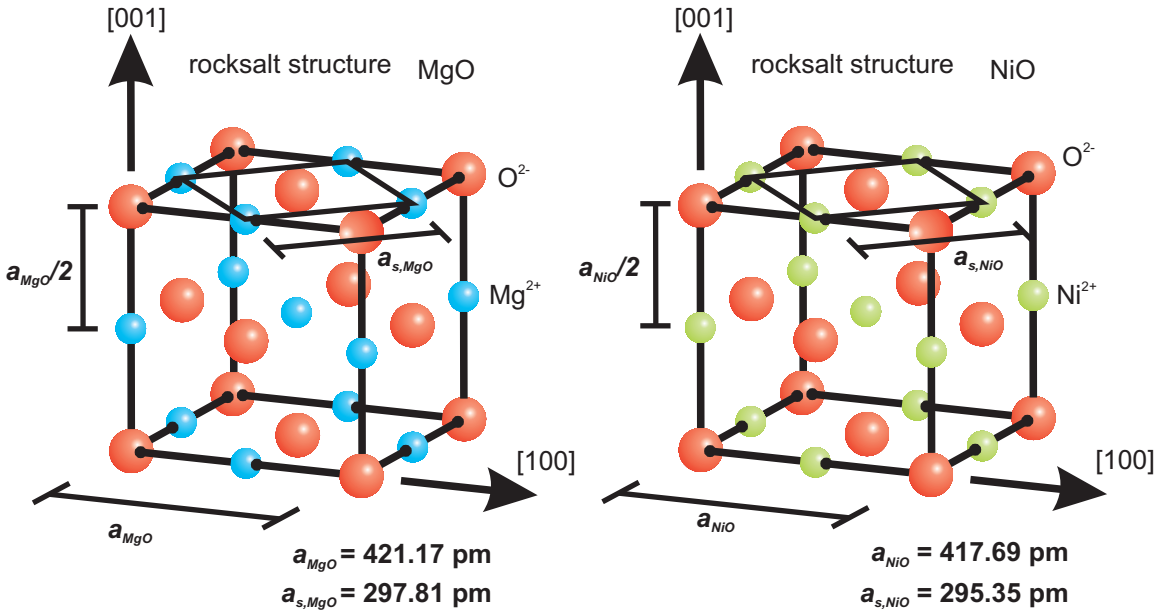

Fig. 3.1: Sketch of the lattice unit cells of MgO and NiO.

with a grayish tinge and is not transparent for visible light.
The most common oxidation states of iron are +2 and +3, however oxidation states from -2 to +6 are also possible. The iron oxides which are likely to grow on MgO(001) are presented in the following.

3.4 Wüstite

Wüstite (FeO) is a non-stoichiometric iron oxide which contains mainly Fe^{2+} ions. Thus, the exact chemical formula is $Fe_{1-\delta}O$. It crystallizes like MgO and NiO in rock salt structure with a lattice constant of 433.2 pm. Therefore, the unit cell and the surface unit cell can be defined analogously to MgO and NiO. If $\delta > 0$ the missing Fe^{2+} ions are compensated by

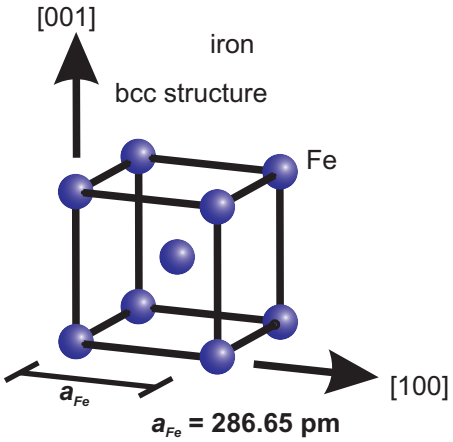

Fig. 3.2: The body centered unit cell of α-Fe.

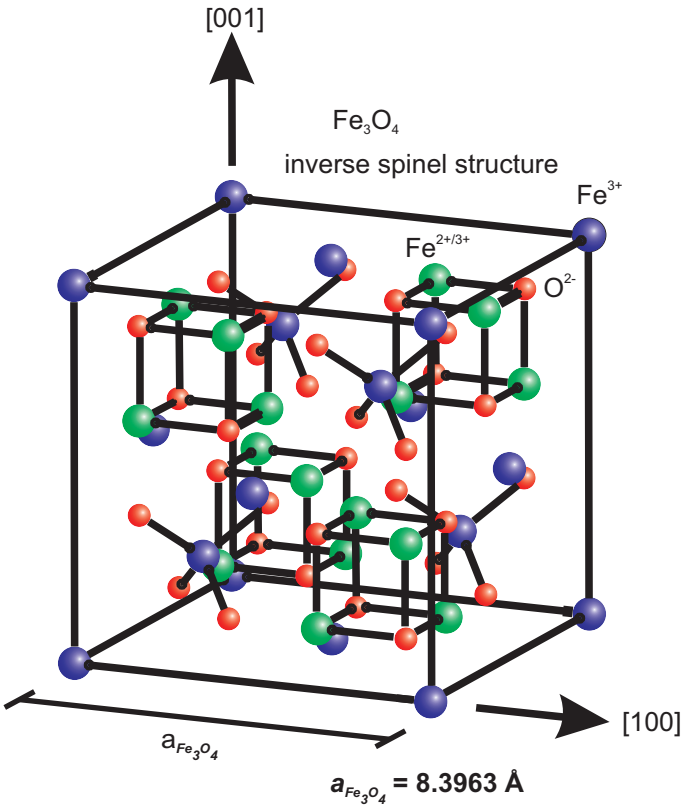

Fig. 3.3: Sketch of the lattice unit cell of magnetite.

Fe^{3+} to preserve the charge balance in the crystal lattice. Wüstite is metastable below 560° C in air and disproportionate to α-Fe and Fe_3O_4. Moreover, wüstite is paramagnetic at room temperature and becomes antiferromagnetic below T_N = -63° C.

3.5 Magnetite

Magnetite (Fe_3O_4) is an iron(II,III) oxide and crystallizes in the inverse spinell structure with a lattice constant of $a_{Fe_3O_4} = 839.64\,\text{pm}$ and a density of $5.2\,\text{g/cm}^3$. The bulk unit cell of magnetite consists of 32 oxygen ions (O^{2-}), which form an fcc sublattice. The 32 octahedral sites of the cation sublattice are half occupied by 8 Fe^{3+} and 8 Fe^{2+} ions forming a 2×1 superstructure for each (001) plane of the sublattice. Both kinds of ions are randomly distributed on these sites. 8 of the 64 tetrahedral sites in the bulk unit cell are occupied by Fe^{3+} ions (cf. Fig. 3.3). Magnetite is ferrimagnetic up to the Curie temperature of T_C = 850° C [67]. The ferrimagnetism originates from different magnetic moments on octahedral and tetrahedral sites coupled antiparallel [5]. The magnetic moments of the Fe^{3+} ions on tetrahedral compensate the antiparallel magnetic moments of the Fe^{3+} ions on octahedral sites. Thus, the magnetic moments of the Fe^{2+} ions on octahedral sites are uncompensated leading to a saturation moment of $4.07\,\mu_B$ [68]. Moreover, magnetite is half-metallic [9] with full spin polarization at the Fermi level.

For bulk magnetite a phase transition occurs at the Verwey temperature $T_V = 125\,\text{K}$. Be-

low T_V magnetite adopts a monoclinic structure, becomes insulating and its susceptibility changes. Thus, the conductivity drops by several orders of magnitude while spontaneous magnetization intensity decreases only minimally if at all. For thin magnetite films, however, the Verwey temperature depends on the film thickness. At $T > T_V$ the magnetic easy axes of bulk magnetite are in $\langle 111 \rangle$ directions due to the magnetocrystalline anisotropy. However, for magnetite thin films the shape anisotropy dominates and the easy axes are in $\langle 110 \rangle$ directions (cf. subsubsection 2.7). As T approaches T_V the magnetocrystalline anisotropy becomes weaker and magnetite is almost isotropic until the phase transition from cubic to monoclinic occurs [69].

3.6 Maghemite and Hematite

Maghemite (γ-Fe_2O_3) is an iron(III) oxide. Thus, it contains solely Fe^{3+} ions. Maghemite crystallizes like magnetite in the inverse spinel structure with a lattice constant of $a_{Fe_2O_3}$ = 835.15 pm and a density of 4.86 g/cm^3. The Fe^{3+} ions occupy $13\frac{1}{2}$ of the octahedral and 8 of the tetrahedral sites of the O^{2-} fcc lattice. Maghemite is ferrimagnetic [70] which is the result of the average excess of Fe^{3+} ions on the octahedral sites leading to a saturation moment of $\approx 2.5\,\mu_B$. The Curie temperature of maghemite is T_C=950 K [71]. Maghemite is a semiconductor with a band gap of 2 eV [72]. It is chemical stable, has a low cost, and is therefore used as a magnetic pigment in electronic recording media since the 1940s [70].

3.7 Antiphase boundaries

During the growth of magnetite or maghemite on MgO(001) frequently antiphase boundaries (APBs) are formed [73–76]. APBs emerge if two islands coalesce which have started to grow at different nucleation centers on a MgO substrate. The doubled size of the magnetite or maghemite lattice constant compared to MgO is the reason for these domain boundaries. As a result, the space between two islands can be smaller than the size of an magnetite or maghemite unit cell and an APB occur (cf. Fig. 3.4). There are several detailed studies on the influence of growth parameters on the density of APBs [73] and the effect of APBs on the properties of magnetite [73, 74]. It was found that the density of APBs is related to the deposition temperature [73] and can be decreased by post-deposition annealing. Another way to lower the density of APBs is a higher deposition rate due to the higher mobility of the ions absorbed at the surface. APBs can suppress the Verwey transition [73, 76] and reduce the magnetization in thin magnetite films [77]. In addition, it is impossible to reach the saturation magnetization even with strong magnetic fields due to APBs [77].

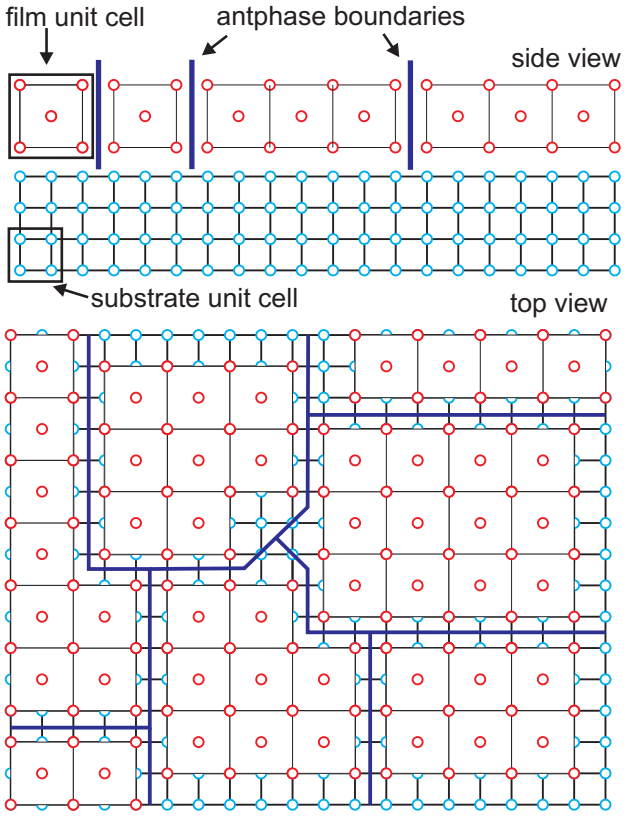

Fig. 3.4: Depiction in side view and top view of a thin film with antiphase boundaries grown on a substrate.

4 Experimental setup

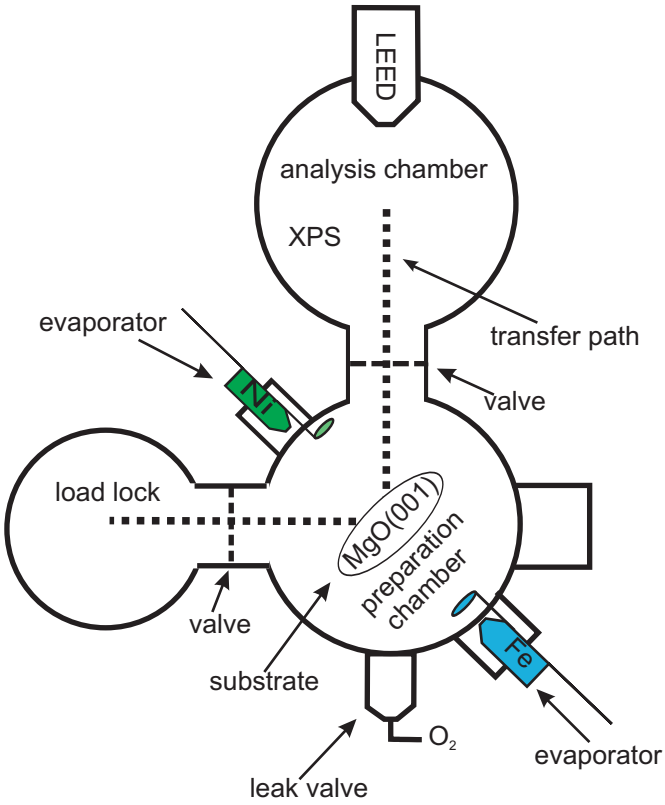

Fig. 4.1: Multi chamber UHV system, which consists of a load lock, a preparation chamber and an analysis chamber. All chambers are separated by valves from each other.

The sample preparation and the *in situ* surface characterization by LEED and XPS were performed in a multi chamber ultra high vacuum (UHV) system. The UHV is necessary to increase the mean free path of the electrons and to minimize the contamination of the substrate surface. The mean free path of electrons and other particles is above 10 cm if the base pressure is below 10^{-3} mbar. A cleaned surface is covered by ad atoms within few seconds at a base pressure of 10^{-6} mbar. A principle drawing of the multi chamber UHV system is depicted in Fig. 4.1. The multi chamber UHV system consists of three single chambers, which are connected by a transfer system. New substrates or fabricated samples are loaded or unloaded via the load lock. The oxide film systems analyzed in this thesis were grown on $10\times10\times0.5\text{mm}^3$ MgO(001) single crystals, which are commercially available from CrysTek GmbH or MaTeck GmbH.
The sample preparation was carried out in the preparation chamber with a base pressure of 10^{-8} mbar. The preparation chamber is equipped with a manipulator and an electron

bombardment based heating system, a high precision leak valve to adjust low oxygen partial pressures, and two evaporators for nickel and iron deposition.

4.1 LEED and XPS setup

The analysis chamber provides a back-view LEED system and an XPS system consisting of a SPECS XR-50 X-ray tube with an Al anode and a Phoibos HSA 150 hemisperical analyzer. The Al K_α line (linewidth 850 meV) with an energy of 1486.6 eV is the dominant photon energy in the emission spectrum of such aluminium tubes. The energy resolution of the analyzer is 0.2 eV.
The setup of a typical XPS experiment is shown in Fig. 4.2 and consists basically of an X-ray source and an energy dispersive electron detector. Either an X-ray tube or synchrotron radiation can be used as X-ray source. To detect the electrons energy-resolved often a hemispherical analyzer is used. In the analyzer, the kinetic energy of the electrons E_{kin} is reduced to $E^{'}_{kin}$ by the work function ϕ_{spec}. Only electrons with the desired kinetic energy $E^{'}_{kin}$ can pass the analyzer. This kinetic energy is also called pass energy. The electrons are detected at the detector by channeltrons. The work function is realized by a lens system where adjustable electric fields are applied which specify the kinetic energy $E^{'}_{kin}$. Considering Eq. (2.48) the binding energy E_B is given by

$$E^{'}_{kin} = E^{kin} - (\phi_{spec} - \phi) \tag{4.1}$$

$$E_B = h\nu - E^{'}_{kin} - \phi_{spec} \ . \tag{4.2}$$

The LEED system is an ErLEED 150 also from the company SPECS. The control unit

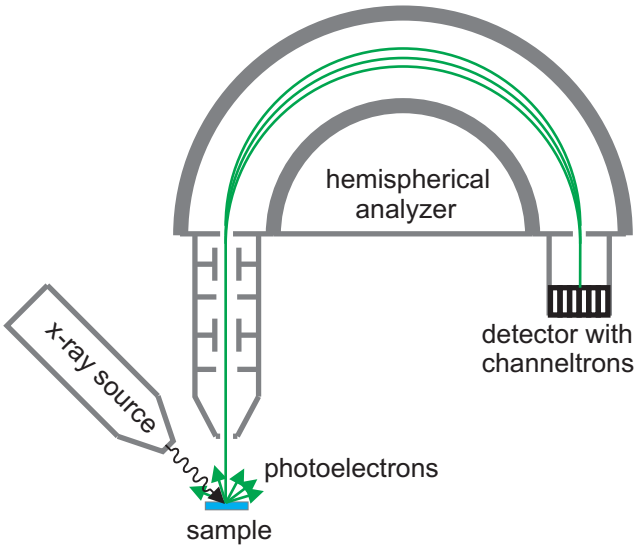

Fig. 4.2: Sketch of a typical XPS setup which basically consists of an X-ray tube and a hemispherical analyzer. The sample is illuminated by X-ray photons. Thus, photoelectrons are emitted from the sample. Only electrons with a certain kinetic energy are allowed to pass the analyzer. These electrons are detected at the detector by channeltrons.

ErLEED 1000A is connected to a computer and the diffracted electrons are mapped to a fluorescence screen using a 3-grid LEED optic. Pictures of the obtained diffraction patterns are taken by a camera which is also connected to the same computer as the LEED control unit. A typical LEED setup consists of an electron source (electron gun) which generates an electron beam with a constant kinetic energy. The electron beam is directed perpendicular to

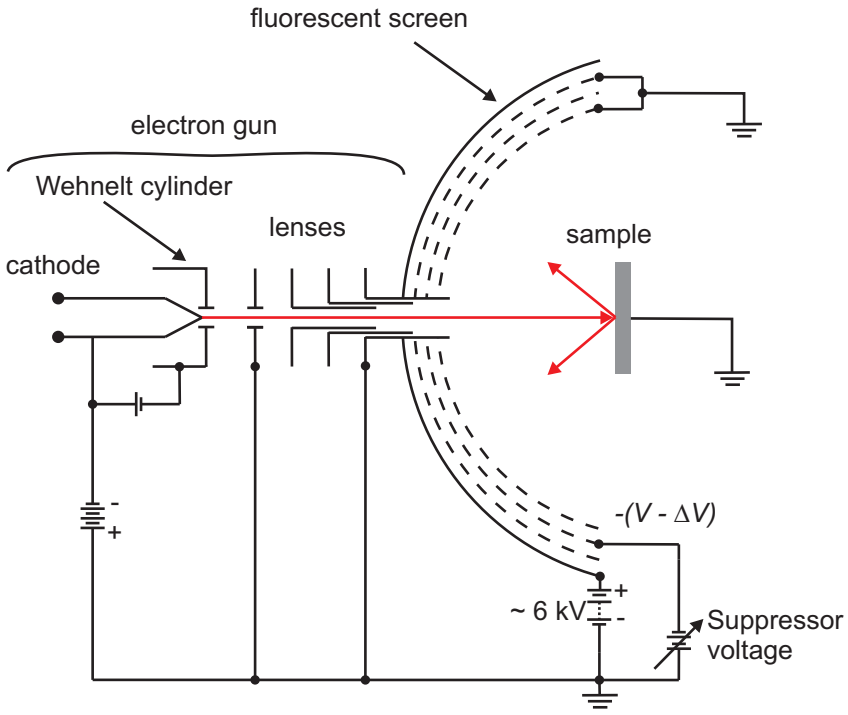

Fig. 4.3: Sketch of a typical LEED setup basically consisting of an electron gun and a fluorescent screen with the three-grid system for background suppression and acceleration.

the sample surface. A spherical fluorescent screen (detector) makes the diffracted electrons visible (Fig. 4.3). The used electron gun has an energy range from 0 to 1000 eV. The electrons are emitted from a filament and are collimated by a Wehnelt cylinder. Subsequently, the electrons are focused and accelerated by an electrostatic lens system. After the low energy electrons are diffracted at the sample surface, the electrons are accelerated with high voltage (≈ 5 keV) to make them visible on the fluorescent screen. In order to minimize the background on the detector the inelastic scattered electrons are suppressed by the negatively charged middle grid (suppressor) of the three-grid LEED system. The other two grids and the first and the last aperture of the lens system are set to ground potential to create a field-free area between the sample and the fluorescent screen system.

4.2 Sample preparation

The films in the presented studies were prepared using different preparation methods described in the following. Prior to the thin film deposition the substrates have been cleaned by heating at 400° C in a 10^{-4} mbar oxygen atmosphere for one hour. This leads to substrates with high crystalline quality and flat surfaces, which have no contamination by impurity atoms as proved by XPS.
The metallic iron films were grown using molecular beam epitaxy (MBE). Here, the substrate is first annealed to the desired deposition temperature and the evaporators are adjusted to deliver a certain deposition rate as measured by an oscillation quartz balance. Both iron and

nickel evaporator are based on electron beam heating. Electrons emitted from a tungsten filament are accelerated by high voltage towards the nickel or iron source. The high voltage is directly applied to the iron or nickel rod. Iron or nickel sublimate before they start to melt due to the UHV conditions. As soon as all parameters are adjusted the evaporator shutter is opened to start the deposition. When the desired film thickness is reached the shutter is closed to stop deposition.
Two methods were used to grow iron oxide. The first method conforms the preparation of metallic iron film except that iron is deposited in an oxygen atmosphere. The evaporated iron atoms react with the oxygen molecules and iron oxide is formed on the substrate. Oxygen partial pressures between $10^{-4}$and 10^{-6} mbar are adjusted using the leak valve. This deposition technique is called reactive molecular beam epitaxy (RMBE).
Another possibility to grow iron oxide is to oxidize a previously grown iron film. Therefore, the iron film was annealed in oxygen atmosphere after preparation.
After each preparation step in-situ LEED and XPS measurements were performed to check the surface structure and the chemical composition of the sample.

4.3 *In situ* distinction of the different iron oxide phases by LEED and XPS

The in-situ characterization by LEED and XPS was used to ensure that the desired material was grown successfully. The comparison of the Fe 2p peak region of the measured sample with reference spectra is a appropriate method to figure out which iron oxide phase is present. The reference spectra of the iron oxide phases wüstite, magnetite and maghemite which are likely to grow on MgO substrates are shown in Fig. 4.4. Furthermore, the Fe 2p spectra of a metallic iron film is depicted in Fig. 4.4 by way of comparison. While wüstite contains solely Fe^{2+} ions, maghemite exclusively comprises Fe^{3+} ions. Both wüstite and maghemite have characteristic charge transfer satellites at 714.7 eV and 718.8 eV, respectively (cf. Fig. 4.4). Magnetite contains bivalent and trivalent iron ions at the ratio of 1/2. Thus, the two charge transfer satellites overlap and form a plateau so that no apparent satellites are visible. This plateau is characteristic of the Fe 2p region of magnetite. The Fe 2p photo emission peaks of the iron oxides are obviously shifted to higher binding energies compared to metallic iron. Due to the absence of oxygen the Fe 2p region of metallic iron exhibits no charge transfer satellites. Besides the analysis of the stoichiometry, the surface structure of the grown iron oxide films can also give a hint which iron oxide phase was grown. Examples for LEED patterns of (a) MgO(001), (b) Fe(001), (c) Fe_3O_4 and (d) Fe_2O_3 are shown in Fig 4.5. Since magnetite and maghemite have a lattice constant which is twice as big as the lattice constant of MgO, the 1×1 structure of magnetite and maghemite has half the size in reciprocal space. The surface structure of magnetite can be distinguished from the surface structure of maghemite by the $(\sqrt{2} \times \sqrt{2})$R45° superstructure which is characteristic feature of magnetite [79–81]. Since wüstite has basically the same crystal structure as MgO they have the same surface structure. Although iron has a bcc structure it has the same surface structure as MgO.

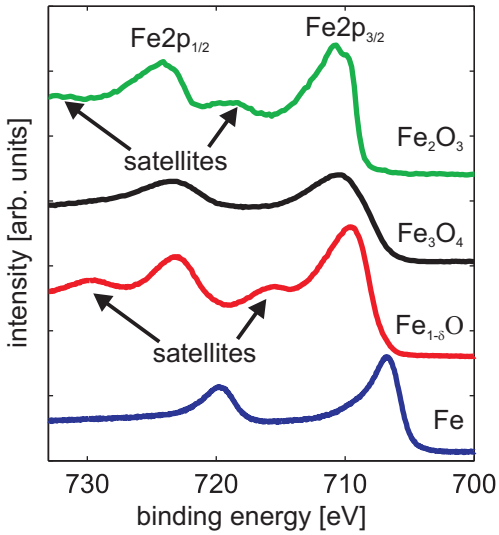

Fig. 4.4: XPS reference spectra of the Fe 2p region of the different iron oxide phases [78].

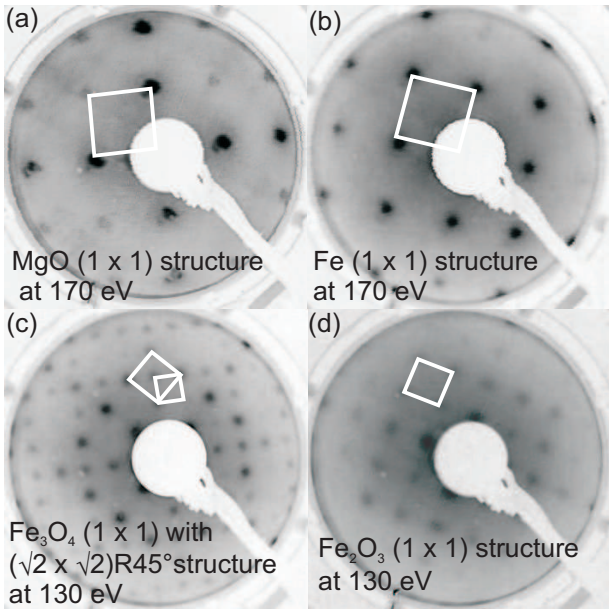

Fig. 4.5: Typical LEED images of (a) a MgO(001) substrate, (b) an Fe(001) film, (c) an Fe_3O_4(001) film, and (d) an Fe_2O_3(001) film. The smallest white square indicate the $(\sqrt{2} \times \sqrt{2})$R45° surface superstructure of the magnetite, while the bigger white squares indicate the (1×1) surface structures.

4.4 MOKE setup

The MOKE experiments are performed with the setup shown in Fig. 4.6. The light source

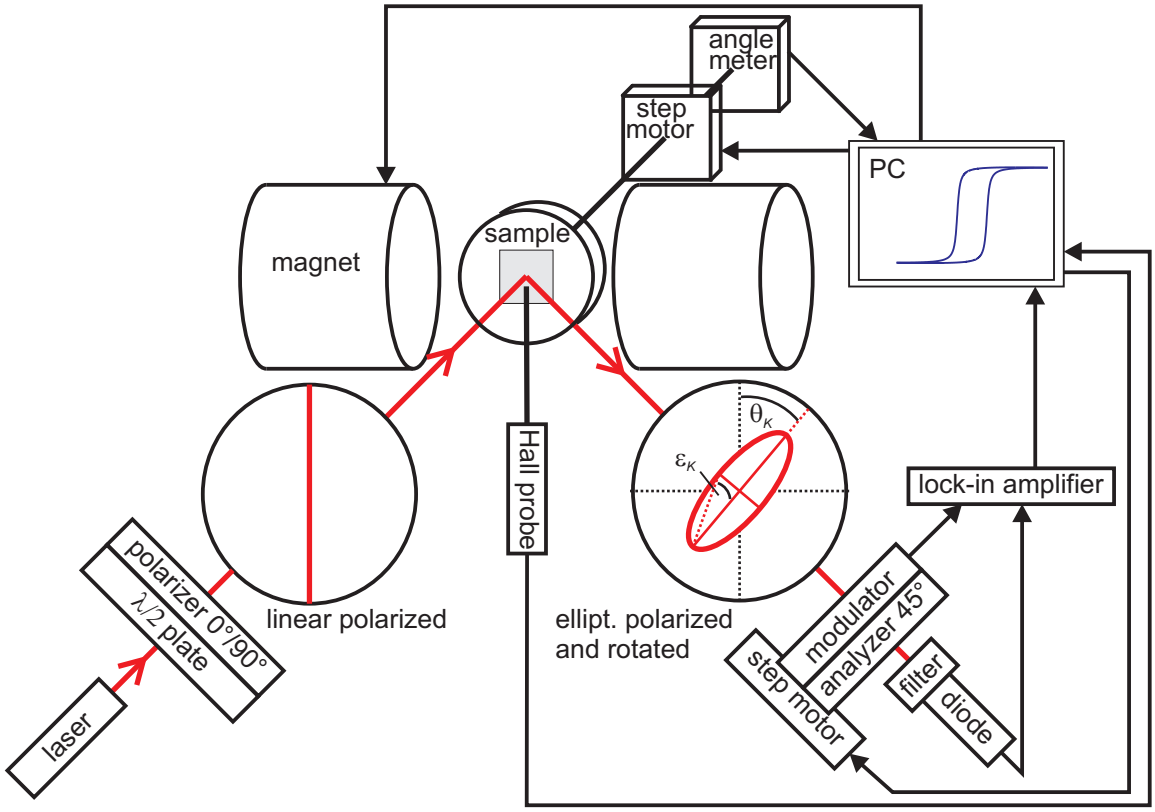

Fig. 4.6: MOKE setup for s- and p-polarized incident light with an external magnetic field parallel to the incidence plane.

is a He-Ne-laser with a wavelength of $\lambda = 632.8$ nm and an incidence angle of 45° to the sample. The intensity of the laser light can be adjusted using a combination of $\lambda/2$ plate and polarizer. In addition, the polarizer can be utilized to switch between p-polarized (0°) and s-polarized (90°) light.
The spatial orientation of the spring mounted sample holders can be varied by adjusting screws. Moreover, the sample holder is rotated by an electromotor and its position is measured by an angle meter (goniometer). Both electromotor and angle meter are controlled by a computer program [82]. The pole shoes of two electromagnets are aligned parallel to the sample surface and perpendicular or parallel to the incidence plane of light. These position of the electromagnets corresponds to the LMOKE and TMOKE geometry, respectively. A Hall probe is mounted close to the sample to determine the magnetic field strength.
The incident laser light is reflected at the sample surface and passes a photoelastic modulator (PEM) and an analyzer before it reaches the photo diode. The PEM consists of a piezo crystal, whose refraction index is modulated by an applied alternating voltage with the frequency Ω. This induces a time-dependent phase shift of the light component parallel to the modulation axis. Thus is described by the modulation $\Delta = \Delta_0 \sin(\Omega t)$. The retardation Δ_0 is attuned to 184° to achieve an optimal signal to noise ratio [83]. The analyzer is rotated by 45° to the

modulation axis of the PEM. As a consequence, the modulated polarization is converted into an intensity modulation and can be detected by the photo diode.

4.5 FMR setup

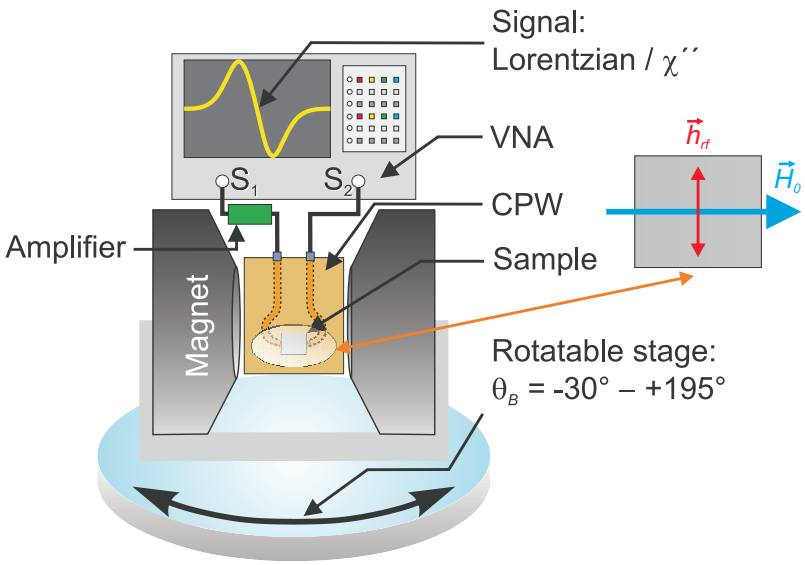

Fig. 4.7: Sketch of the VNA-FMR setup. The geometry of the external magnetic field and the rf field is magnified on the right side. Taken from Ref. [84]

The dynamic characterization was carried out using a broadband vector network analyzer - ferromagnetic resonance (VNA-FMR) setup shown in Fig. 4.7. Therein, the two-port Agilent E8364B VNA acts as source and detector in a frequency range from 10 MHz to 50 GHz. The microwave is coupled from port 2 via an 80 μm wide coplanar waveguide (CPW) to the sample surface. There, it acts as an altering excitation field perpendicular to the external field and parallel to the sample surface causing a precessional motion of the spins. To record the transmission of the sample, the microwave signal is guided to port 1 allowing for the detection of the complex scattering parameter S21. Moreover, a rotation of the sample stage is realized to enable in-plane angle-dependent measurements, whereas out-of-plane angular rotations are realized by the rotary 2.2-T-magnet. Finally, the resonance spectra are obtained by sweeping the external field at fixed frequencies. An example of a measured FMR signal is shown in Fig. 4.8 which is basically the derivation of the actual absorption signal (cf. Fig. 4.8 (inset)). Similar to the MOKE experiments the FMR signal can be measured in dependence on the azimuthal sample rotation to analyze the in-plane anisotropy of the film system.

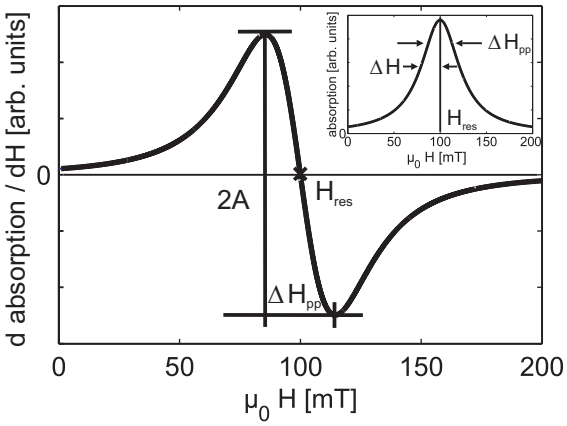

Fig. 4.8: In the ideal case with only Gilbert damping the FMR absorption signal has a lorentzian shape with the maximum at H_{res} (cg. inset). Due to technical reasons mostly the derivation of the adsorption is measured.

4.6 Experimental setup for synchrotron radiation experiments

All X-ray scattering experiments presented in this work were carried out at Deutsches Elektronen-Synchrotron (DESY), Hamburg at PETRA III beamline P08 [85,86] and at DORIS III beamline W1 [34]. Synchrotron radiation is superior to laboratory X-ray sources for thin film investigation due to the higher intensities and, therefore, higher sensitivity as well as higher energy resolution.

4.6.1 Generation of synchrotron radiation

The generation of synchrotron radiation is based on the fact that every accelerated charged particle emits energy in form of electromagnetic waves [87]. The charged particles are usually accelerated in a combination of linear and circular accelerators (cf. Fig. 4.9). At DESY

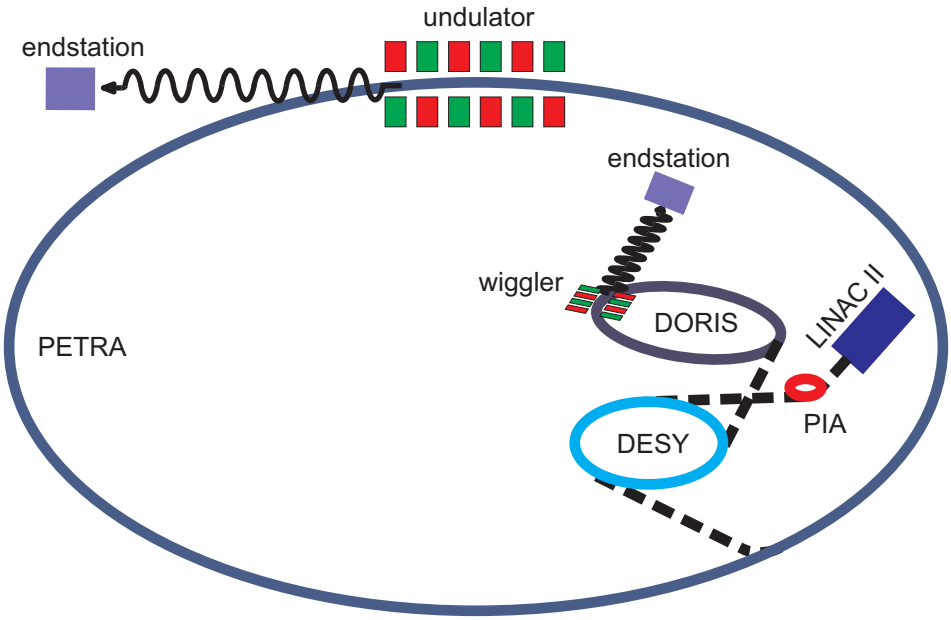

Fig. 4.9: Diagram of the different accelerators at DESY. Generated electrons or positrons are accelerated with the linear accelerator LINAC. Prior to the transfer in Petra III or DORIS III the electrons are accelerated in the booster rings PIA and DESY. Wigglers and undulators are used to generate the radiation for the experiments at the endstations.

the linear accelerator LINAC accelerates the charged particles (positrons or electrons) to a velocity close to speed of light. Due to the limited length of the linear accelerators the kinetic energy of the particles is also restricted. Therefore, the particles are injected into the ring accelerators PIA and DESY to increase the velocity of the particles even further to prepare them for the injection into the storage rings PETRA III or DORIS III. In both the linear accelerator and the ring accelerator the acceleration is achieved by cavity resonators [88]. The energy of the particle beam in the storage ring is finally kept constant which results in a very stable radiated beam. Thus, the spectrum of the emitted radiation is not shifting due to the change of the particle energy.
Modern storage rings have a polygon shape and are not complete circular. The straight

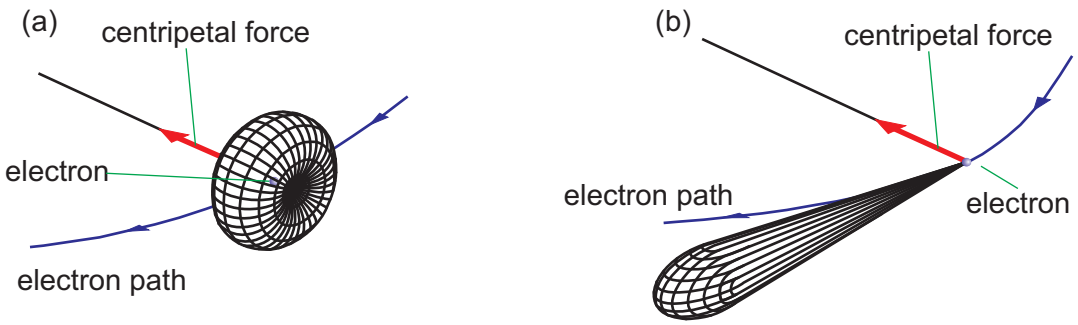

Fig. 4.10: Transformation of the radiation field of an electron traveling along a circular path (a) non-relativistic velocity (b) relativistic velocity. This picture is adapted from Ref. [87] and was revised in Ref. [37].

section of such a polygon are connected by so-called bending magnets which deflect the particles from one straight section into the following one. Due to their relativistic velocity the particles have an altered radiation field compared to particles at non-relativistic velocity (cf. Fig. 4.10). At non-relativistic velocity the radiation of the particles has a toroidal shaped dipole radiation pattern with the main axis pointing into the direction of the accelerating force. For velocities close to the speed of light relativistic effects and the Doppler shift have to be considered. Thus, the radiation field becomes a cone with its center pointing into the direction of propagation (cf. Fig. 4.10).
Only light particles like electrons and positrons are appropriate to generate synchrotron radiation since the emitted radiation is proportional to the particle mass m by the factor $\frac{1}{m^4}$ [87]. Both electrons and positrons collide with the residual gas and generate positive charged particles in the storage ring. Thus, the beam lifetime of positrons is higher since they repel the positive charged particles in their path [89, 90]. However, electrons can be generated easier than antimatter particles such as positrons and for the small particle beam sizes the interaction with the residual gas is negligible. Therefore, currently electrons are used in the storage ring PETRA III. But before DORIS III has been shut down, positrons were used in both DORIS III and PETRA III.
The synchrotron radiation for experimental usage is generated by devices such as bending magnets, wigglers and undulators. The most basic of these devices are the bending magnets. They are placed between straight sections of the polygon shaped storage rings to force the charged particles onto a circular path due to Lorentz force whereby the particles are accelerated and emit radiation. The emitted spectrum of this radiation is continuous and depends both on the bending radius which is determined by the ring geometry and the particle energy. In order to obtain higher beam intensities and smaller beam sizes wigglers and undulators were developed. Both wigglers and undulators consist of periodically alternating magnetic structures, which can be considered as an accumulation of many bending magnets. As a result the particles are forced on an oscillating path emitting radiation at each direction change. Wigglers and undulators can be distinguished by the strength of the magnetic field, the displacement of the particles from its straight path, and their characteristic emission spectra. In a wiggler, the particles have a larger displacement than in an undulator and a wiggler produces a continuous energy spectrum like a bending magnet does, but shifted to higher energies and with larger intensities. The particles oscillate with a smaller amplitude in an undulator, thus, the emitted overlapping waves show constructive or destructive interference

effects. As a result, a typical undulator spectrum exhibit sharp intensity peaks at certain energies and its repetition at higher harmonics. The line spectrum of an undulator can be tuned within a spectra range by variation of the magnetic field which depends on the opening gab of the undulator [90].

4.6.2 Setup for XRR, XRD and GIXRD experiments at the beamlines W1 and P08

The synchrotron radiation for the X-ray diffraction beamline W1 at the DORIS III synchrotron is generated by a wiggler of 16 periods (length 2m). The continuous spectrum of the wiggler is filtered by a water cooled Si(111) double crystal monochromator (DCM). The first Si crystals of the DCM is aligned to fulfill the first order Bragg condition for the desired energy, while the second crystal is arranged so that it is hit by the diffracted beam of the first crystal and fulfills the same Bragg condition. As a result, only photons having the desired energy can pass the DCM. All X-ray scattering measurements at the beamline W1 were performed at photon energies of 10.5 keV corresponding to a wavelength of 0.118 nm.
The beamline P08 at the third generation synchrotron PETRA III is equipped with an undulator with 67 periods. Thus, it provides a significant higher intensity and resolution of the synchrotron radiation than the wiggler beamline W1 [85]. Since the beamline P08 and the adjacent beamline P09 are located in the same straight section of the synchrotron a combination of DCM and large-offset monochromator (LOM) is needed to separate the beams of both beamlines. The DCM consists of two liquid nitrogen cooled Si(111) crystals which have a fixed offset of 22.5 mm. The LOM is basically also a DCM but with a significantly higher vertical offset of 1250 mm, which enables the separation of the beamlines P08 and P09 and the suppression of the higher harmonics. The synchrotron beam is focused and collimated by compound refractive beryllium lenses CRLs.
At the W1 beamline the endstation is equipped with a six-circle z-axis heavy load diffractometer, while at the P08 beamline endstation a 4S+2D type diffractometer [91] is installed. Both diffractometers are appropriated to perform the modes for XRD, XRR, and GIXRD measurements. The different modes are examplarily explained in the following for the W1 diffractometer shown in Fig. 4.11. The whole diffractometer can be rotated with respect to the incident beam by the angle α. The sample is mounted at the pivot point of the diffractometer and the sample surface can be aligned by the sample goniometer. The sample is rotated by ω and the position of the detector is defined by the angles γ and δ. The XRD measurements of the specular diffration rod are performed in the horizontal mode. In this mode, the sample is mounted horizontally on the sample stage so that the surface normal defined by the crystal planes is parallel to the incidence plane of the X-rays. The diffractometer rotation α and the detector rotation γ are kept at zero. The incidence angle of the X-rays is defined by the sample rotation ω and the diffraction angle is the detector angle δ. The incidence angle ω has to be rotated by the value θ and the diffraction angle has to be at the value 2θ to fulfill the scattering conditions.
For the GIXRD measurements the vertical mode is used. In this mode, the sample is vertically mounted so that the surface normal of the crystal planes is perpendicular to the incidence plane of X-rays. The incidence angle of the X-rays is fixed and given by the diffractometer rotation α. With the surface normal as rotation axis the sample can be rotated by 360° using the angle ω. In combination with the sample rotation the detector angles γ and δ can be used

to obtain in-plane Bragg peaks as well as higher order diffraction rods.
At both beamlines W1 and P08 a Mythen [92] array detector was used for the measurements presented in this thesis. The Mythen detector has a higher dynamic range than a point detector and enables to create reciprocal space maps within a much smaller time compared to a point detector. Since the photon flux of $\approx 10^{11}$ cps (counts per second) of the primary beam is to high for the Mythen detector, a primary beam monitor and a beam attenuator are installed to control the beam intensity, which shouldn't be higher than $\approx 10^6$ cts to prevent damage from the detector. The background scattering is suppressed by an additional slit system in front of the detector tube.

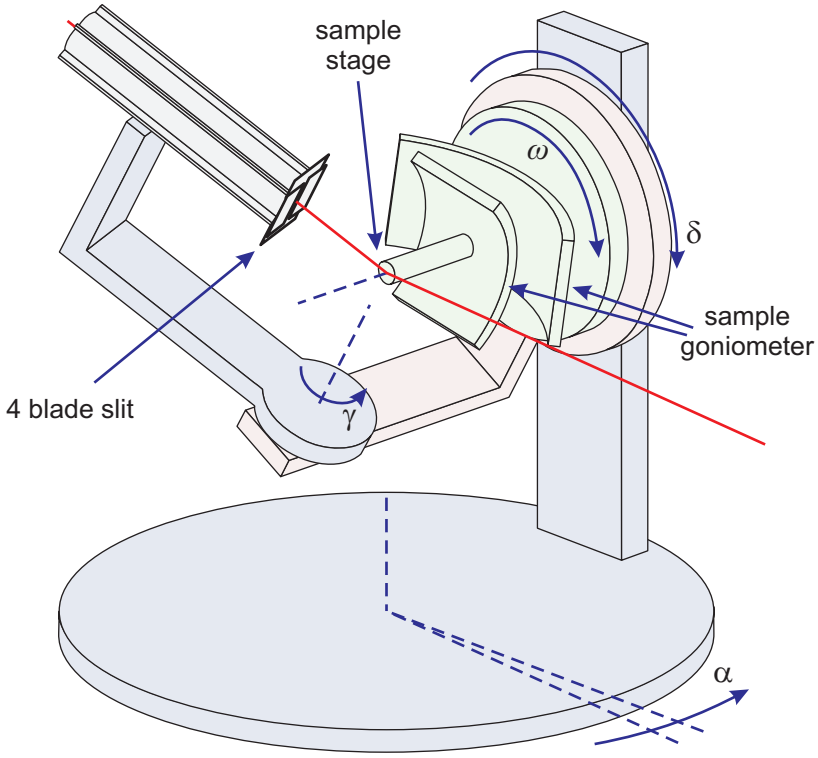

Fig. 4.11: Sketch of the z-axis diffractometer at W1. The whole diffractometer can be rotated by the angle α with respect to the incoming beam. The detector can be positioned by the rotations δ and γ, while the sample is rotated by the angle ω. The sample surface is aligned with the sample goniometer. In order to reduce the background scattering during the measurement a 4 blade slit system in front of the detector is used. Image taken from Ref. [37].

Original publication: Material Research Express **2**, 016101 (2015).
available at http://dx.doi.org/10.1088/2053-1591/2/1/016101

Magnetic anisotropy related to strain and stoichiometry of ultrathin iron oxide films on MgO(001)

T. Schemme, N. Pathé, G. Niu, F. Bertram, T. Kuschel, K. Kuepper, and J. Wollschläger

Abstract

Iron oxide films with different thicknesses (7.6 nm - 30 nm) were grown on clean MgO(001) substrates using reactive molecular beam epitaxy at 250 °C depositing Fe in a 5×10^{-5} mbar oxygen atmosphere. X-ray photoelectron spectra and low energy electron diffraction experiments indicate the stoichiometry and the surface structure of magnetite (Fe_3O_4). Film thicknesses and the lattice constants were analyzed *ex situ* by X-ray reflectometry and X-ray diffraction, respectively. These experiments reveal the single crystalline and epitactic state of the iron oxide films. However, the obtained vertical layer distances are too small to be strained magnetite and would rather suit to maghemite. Raman spectroscopy carried out to analyze the present iron oxide phase demonstrate that the films are partially oxidized to maghemite in air. This effect is most obvious for the thinnest magnetite film. Further magneto-optic Kerr measurements were performed to investigate the magnetic properties. While the thinnest film shows a magnetic isotropic behavior, the thicker films exhibit a fourfold magnetic in-plane anisotropy. The magnetic easy axes are in the Fe_3O_4 [110] direction. We propose that the magnetocrystalline anisotropy is too weak for very thin iron oxide films to form fourfold anisotropy related to the cubic crystal structure.

Original publication: Thin Solid Films **589**, 526 (2015).
available at http://dx.doi.org/10.1016/j.tsf.2015.06.018

Structure and morphology of epitaxially grown Fe_3O_4/NiO bilayers on MgO(001)

T. Schemme, O. Kuschel, F. Bertram, K. Kuepper, and J. Wollschläger

Abstract

Crystalline Fe_3O_4/NiO bilayers were grown on MgO(001) substrates using reactive molecular beam epitaxy to investigate their structural properties and their morphology. The film thickness either of the Fe_3O_4 film or of the NiO film has been varied to shed light on the relaxation of the bilayer system. The surface properties as studied by X-ray photoelectron spectroscopy and low energy electron diffraction show clear evidence of stoichiometric well-ordered film surfaces. Based on the kinematic approach X-ray diffraction experiments were completely analyzed. As a result the NiO films grow pseudomorphic in the investigated thickness range (up to 34 nm) while the Fe_3O_4 films relax continuously up to the thickness of 50 nm. Although all diffraction data show well developed Laue fringes pointing to oxide films of very homogeneous thickness, the Fe_3O_4/NiO interface roughens continuously up to 1 nm root-mean-square roughness with increasing NiO film thickness while the Fe_3O_4 surface is very smooth independent on the Fe_3O_4 film thickness. Finally, the Fe_3O_4/NiO interface spacing is similar to the interlayer spacing of the oxide films while the NiO/MgO interface is expanded.

Original publication: Journal of Applied Physics **118**, 113904 (2015).
available at http://dx.doi.org/10.1063/1.4930998

Modifying magnetic properties of ultra-thin magnetite films by growth on Fe pre-covered MgO(001)

T. Schemme, A. Krampf, F. Bertram, T. Kuschel, K. Kuepper, and J. Wollschläger

Abstract

Iron oxide films were reactively grown on iron buffer films which were deposited before on MgO(001) substrates to analyze the influence of the initial iron buffer layers on the magnetic properties of the magnetite films. X-ray photoelectron spectroscopy and low energy electron diffraction showed that magnetite films of high crystalline quality in the surface near region were formed by this two-step deposition procedure. The underlying iron film, however, was completely oxidized as proved by X-ray reflectometry and diffraction. The structural bulk quality of the iron oxide film is poor compared to magnetite films directly grown on MgO(001). Although the iron film was completely oxidized we found drastically modified magnetic properties for these films using the magnetooptic Kerr effect. The magnetite films had strongly increased coercive fields and their magnetic in-plane anisotropy is in-plane rotated by 45° compared to magnetite films formed directly by one step reactive growth on MgO(001).

8 Complex fourfold magnetocrystalline anisotropy of Fe_3O_4/Fe bilayers on MgO(001)

8.1 Abstract

In order to investigate the structural and magnetic properties of differently oxidized Fe thin films, three Fe layers have been grown on MgO(001). The films have been either left as grown, partially or completely oxidized. The stoichiometric, structural and magnetic properties of these films have been analyzed and compared. X-ray photoelectron spectroscopy and low energy electron diffraction indicate that the surface of the oxidized iron film has been transformed to magnetite. X-ray reflectometry measurements prove that, in case of the partially oxidized iron film, a Fe_3O_4/Fe bilayer was formed while there is no residual iron underneath the completely oxidized iron film. The prepared Fe_3O_4/Fe bilayer has a good crystalline quality as shown by transmission electron microscopy. However, grazing incidence X-ray diffraction and transmission electron microscopy have also demonstrated that the magnetite and the iron film of the bilayer have no homogeneous thickness due to the wavy Fe_3O_4/Fe interface. Magnetooptic Kerr effect and ferromagnetic resonance experiments reveal that the effective magnetic anisotropy of the bilayer is strongly influenced by a magnetic coupling between the Fe_3O_4 and Fe film. The magnetization curves of the bilayer have a higher coercive field than single iron films and a higher remanence than single magnetite films. The angular dependence of the coercive field of the bilayer, which is fourfold in the case of single magnetite or iron films due to the cubic crystalline magnetic anisotropy, exhibits a fourfold symmetry with additional features resulting in a complex fourfold magnetic anisotropy. FMR measurements provide all relevant magnetic parameters, such as anisotropies, as well as the coupling constant J_1. The angular dependence of the resonance field exhibits also a complex fourfold magnetic anisotropy. We found an appropriate model to calculate the resonance field of the magnetite and iron films using fourth and eighth order energy contributions of the crystal field anisotropy.

8.2 Introduction

Improving the magnetic properties of thin ferromagnetic films is of huge interest for spintronic devices including magnetic tunnel junctions (MTJs) [93]. MTJs consist of two ferromagnetic films which are separated by an insulating non-magnetic film, the tunnel barrier. Among others it is important to control the alignment of the magnetizations in the ferromagnetic films, since the tunnel probability through the tunnel barrier depends strongly on the magnetic configuration. While there is a high tunnel current for a positive tunnel magnetoresistance (TMR) [7] if the magnetizations are parallel oriented, there is a low tunnel current for antiparallel alignment. For negative TMR it is vice versa [94]. Therefore, a high coercive field is advantageous to stabilize the magnetization alignment, which depends on the crystalline structure and the film thickness [26]. A specific way to influence the coercive field of one of the ferromagnetic films is via a coupling to another ferromagnetic or antiferromagnetic film such as iron (Fe) [95] or nickel oxide (NiO) [49]. A suitable electrode material for MTJs is the ferrimagnetic magnetite (Fe_3O_4) due its high spin polarization at the Fermi level [10] and the resulting half-metallic character [9]. Moreover, magnetite has a Curie temperature [96] (587° C) considerably higher than room temperature and a saturation moment of about $4\mu_B$ [97]. An approved substrate to grow Fe_3O_4 with high crystalline quality by different deposition techniques is MgO(001) [12–14, 24–26], since the lattice mismatch of the inverse spinel structure of magnetite ($a_{Fe_3O_4}$=0.8396 nm) is only 0.3 % concerning the doubled MgO lattice constant

(a_{MgO}=0.4212 nm, rock salt structure).
In a recently published study regarding the growth of Fe_3O_4 on previously deposited iron we have shown, that the magnetic and structural properties of the magnetite film have drastically changed [98]. The magnetite films have no homogenous thickness and the magnetic fourfold anisotropy is rotated by 45°.
In this study, we investigate and compare the stoichiometric, structural, and magnetic properties of either a non-oxidized, a partially or a completely oxidized iron film on MgO(001). For the partially oxidized iron film we found a complex fourfold magnetic anisotropy.

8.3 Experimental setup and sample preparation

The samples were prepared in an ultra high vacuum multi chamber system with a preparation chamber (base pressure of 10^{-8} mbar) and an analysis chamber (base pressure of 10^{-10} mbar). The preparation chamber was equipped with an electron beam evaporator for iron, an oxygen source and a heatable manipulator. In the analysis chamber the film surface can be characterized by low energy electron diffraction (LEED) and X-ray photoelectron spectroscopy (XPS). The X-ray source of the XPS system is an Al K_α anode (1486.7 eV). In order to deposit iron films on clean substrates, the MgO substrates were annealed at 400°C in 10^{-4} mbar oxygen atmosphere for one hour. Three type of Fe films films were epitaxially grown at 250°C substrate temperature. Thereafter, one type was completely and another partially oxidized at 250°C substrate temperature and 10^{-6} mbar oxygen atmosphere. The initial iron film thickness of the partially oxidized iron film was considerably thicker to maintain an iron film after the oxidation since we could not control the film thickness during the experiment. After each preparation step the stoichiometry and the surface structure were checked by XPS and LEED, respectively.
X-ray reflectivity (XRR) and grazing incidence X-ray diffraction (GIXRD) measurements (incident angle 0.5°) were carried out at the beamline P08 of HASYLAB (DESY, Hamburg) at an energy of 15 keV to determine the film thickness, interface properties and the structure of the films. Moreover, one partially oxidized Fe film was inspected with cross-section transmission electron microscopy (TEM, FEI Titan 80-300) and energy filtered transmission electron microscopy (EFTEM).
The magnetization reversal process of the films were analyzed by magnetooptical Kerr effect (MOKE). The used MOKE setup is the same as described by Kuschel et al. [60, 99]. The MOKE measurements were performed in the longitudinal setup geometry using a HeNe laser (λ = 632.8 nm) at an incidence angle of 45°. A photoelastic modulator with a modulation frequency of f= 42 kHz was used to modulate the polarization of the reflected beam. After the modulated polarization signal has been converted into an intensity signal by an analyzer (polarizer at 45°) the intensity was detected by a photo diode. The measured intensity of the $2f$-signal (using the lock-in technique) is proportional to the Kerr rotation angle within the small angle approximation. While the magnetization curve for M_x is measured with an external magnetic in-plane field parallel to the plane of incidence of light, M_y is determined by a 90° rotation of both sample and external magnetic field [60, 100]. In addition, a vibrating sample magnetometer (VSM) was used to determine the saturation magnetization. The VSM device is a Quantum Design Squid VSM. The anisotropy constants were obtained by ferromagnetic resonance (FMR) measurements. The FMR experiments were carried out using a

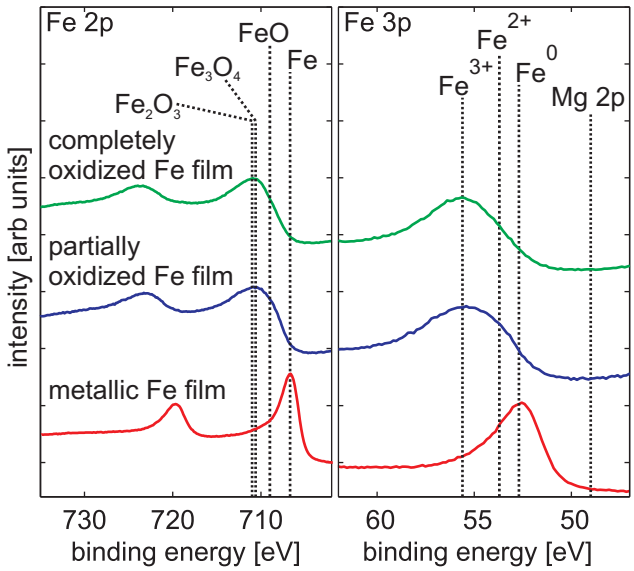

Fig. 8.1: XPS measurements of the Fe 2p and Fe 3p region for a metallic iron film, a partially oxidized iron film , and a completely oxidized iron film grown on MgO.

broadband vector network analyzer ferromagnetic resonance (VNA-FMR) setup.

8.4 Results and discussion

8.4.1 Film stoichiometry and structure

The measured Fe 2p and Fe 3p spectra are shown in Fig. 8.1. The peak positions of the Fe $2p_{3/2}$ and Fe $2p_{1/2}$ peaks of the initially grown metallic iron film are located at binding energies of 706.7 eV and 719.7 eV, respectively. The binding energy of the Fe 3p peak of the iron film is at 52.7 eV. These peak positions are typical for metallic iron [101, 102].
After oxidation of the iron films at 250°C in 10^{-6} mbar oxygen, the Fe 2p peaks and the Fe 3p peak of the iron films are at higher binding energies proving the higher oxidation state of the iron atoms. In addition, the initially sharp Fe 2p and Fe 3p peaks of the metallic iron are broader since they consist of the superposed peaks of the Fe^{2+} and Fe^{3+} ions of the formed iron oxide. The Fe $2p_{3/2}$ and Fe $2p_{1/2}$ peaks are now at 710.6 eV or 723.6 eV and the Fe 3p peak is at 55.6 eV, which is consistent with already reported binding energies of magnetite [28, 78]. The shape of the Fe 2p peak and the absence of distinct charge transfer satellites point to the formation of magnetite at the surface after oxidation [103, 104]. The missing Mg 2p peak at about 49 eV proves that there is no Mg interdiffusion in the surface near region of the iron oxide film. Since the shape and the position of the Fe 3p and the Fe 2p spectra of a completely oxidized iron film are almost equal to a partially oxidized iron film we conclude that both type of films have Fe_3O_4 stoichiometry. both type of films have no trace of metallic iron at the surface as can be seen from the missing peak at 706.7 eV.

The distinct quadratic (1×1) diffraction pattern of an initially cleaned MgO(001) surface which originates from the surface unit cell of the rock salt structure is depicted in Fig. 8.2(a). The diffraction pattern of the iron films exhibit not only an ordinary (1×1) surface structure

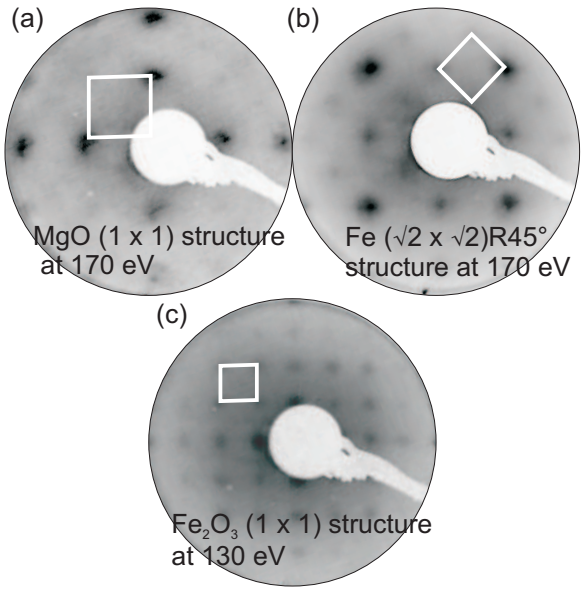

Fig. 8.2: LEED pattern of (a) cleaned MgO(001) substrate surface, (b) a previously grown iron film, and (c) an oxidized iron film. The large white square indicates the (1×1) structure of the MgO(001) surface, while the medium white squares indicate the $(\sqrt{2} \times \sqrt{2})\,\mathrm{R}\,45°$ superstructure of the Fe(001) surface, respectively. The small white square signals the (1×1) of the iron oxide surface.

(cf. Fig. 8.2(b)) but also a weak $(\sqrt{2} \times \sqrt{2})$R45° reconstruction. The (1×1) structure of iron is basically the same as the (1×1) structure of MgO since the surface unit cell of the body centered cubic iron unit cell adapts the surface unit cell of MgO (lattice mismatch -3.7 %). The $(\sqrt{2} \times \sqrt{2})$R45° iron reconstruction is an indicative of a step-terrace-based thin film that is pure and atomically flat [105, 106]. Thus, the iron surface has a good crystalline quality. The LEED measurement of the oxidized iron films are shown in Fig. 8.2(c) and reveals that the well ordered iron surface structure transforms into a Fe_3O_4(001)-(1×1) surface structure after oxidation since the reciprocal surface unit cell has half the size of both MgO(001) and Fe(001) unit cell.. The alignment follows Fe_3O_4(001)[100]‖Fe(001)[110]‖MgO(001)[100]. The missing $(\sqrt{2} \times \sqrt{2})$R45° superstructure could indicate that the surface is not well-ordered or the iron films are over oxidized and maghemite is formed at the surface. However, the XPS results contradict the formation of maghemite since there is no excess of Fe^{3+} ions at the film surface as can be seen from the missing XPS charge transfer satellites.

Furthermore, *ex situ* XRR measurements were carried out to determine the thickness and the roughness of the films after preparation. The analysis of the periodicity of the Kiessig fringes of the reflected intensities in Fig. 8.3 reveals the film thickness and the damping of the Kiessig fringes indicate the roughness of the films. The Kiessig fringes of a metallic iron film point to a film thickness of 14.0 nm. However, there is a beating which occurs for scattering vectors between q=0.17 $\mathrm{Å}^{-1}$ and q=0.21 $\mathrm{Å}^{-1}$ due to a thin (1.7 nm) iron oxide film on top of the iron film due to exposure to ambient conditions. A completely oxidized iron film exhibits only one kind of Kiessig fringes which belongs to a film thickness of 12.2 nm, so that the presence of a residual iron film can be ruled out. The reflected signal of a partially oxidized iron film exhibits a complex pattern of Kiessig fringes with two different oscillation

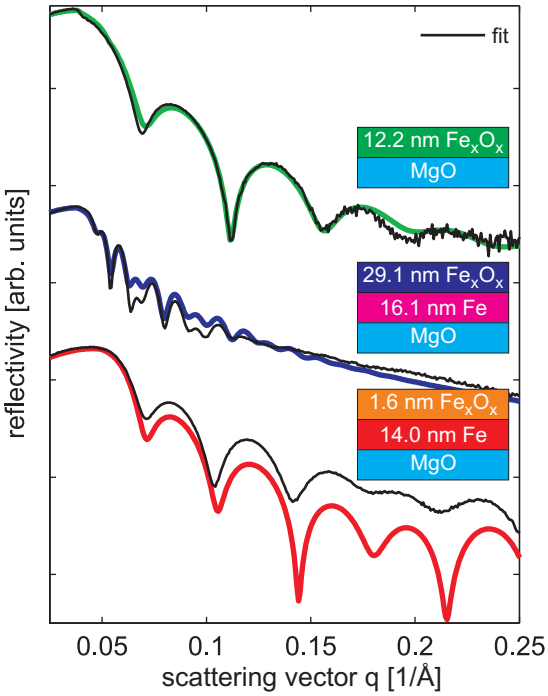

Fig. 8.3: XRR measurements of a metallic iron film (red), a partially oxidized iron film (blue), and a completely oxidized iron film (green) grown on MgO(001).

lengths proving the existence of two different films. The film thickness of the residual Fe film is 16.1 nm, while the thickness of the Fe_3O_4 film is 29.1 nm. Thus, combining the XPS, LEED and XRR results so far the partially oxidized iron film can be considered as a Fe_3O_4/Fe bilayer and the completely oxidized iron film is a single magnetite film. The surface (0.1 nm) and Fe/MgO interface roughness (0.1 nm) of the metallic iron film is low compared to the interface roughnesses of the completely oxidized iron film (0.1 nm Fe_3O_4/MgO, 1.2 nm Fe_3O_4 surface) and the partially oxidized iron film (2.0 nm Fe/MgO, 1.9 nm Fe_3O_4/Fe, 0.1 nm Fe_3O_4/air), as concluded from the damping of the Kiessig fringes with increasing scattering vector. Thus, we assume that the surface of the formed magnetite films is not well ordered.

Ex situ GIXRD measurements were performed to analyze the crystal structure of the formed iron oxide and the iron films. For this reason, we performed GIXRD scans with the scattering vector $q_\perp$ perpendicular to the surface. The GIXRD scans along the MgO $(11L)$ rod for all films studied here are shown in Fig. 8.4. The vertical direction is indexed with respect to the atomic layer distance c, which conforms to the size of the bulk unit cell of MgO. Here, $L = q_\perp\, c\,/\,2\,\pi$ denotes the scaled vertical scattering vector. All scans exhibit distinct MgO(111) rock salt reflections of the substrate. In addition, the scan of the metallic and the scan of the partially oxidized iron film show broad Fe(101) Bragg peaks pointing to crystalline iron films. The Fe_3O_4(222) Bragg peaks of the bilayer and of the completely oxidized iron film appear weakly in the shoulder of the MgO(111) Bragg peak if at all. The missing Fe(101) Bragg peak in the scan of the completely oxidized iron film proves that there is no residual crystalline iron left after the oxidation process. The diffraction signal of the bilayer displays also the (224) Bragg reflection of magnetite which can also be observed for the completely oxidized iron film. The Fe_3O_4(224) Bragg reflection originates exclusively from Fe ions on the

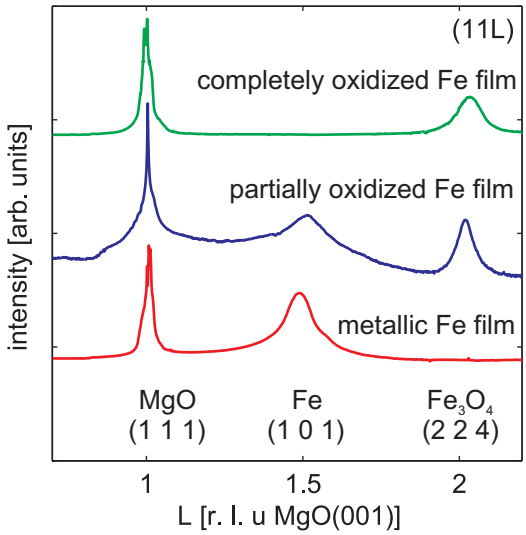

Fig. 8.4: XRD scans along the (11) rod of MgO(001) in L-direction for a metallic iron film, a partially oxidized iron film (bilayer), and a completely oxidized iron film grown on MgO.

tetrahedral sites of the inverse spinel structure [14]. Thus, this indicates an at least partially ordered tetrahedral sublattice of a crystalline magnetite film since the (224) Bragg reflection of magnetite can clearly be seen. The overall missing Laue fringes point out that the formed magnetite films and the residual iron film do not have homogeneous film thickness. This observation confirms the high roughness of the films as determined by XRR.

The bilayer has also been examined by cross-section TEM measurements and EFTEM to analyze the bilayer structure and element distribution in more detail (cf. Fig. 8.5). The pseudo-color image of the cross section shows the distribution of oxygen (red) and iron (blue) in the bilayer (cf. Fig. 8.5 (a)). The cross section of the bilayer clearly consists of three sections. The first section at the bottom is the oxygen rich MgO substrate. Above the substrate follows the oxygen poor iron film. On top of the iron film is the magnetite film which contains of iron and oxygen ions.

In accordance with our GIXRD studies, the film characterization by TEM reveals that both the iron film and the magnetite film of the bilayer have a crystalline structure with sharp transitions between their atomic structures (cf. inserts Fig. 8.5 (b)) as can be easily seen at the atomic resolution TEM images. Though the interface between the magnetite film and the iron film is quite sharp it is also wavy so that both films have no homogeneous film thickness. This can be attributed to a non-homogeneous oxidation process. The interface between the iron film and the substrate is smooth despite the oxidation of the iron film. Thus, the TEM experiments confirm the XRR and GIXRD results which point to an Fe_3O_4/Fe bilayer with a crystalline iron film and a crystalline magnetite film with large interface roughness.

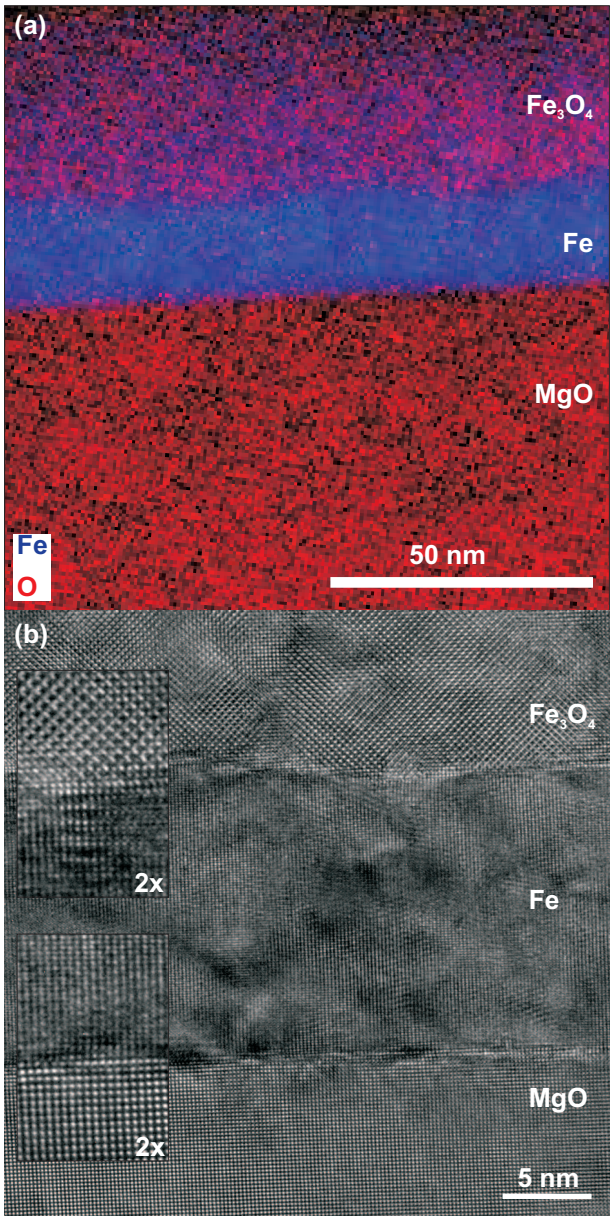

Fig. 8.5: (a) EFTEM and (b) TEM image of a cross section of the Fe_3O_4/Fe bilayer.

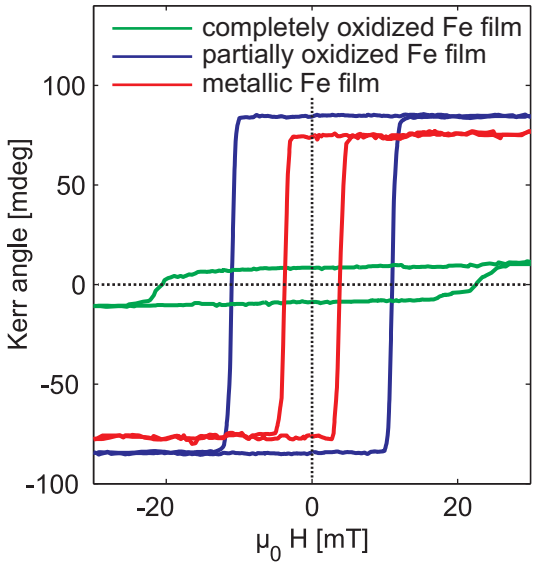

Fig. 8.6: Magnetization curves in magnetic easy direction for a single Fe film (blue), a single Fe_3O_4 film (black) and an Fe_3O_4/Fe bilayer (red).

8.5 Magnetooptic Kerr effect

Ex situ MOKE measurements were performed in longitudinal geometry to determine the dependence of the magnetization on the direction of the external magnetic field for all samples. Figure 8.6 presents the magnetization curves of the Fe_3O_4/Fe bilayer (partially oxidized iron film), the metallic iron film and the completely oxidized iron film. The external magnetic field was applied in [110] direction of the MgO substrate, which coincides with the magnetite [110] direction as well as the Fe[100] direction. These axes are typical magnetic easy axes of magnetite [26, 107] and iron films [60], respectively. While the magnetization curve of the completely oxidized iron film exhibits a small Kerr rotation for saturation and a high coercive field, the magnetization curve of the metallic iron film has a high saturation Kerr rotation and a lower coercive field. The measured Kerr rotation of the Fe_3O_4/Fe bilayer is slightly larger than for the metallic iron film while the coercive field is smaller than the coercive field of the completely oxidized iron film.
The small Kerr angle of the completely oxidized iron film in magnetic saturation has also been observed earlier for single magnetite films [26]. The high Kerr rotation for the bilayer indicates that the magnetization curve of the bilayer is dominated by its iron film. The coercive field of the bilayer and the completely oxidized iron film is higher than reported for magnetite in literature [26, 108]. This can be attributed to the inhomogeneous film thickness of the bilayer and the completely oxidized iron film as determined by GIXRD and TEM. Thus, the magnetization curve of the bilayer combines the high Kerr rotation of its iron film with a higher coercive field.

Magnetization curves applying the external magnetic field in different azimuthal sample directions α were measured in one degree steps to analyze the magnetic anisotropy due to the crystalline structure of all films in more detail. The angular dependence of the magnetic remanence is depicted in Fig. 8.7. A distinct fourfold magnetic anisotropy can be seen for

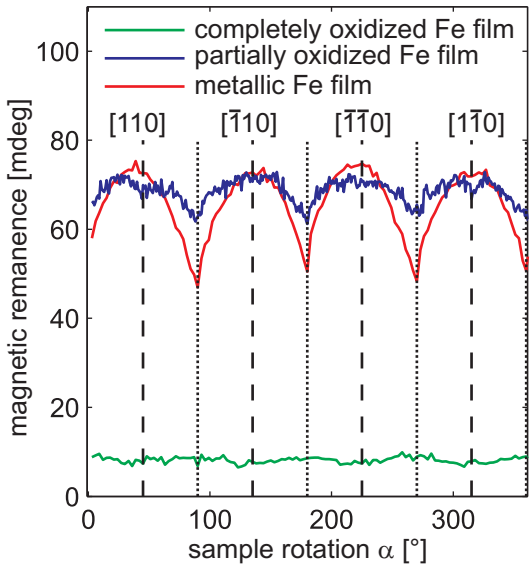

Fig. 8.7: Angular dependence of the Kerr angle in magnetic remanence. Maxima indicate magnetic easy directions, minima point to magnetic hard directions.

the metallic iron film and the bilayer. As pointed out before, both the metallic iron film and the bilayer have the magnetic easy axes in MgO⟨110⟩ directions, which are well known for iron and magnetite films (see above). Although the magnetic remanence is almost equal for the bilayer and the metallic iron film, the maxima in the angular dependence of the magnetic remanence are more pronounced for the single iron film. The completely oxidized iron film, however, shows an almost isotropic behavior which can be attributed to the overall small Kerr angle of this film.

The magnetic hard and easy axes of the completely oxidized iron film can be easier observed in the angular dependence of the coercive field in Fig. 8.8. The completely oxidized iron film has the highest coercive fields and exhibits a distinct fourfold anisotropy with clear maxima in MgO⟨100⟩ directions, due to the comparably high coercive field. In addition, there are sharp maxima in MgO⟨110⟩ directions. These sharp maxima (spikes) at exact magnetic hard directions point to magnetic multidomain states in magnetic remanence and incoherent magnetization rotation (some magnetic domains rotate clockwise, some counterclockwise) between magnetic saturation and magnetic remanence [109]. The magnetic moments are frustrated when chosing the next magnetic easy axis during the reversal process [110].

As reported in literature [107], the magnetic easy axes of magnetite thin films are commonly in MgO⟨110⟩ directions. This rotation by 45° observed here has been reported earlier [98] and could be related to the poor structural quality of the completely oxidized iron film. The metallic iron film displays the same fourfold magnetic anisotropy with maxima for MgO⟨110⟩ directions as seen in magnetic remanence (cf. Fig. 8.7). However, differences between magnetic easy and hard axes are much less pronounced due to the small coercive field of the metallic iron film. Moreover, no spikes can be seen at magnetic hard directions indicating a coherent magnetization rotation.

The angular dependence of the coercive field of the Fe_3O_4/Fe bilayer (partially oxidized iron film) is rather complex in contrast to the magnetic remanence. It exhibits a fourfold magnetic anisotropy with overall eight maxima and additional spikes for MgO⟨100⟩ directions. Here

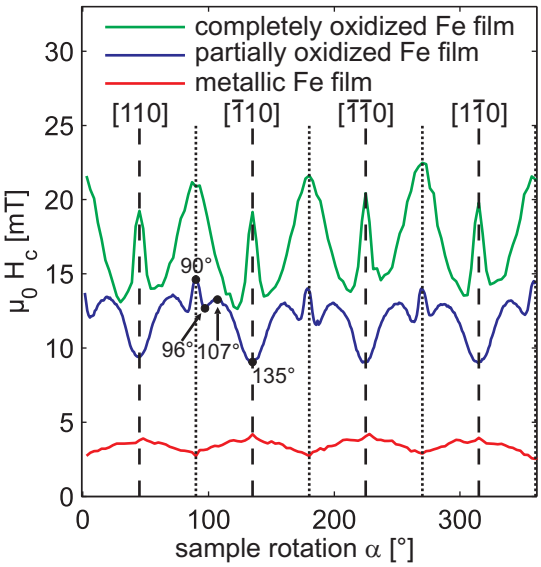

Fig. 8.8: Coercive field plots dependent on the azimuthal sample angle α of a single Fe film (red), a single Fe_3O_4 film (green) and an Fe_3O_4/Fe bilayer (blue).

the spikes again indicate magnetic hard directions with multi domain states. These directions agree with the hard directions concluded from the magnetic remanence of the bilayer. However, the coercive field plot shows the deepest minima in MgO⟨110⟩ directions which contradicts the remanence plot where the maxima, which define the magnetic easy axes, are also in MgO ⟨110⟩. The eight maxima are roughly ± 17° off magnetic hard directions.

Since the determination of the magnetic easy axes of the partially oxidized iron film is not obvious considering the contradicting results of the angular dependence of the coercive field and the magnetic remanence we carried out vectorial magnetometry based on MOKE as described earlier to investigate the reversal process of the magnetization vector in the bilayer. Therefore, the magnitude $M = \sqrt{M_x^2 + M_y^2}$ and the azimuthal rotation angle $\gamma = \arctan(M_x/M_y)$ of the in-plane magnetization vector are calculated with respect to the positive external magnetic field direction. We neglect the out-of-plane component M_z due to the magnetic shape anisotropy. The magnetic field dependence of M_x and M_y were recorded for four special angular directions alpha chosen from the angular dependence of the coercive field of the bilayer. These are $\alpha = 135$ ° (global minima, magnetic easy axis), $\alpha = 90$ ° (spike, magnetic hard direction), $\alpha = 96°$ (minima next to the spike, 6° off magnetic hard axis), and $\alpha = 107°$ (one of the eight maxima). The obtained magnetization hysteresis curves and the calculated magnitude of the magnetization plotted versus the applied external magnetic field are depicted in Fig. 8.9.

All curves for M_x (blue line) have the same Kerr rotation for the magnetic saturation of about 75 mdeg and a similar shape of the hysteresis loop. They vary slightly in the magnitude of the magnetic remanence and in the applied coercive field. The coercive field at $\alpha = 135$ ° is distinctly smaller than the coercive fields of the other chosen directions eye.
The shape of the M_y (red) curves varies distinctly for the different directions. At $\alpha = 135°$

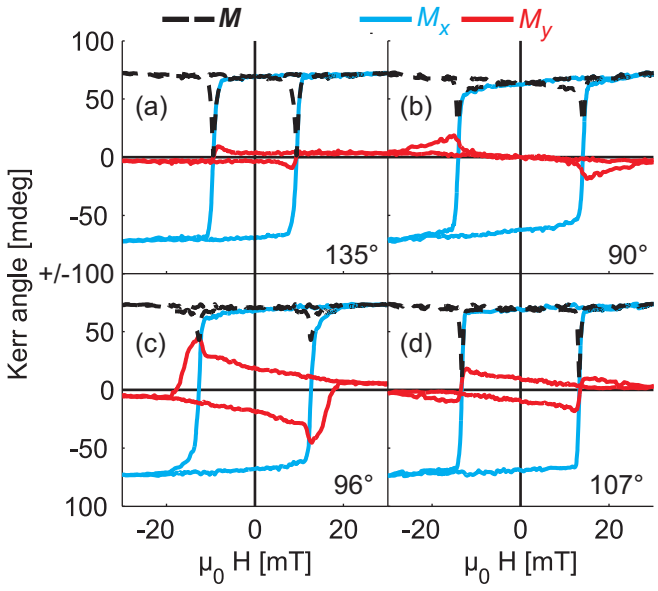

Fig. 8.9: Magnetization curves of the Fe_3O_4/Fe bilayer for M_x and M_y for (a) magnetic easy axis, (b) magnetic hard axis, (c) 6° off magnetic hard axis, and (d) at $\alpha = 107°$.

nearly no M_y component is detectable during the entire reversal process. This behavior is typical for a magnetic easy axis. For the other three directions a M_y component is obtained which is strongest at $\alpha = 96°$. The Kerr rotation of M_y vanishes for the magnetic saturation and is largest near the coercive field where M_x switches.
The magnitude M (black dashed line) depending on the external magnetic field is also shown for the four sample alignment angles introduced above. The magnitudes overlap with their M_x component if their M_y component is small. The saturation values of the magnitude correspond to the saturation value of the M_x component (both 75 mdeg), because in magnetic saturation the magnetization vector should be parallel to the external magnetic field. The magnitude is almost constant during the reversal process, however, sharp decreases are observed near the coercive fields of the M_x component. The decreasing of the magnitude of the magnetization is related to the transition from magnetic mono-domain state into magnetic multi-domain state with different magnetization orientations. Thus, the resulting averaged magnetization vector is smaller in this case. At $\alpha = 135\,°$ these sharp drops are deepest and weakest for $\alpha = 96\,°$. The weaker the drops the larger is the M_y component and vice versa. At $\alpha = 107\,°$ these sharp drops are almost as deep as for $\alpha = 135\,°$.
The reconstructed courses of the magnetization during the reversal processes of the magnetization are shown in Fig. 8.10 using polar plots for the four sample alignment angles α. Here, γ is the azimuthal rotation angle of the magnetization vector $\boldsymbol{M}$, which is defined as the angle between sample magnetization and positive external magnetic field direction (cf. magnetization for saturation). The rotation direction of the net magnetization during the reversal process is counterclockwise for $\alpha = 90\,°$ (magnetic hard axis). For the directions $\alpha = 96\,°$ and $\alpha = 107\,°$ the sense of the rotation is also counterclockwise except for the parts where the magnetization rotates backwards into the direction of the inverted external magnetic field. There is no certain sense of the rotation for $\alpha = 135\,°$ (magnetic easy axis), since themagnetic moments rotate both clockwise and counterclockwise. Starting in satura-

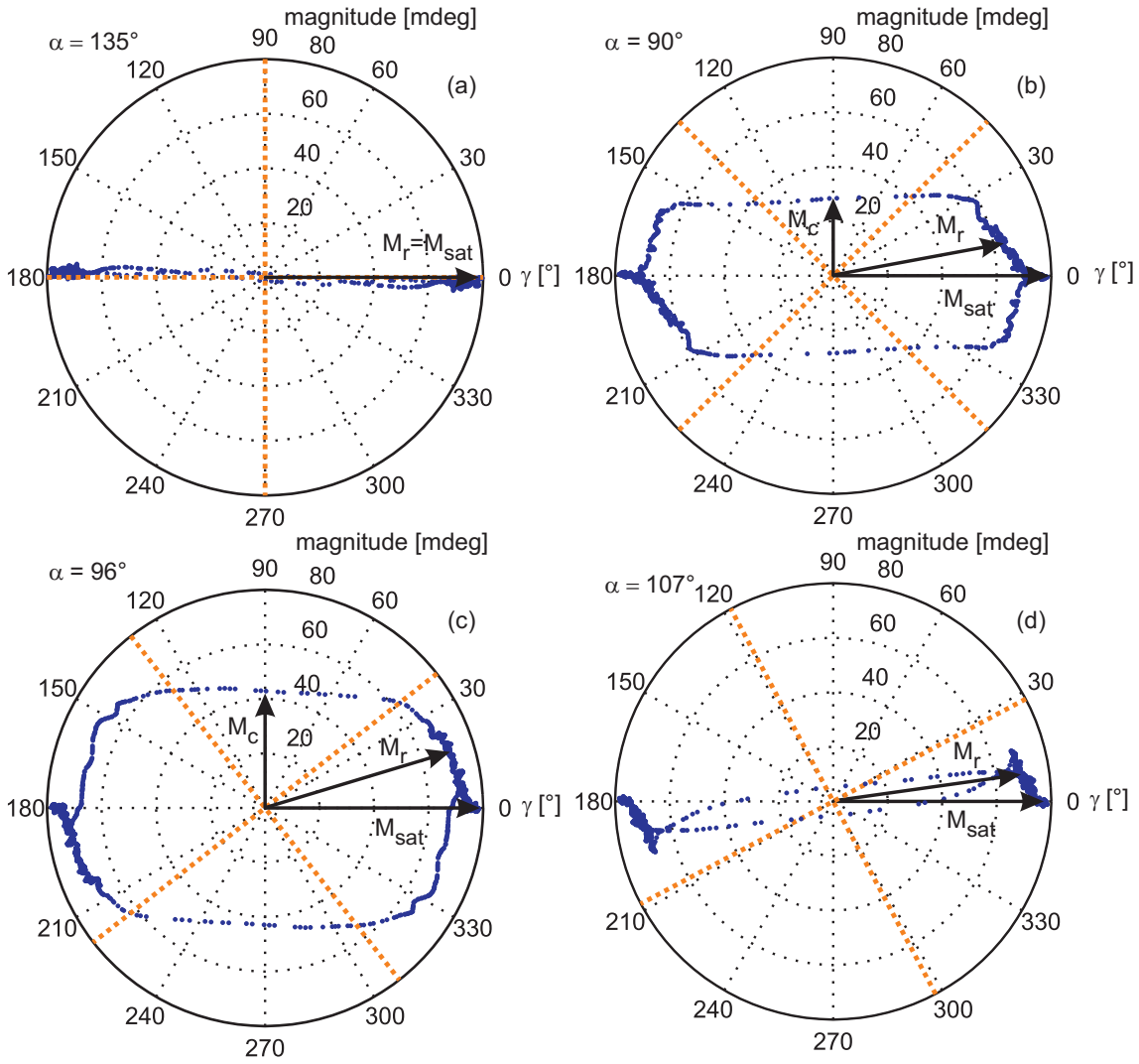

Fig. 8.10: Reversal process of the magnetization vector of the bilayer for (a) $\alpha = 135$ ° (magnetic easy axis), (b) $\alpha = 90$ ° (magnetic hard axis), (c) $\alpha = 96$ ° (6° off magnetic hard axis), and (d) $\alpha = 107°$ (between magnetic easy and hard axis). The magnetization is plotted with respect to the rotation angle γ. The magnetic field is aligned in $\gamma = 0°$ ($\gamma = 180°$) direction. The yellow dashed lines indicate the magnetic easy axes. The position of the magnetization vector in magnetic saturation M_s and in magnetic remanence M_r is marked. In addition, for $\alpha = 90$ ° and $\alpha = 96$ ° the position of the magnetization vector M_c at $M_x = 0$ ($\gamma = 90$ °) is shown.

tion, the magnetization rotates towards the closest magnetic easy axis with respect to the direction of the external magnetic field if the external magnetic field is not applied exactly in magnetic easy or magnetic hard direction. Thus, the magnetization for $\alpha = 96\,^\circ$ rotates counterclockwise because the next magnetic easy axis is at $\gamma = 309\,^\circ$ or $\gamma = 39\,^\circ$ (cf. Fig 8.10).
The reversal process of the magnetization vector can be explained using monodomain states during saturation of the magnetization vector and multi domain states if the magnitude of the magnetization vector decreases. This happens in two different situations. On the one hand, multi domain states occur, when the net magnetization switches from one magnetic easy axis to another magnetic easy axis. Here, the magnetic moments switch successively from one to the other magnetic easy axis (90° or 180° domain states). During the switch half of the moments are aligned in one magnetic easy direction, the other half in the second magnetic easy direction. Thus, the net magnetization is reduced [60]. On the other hand, multi domain states are present, when the external magnetic field is aligned parallel to a magnetic hard axis. Reducing the external magnetic field strength in magnetic saturation the moments split up in those that rotate clockwise and those that rotate counterclockwise (incoherent rotation). Therefore, the net magnetic moment is again reduced and the magnetic frustration leads to the formation of the spikes in the coercive field values.
During domain splitting phase in most cases the magnetic moments of the individual domains are parallel to magnetic easy axes. The behavior of the magnitude of the magnetization for $\alpha = 135\,^\circ$ (magnetic easy axis), $\alpha = 96\,^\circ$ (6° off magnetic hard axis), and $\alpha = 90\,^\circ$ (magnetic hard axis) has been studied earlier for a 7 nm single iron film by Kuschel et al. [60].
Comparing their obtained reversal processes to the measured reversals here reveals similarities and differences. The reversal process of the magnetic easy axis (alpha=135 °, cf. Fig 8.10(a)) is the typical two-state behavior as also seen in Ref. [60]. The magnetization stays in magnetic easy direction until the magnetic remanence. When the reversed magnetic field reaches the coercive field value, the moments switch to the opposite magnetic easy direction (180 ° domains). There is only one switch and the other perpendicular aligned magnetic easy axis is not involved in the reversal process.
If the magnetic field is aligned 6 ° off the magnetic hard axis (alpha=96 °, cf. Fig. cf. Fig 8.10(c)), a rectangular-like behavior is observed for the course of the magnetization vector in the polar plot. While in Ref. [60] two switches could be observed, here only one switch can be detected as already seen from the magnitude vs. magnetic field curves in Fig. 8.9 having just one dip at the coercive field position. So, the magnetic anisotropies and the resulting energy landscape do not allow the magnetization to switch a second time, but to rotate towards the reversed external magnetic field direction after pointing slightly to negative M_y values. The rectangular-like course points to some magnetic domains rotating in the opposite direction already from magnetic saturation on (slightly incoherent rotation), since a reversal process with coherent rotation (all magnetic moments have the same rotation sense) has a square-like course [60]. Thus, during the switch two major 90 ° domain types are present pointing into the upper two magnetic easy directions, while two minor 90 ° domains point into the lower magnetic easy directions.
The reversal process for magnetic hard direction (alpha=90 °, cf. Fig. Fig 8.10(b)) gives again the same picture as in Ref. [60]. The incoherent rotation of the magnetic moments having different rotation senses results in an already reduced magnitude of the magnetization between saturation and magnetic remanence. Since the net magnetization rotates counterclockwise, a larger amount of magnetic moments rotate counterclockwise as well, while a minor amount

rotates clockwise. Therefore, the external magnetic field is not exactly aligned in magnetic hard direction, but should be close (± 1 °). During the single switch four 90 ° domain states occur as described in detail in Ref. [60].
One type of reversal process can be observed which was not detected in Ref. [60]. This curve (for alpha=107 °, cf. Fig 8.10(d)) consists of an initial almost coherent rotation followed by a 180 ° switch comparable to the reversal process in magnetic easy axis. The main difference is, that the 180 ° switch does not start/end at γ=0 °/180 °, but takes place 10 ° off these directions. Such kind of reversal processes needs more complicated energy landscapes and, therefore, additional anisotropy contributions as now tested by FMR.

8.6 Ferromagnetic resonance

Similar to the MOKE measurements, dynamic FMR measurements can be performed to characterize the angle-dependent behavior (in-plane and out-of-plane) of the bilayer. Therefore, at first the metallic and the fully oxidized iron film were characterized by FMR yielding the respective film properties of both components. Subsequently the film parameters were reemployed for the fitting of the coupling bilayer which enables the quantification of the exchange coupling constant J_1.

Numerical model

The resonance frequencies were fitted by numerically solving the resonance condition [63, 111]:

$$\omega = \frac{\gamma}{M_\mathrm{S} \cdot \sin\vartheta_0} \cdot \left[F_{\vartheta\vartheta}F_{\varphi\varphi} - F_{\vartheta\varphi}^2\right]^{\frac{1}{2}} \quad . \tag{8.1}$$

Here, $F_i = \frac{\partial F}{\partial i}$ is the derivative of the free energy F, ϑ (φ) the polar (azimuth) angle of the magnetization and ϑ_0 the polar equilibrium angle of the magnetization. In the model, the free energy F consists of the following contributions:

$$\begin{aligned} F =& F_\mathrm{Zeeman} + F_\mathrm{shape} + F_\mathrm{crystal} \\ F =& -\mu_0 M_\mathrm{S} H \left[\sin\vartheta \sin\vartheta_H \cos(\varphi - \varphi_H) + \cos\vartheta\cos\vartheta_H\right] \\ & - \left(\tfrac{1}{2}\mu_0 M_\mathrm{S}^2 - K_{2\perp}\right) \cdot \sin^2\vartheta - K_{2\parallel} \cdot \sin^2\vartheta\cos^2(\varphi - \varphi_u) \\ & - \tfrac{1}{2}K_{4\perp}\cos^4\vartheta - \tfrac{1}{8}K_{4\parallel} \cdot \left[3 + \cos 4\varphi\right] \cdot \sin^4\vartheta \end{aligned} \tag{8.2}$$

with the polar (azimuth) magnetization angle ϑ (φ) and ϑ_H (φ_H) the polar (azimuth) field angle and $K_{2\perp}$ ($K_{2\parallel}$) and $K_{4\perp}$ ($K_{4\parallel}$) the uniaxial and fourfold out-of-plane (in-plane) anisotropy constants, respectively. In case of the partially oxidized bilayer, an additional coupling contribution to the free energy F needs to be considered. Therefore, the expression as an areal

	t	M_S	$g_\perp$	$g_\parallel$	$K_{2\perp}$	$K_{4\perp}$	$K_{4\parallel}$
unit	nm	kA/m			kJ/m^3	kJ/m^3	kJ/m^3
iron	14	1706.2	2.09	2.07	55.5	15.0	51.0
magnetite	12.2	475.1	2.00	2.00	74.9	-1.1	15.0

Tab. 8.1: Properties of the metallic and the completely oxidized iron film (magnetite). The magnetic quantities were obtained by FMR measurements. The values for M_S were obtained using VSM.

density $\hat{F}$ becomes suitable

$$\hat{F} = \hat{F}_J + \sum_{i=1}^{2} t_i \Big[-\mu_0 M_{S,i} H \cdot \big(\sin\vartheta_i \sin\vartheta_H \cos(\varphi_i - \varphi_H) + \cos\vartheta_i \cos\vartheta_H \big) + F_{crystal,i} \Big] \tag{8.3}$$

with

$$F^i_{crystal} = -\left(\tfrac{1}{2}\mu_0 M^2_{S,i} - K_{2\perp,i}\right) \cdot \sin^2\vartheta_i - K_{2\parallel,i} \cdot \sin^2\vartheta_i \cos^2(\varphi_i - \varphi_u) \tag{8.4}$$

$$- \tfrac{1}{2} K_{4\perp,i} \cos^4\vartheta_i - \tfrac{1}{8} K_{4\parallel,i} \cdot [3 + \cos 4\varphi_i] \cdot \sin^4\vartheta_i \tag{8.5}$$

and

$$\hat{F}_J = -J_1 \frac{\vec{M}_1 \cdot \vec{M}_2}{M_{S,1} M_{S,2}} = -J_1 \left(\sin\vartheta_1 \sin\vartheta_2 \cos(\varphi_1 - \varphi_2) + \cos\vartheta_1 \cos\vartheta_2\right) \tag{8.6}$$

and with the index i representing each layer, ϑ_i (φ_i) the polar (azimuth) magnetization angle and t_i the layer thickness. The direct exchange coupling was regarded by adding the coupling contribution $\hat{F}_J$ with J_1 being the coupling constant. [112]
For a quantification of the exchange-coupling in the Fe_3O_4/Fe bilayer, characterizations of the single metallic iron and the completely oxidized iron films were carried out first serving as references. By means of FMR, angle- and frequency-dependent measurements were performed and magnetic parameters, as presented in Tab. 8.1, were obtained by the fitting of the resonance positions using Eq. (8.2).

The in-plane (easy axis) and out-of-plane frequency-dependencies of both materials are depicted in Fig. 8.11. Note that the out-of-plane measurement data of the single metallic iron film does also contain the not aligned mode, which cannot be described by the calculations. The not aligned mode arises from magnetization switching into the easy axis direction since the applied magnetic field is too weak.

For a firm description of the modes in the partially oxidized bilayer sample, exchange coupling and its effects on the FMR spectra need to be considered. Equivalently to coupling oscillators in mechanics, the measured resonances can be understood as either in-phase precession (acoustical mode) or anti-phase precession (optical mode) of the spins in either film. It is noted that the coupling becomes most relevant when the modes of the single films are of similar energy. The more the energies of the single-film modes differ, the lower the impact of

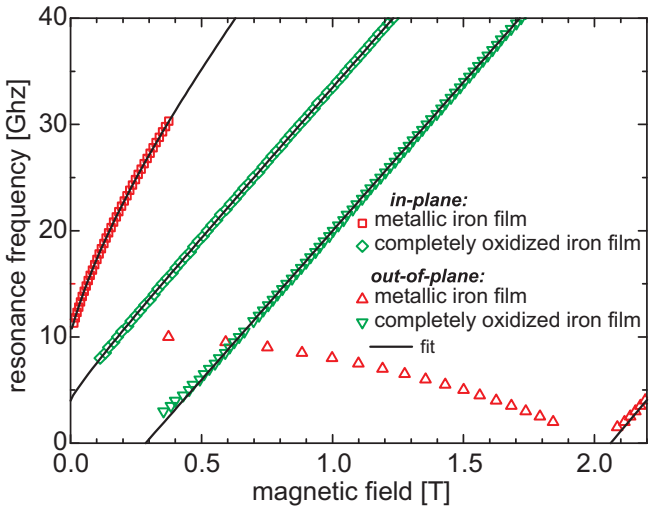

Fig. 8.11: (Color online) Frequency vs. field dependencies of both metallic iron (red symbols) and completely oxidized iron (green symbols) with fits. The corresponding magnetic parameters gained by fitting are given in Tab. 8.1.

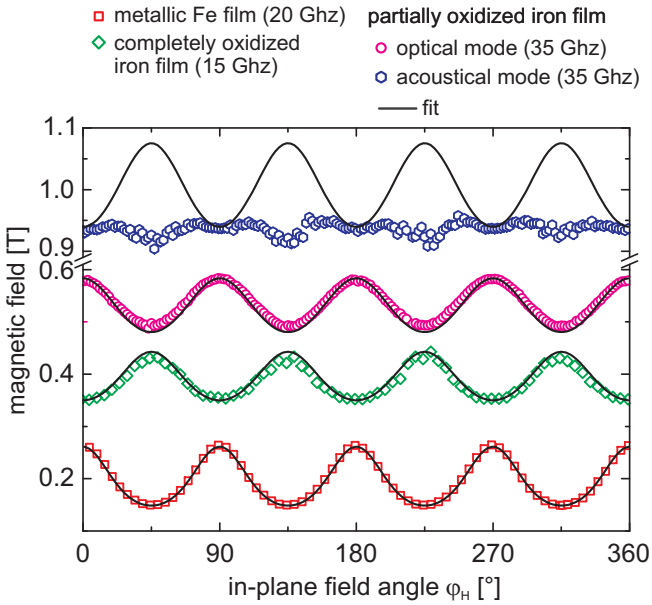

Fig. 8.12: (Color online) In-plane angular dependencies of the metallic iron film (red squares) and the completely oxidized iron film (green diamonds) as well as the optical and acoustical mode of the partially oxidized iron film with the respective fits. The optical (acoustical) mode of the coupled stack is represented by black circles (blue hexagons). The measured angular dependence of the acoustical mode reveals systematic deviations from the expected behavior with an additional easy axis coinciding with the optical modes' easy axis.

	t_{Fe}	$t_{Fe_3O_4}$	$K_{2\perp}$-Fe	$K_{2\perp}$-Fe_3O_4	$K_{4\parallel}$-Fe_3O_4	J_1
unit	nm	nm	kJ/m^3	kJ/m^3	kJ/m^3	mJ/m^2
value	16.1	29.1	30.6	54.3	23.5	0.64

Tab. 8.2: Parameters obtained by FMR measurements of the exchange coupled Fe_3O_4/Fe bilayer.

the coupling on the resonance position.

To describe the optical and acoustical mode of the exchange-coupled Fe_3O_4/Fe bilayer, all parameters from the pre-characterization (Tab. 8.1) were re-employed, except from the two-fold out-of-plane anisotropy $K_{2\perp}$ and M_S. In the bilayer, the additional interface between both films is present. This circumstance alters the surface anisotropies of the layers, which requires for an independent fitting of $K_{2\perp}$ in case of the bilayer. Moreover, systematic deviations between measurement and theory revealed an enlarged fourfold in-plane anisotropy of the Fe_3O_4 layer in the bilayer sample. Hence, fits in Fig. 8.13 were obtained by adjusting $K_{4\parallel}^{Fe_3O_4}$ (value provided in Tab. 8.2). To find the optimal values for $K_{2\perp}$, $K_{4\parallel}^{Fe_3O_4}$ and J_1, the quantities were fitted using the frequency-dependencies in in-plane and out-of-plane configuration. The resulting fits as well as the measurement data is illustrated in Fig. 8.13 and the values are provided in Tab. 8.2. Note that the not-aligned branch shows coupling effects, i.e. the splitting into optical and acoustical mode, as well.

A comparison of the angle-dependent measurement with the theory is illustrated in Fig. 8.12. The fit follows well the measurement data along the optical mode. However, the acoustical mode shows major deviations from the theoretically calculated resonance position around the hard direction ($\varphi_H = 45°, 135°, 225°, 315°$). Here, an additional pronounced easy direction is measured such that the hard directions are apparently shifted towards intermediate angles ($\varphi_H = 22.5°, 67.5°, 112.5°, 157.5°$).

This peculiar behavior is the only significant discrepancy between measurement and theory, which indicates, that further magneto-dynamic effects might play a role here. Standing spin-waves [113, 114], which are confined between the two surfaces of a thin film, might play an important role here related to this phenomenon. These spin-wave modes are also referred to as perpendicular standing spin-wave (PSSW) modes and are different from precessional modes, since they are having a defined vertical wave vector $k = n(\pi + \delta)/d$ with n=1,2,... determined by the film thickness d and the pinning parameter δ. The frequency-field dependence can be calculated by [115, 116]

$$(\omega/\gamma)^2 = (\mu_0 H_{eff} + \mu_0 M_S + Dk^2) \cdot (\mu_0 H_{eff} + Dk^2) \tag{8.7}$$

with H_{eff} being the sum of the external field and the anisotropy field and D the exchange stiffness constant. The green lines in Fig. 8.13 indicate that the PSSW mode of the magnetite layer is very close to the acoustical mode, if $\delta = 0$ and $D = 12\,\mathrm{Tnm}^2$ are selected according to the literature [117]. This circumstance makes an interaction between the acoustical coupling mode and the magnetite PSSW mode a possible candidate for the origin of the complex fourfold behavior. However, the above calculation can only be understood as an approximation, since the pinning parameter and the exchange stiffness constant are unknown for magnetite

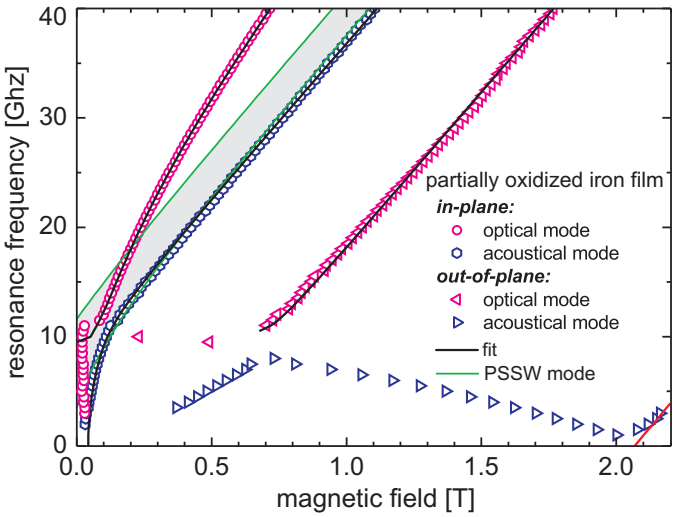

Fig. 8.13: (Color online) The frequency dependence of the exchange-coupled Fe_3O_4/Fe bilayer with fits. The optical (acoustical) mode is represented by magenta symbols (blue symbols). Parameters obtained by fitting are provided in Tab. 8.2.

samples of such preparation technique. As Aragon et al. reported, the exchange stiffness constant is very sensitive to minor stoichiometric changes in the case of magnetite [117].

8.6.1 Eighth order magnetocrystalline anisotropy

We also propose another model to calculate the resonance field of all samples using also the formula of Smit et al. [63]. Like in the approach above, we initially sum up the different contributions of the free energy to obtain the total free energy density F_{tot}. However, instead of introducing a coupling contribution with a coupling parameter, we consider beside the fourth order [47] also the eighth order of the crystal anisotropy $F_{crystal}$. Here, we assume that the the magnetization is always parallel to the applied external magnetic field ($\vartheta = 90°$). In addition, we suppose that the acoustical mode corresponds to the magnetite film and the optical mode corresponds to metallic iron film of the bilayer. The contribution of the eighth order of the crystal anisotropy can be expressed as

$$\begin{aligned} F_8 &= K_{8\parallel}\,\alpha_1^4\alpha_2^4 + K_{8\perp}\,(\alpha_1^4\alpha_3^4 + \alpha_2^4\alpha_3^4) \\ &= K_{8\parallel}\,\cos^4\vartheta\,\sin^4\vartheta + K_{8\perp}\,\sin^8\vartheta\,\cos^4\varphi\,\sin^4\varphi\ . \end{aligned} \tag{8.8}$$

Here, α_i denote the direction cosine regarding the crystal axis i and $K_{8\parallel}$ and $K_{8\perp}$ are the anisotropy constants of the eighth order. The direction cosine in polar coordinates are given by $\alpha_1 = \sin\vartheta\,\cos\varphi$, $\alpha_2 = \sin\vartheta\,\sin\varphi$, and $\alpha_3 = \cos\vartheta$. Afterwards, we set in F_{tot} in the resonance equation given by Smit and Beljers [63]. We solve this equation for $\mu_0 H$ and obtain a periodic expression to calculate the experimental measured resonance field. To simplify the calculation, we used the effective magnetization M_{eff} instead of M_S. The effective magnetization M_{eff} is defined by

$$\mu_0 M_{eff} = \mu_0 M_S + 2k_{2\perp} + 2k_{4\perp} - \frac{1}{2}k_{4\parallel} + \frac{3}{16}k_8\ ,$$

film	ω [GHz]	g	$\mu_0 M_{eff}$ A/m	$K_{4\parallel}$ kJ/m^3	$K_{8\parallel}$ kJ/m^3
optical mode of the partially oxidized iron film	35	2.07	2.19	-44.2 (43.2)	5.0
acoustical mode of the partially oxidized iron film	35	2.00	0.71	-0.2	-12.7
metallic iron film	20	2.00	2.18	-57.3 (-54.4)	30.4
completely oxidized iron film	15	2.07	0.30	14.1 (15.2)	5.6

Tab. 8.3: Parameters obtained by FMR measurements of the Fe_3O_4/Fe bilayer (partially oxidized iron film) considering the 8 th order of the magneto crystalline anisotropy. The values for $K_{4\parallel}$ with $K_{8\parallel} = 0$ during the calculations are represented in brackets.

and the relative magnetic in-plane anisotropy constants $k_{4\parallel}$ and $k_{8\parallel}$ are given by $k_{4\parallel} = K_{4\parallel}/M_S$ and $k_{8\parallel} = K_{4\parallel}/M_S$. The values for $g$were taken over from the previous calculations. Thus, $\mu_0 H$ is besides the azimuthal sample angle φ a function of the relative magnetic in-plane anisotropy constants $k_{4\parallel}$, $k_{8\parallel}$, and the effective magnetization M_{eff}. The results of this calculation are included in Fig. 8.14 as black curves and the parameters are listed in Tab. 8.3. The calculations fit closely to the measured resonance fields. Comparing the obtained anisotropy constants $K_{4\parallel}$ and $K_{8\parallel}$, for Fe_3O_4 layer (acoustical mode) we find that the $K_{4\parallel}$ of the acoustical mode is almost zero. Thus, the $K_{8\parallel}$ of the acoustical mode is much larger and determines the shape of the resonance field and causes the eightfold anisotropy. Although the $K_{8\parallel}$ is not zero in the other cases, it has only a small influence on the resonance field and is superimposed from the fourth order. Thus, the eighth order contribution can only be observed if the fourth order contribution is small. The reduction of the $K_{4\parallel}$ of the acoustical mode (magnetite film) of the bilayer to almost zero is probably due to the coupling to the optical mode (iron film). If we consider the $K_{4\parallel}$ of the single metallic iron film and the single magnetite film, we notice that the $K_{4\parallel}$ of iron film is larger than the $K_{4\parallel}$ of the magnetite film. In this case, the $K_{4\parallel}$ of the iron film superimpose the $K_{4\parallel}$ of the magnetite film.
We have also calculated $K_{4\parallel}$ for $K_{8\parallel}$=0 for all films except for the acoustical mode of the bilayer. In this case, the values for $K_{4\parallel}$ and the goodness-of-fit (not shown) are hardly affected confirming the small influence of the eight order of the magnetocrystalline anisotropy.

8.7 Summary

We prepared a single metallic iron film, a Fe_3O_4/Fe bilayer, and a single magnetite film by oxidizing previously grown Fe films on MgO(001). The stoichiometry of the iron oxide films corresponds to magnetite as proven by XPS. The structural analysis by XRD reveal that though the magnetite films are crystalline, they have inhomogeneous thicknesses. The Magnetization curves of the bilayer measured by MOKE exhibit a magnetic saturation which is comparable to the magnetic saturation of the single metallic iron film. However, the coercive field is higher compared to the metallic iron film due to the high interface roughness. Considering the coercive field as a function of the sample rotation α the bilayer exhibits

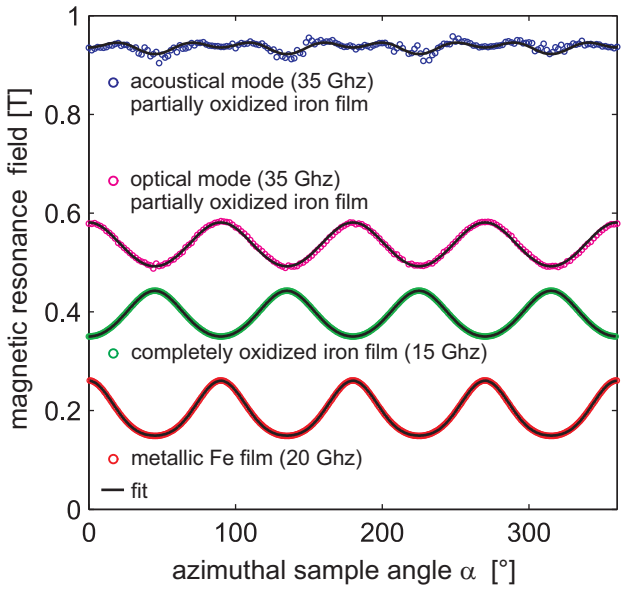

Fig. 8.14: Angular dependence of the in-plane resonance field of the 16.2 nm iron film (magenta) and the 29.1 nm iron oxide film (blue) of the Fe_3O_4/Fe bilayer. Maxima indicate magnetic hard directions, minima point to magnetic easy directions.

complex fourfold anisotropy with eight maxima. The angular dependence of the magnetic remanence features only simple fourfold anisotropy with easy axes in ⟨110⟩ directions of MgO(001). The magnetic easy axis of the magnetic in-plane anisotropy of the completely oxidized iron film is rotated by 45° compared to magnetite films grown directly on MgO as already observed in Ref. [98].

Vector MOKE analysis displays that the magnetic reversal processes of the bilayer are similar to single iron films. Thus, the bilayer exhibits mostly the magnetic properties of a single iron film with magnetic easy axis in ⟨110⟩ directions of MgO(001) and a high saturation magnetization. A magneto-dynamic investigation of the exchange-coupling Fe_3O_4/Fe bilayer system was carried out to yield all relevant magnetic parameters, such as anisotropies, as well as the coupling constant J_1. Here, also a complex fourfold magnetic anisotropy was observed at the acoustical mode of the bilayer, which might be due to a coupling of a perpendicular spin-wave mode in the magnetite layer with the acoustical coupling mode. We also successfully calculate the angular dependencies of the resonance fields of all films considering the eighth order of the magnetocrystalline anisotropy. However, the reason of the complex behavior of the angular dependence of the coercive field is still unknown and needs further investigations. In this case, the angular dependence of the coercive field is not viable to determine the magnetic easy or hard directions of the film. Here, the angular dependence of the remanence should be considered to determine the magnetic easy axis of the bilayer, which are in ⟨110⟩ directions of MgO(001). The optical mode of the bilayer measured by FMR conforms this results. Nevertheless, this bilayer provides interesting properties for application in MTJs due to its enhanced magnetic properties like coercive field and remanence.

8.8 Acknowledgements

Parts of this research were carried out at the light source PETRA III at DESY, a member of the Helmholtz Association (HGF). We would like to thank O. H. Seeck for assistance in using beamline P08. Thanks to Financial support by the DFG (KU2321/2-1) is gratefully acknowledged.

9 Summary and outlook

In this thesis the influence of different growth conditions on the structural and the magnetic properties of magnetite were analyzed. Therefore, ultrathin Fe_3O_4 films were grown on MgO(001) substrates, on NiO, and on Fe pre-covered MgO(001) substrates.
In the first part of this thesis magnetite films with different film thicknesses were deposited directly on MgO by RMBE to investigate the thickness dependence of the anomalous strain and the in-plane magnetic anisotropy. Surface sensitive methods like XPS and LEED have shown that all films in the investigated thickness range are stoichiometric and epitactic magnetite. Bulk sensitive XRD experiments at the specular rod point to well-ordered films with homogenous film thickness indicated by the distinct Laue oscillations. However, the vertical layer distances are smaller than expected even for strained magnetite. Raman measurements were carried out to clarify this contradiction between surface sensitive and bulk sensitive measurements. While the 20 nm and 30 nm films exhibit the typical bands for magnetite, no distinct bands can be observed for the 7.6 nm film. Due to this results we first assume a partial formation of a thin maghemite layer on top of the uncapped magnetite film under ambient conditions. Nevertheless, additional XPS measurement exclude the complete oxidation of magnetite to maghemite since there is no significantly increased Fe^{3+}-signal visible. Thus, the low vertical layer distance can be attributed to the presence of APBs causing an anomalous strain relaxation as reported in literature. Although all films feature ferromagnetic behavior there are differences in the characteristic of the magnetic in-plane anisotropy. The 7.6 nm film has an in-plane magnetic isotropy while the 20 nm and 30 nm film have an in-plane fourfold magnetic anisotropy. Here, the fourfold magnetic anisotropy is stronger for the 20 nm magnetite film than for the 30 nm film. The critical film thickness for the transition from magnetic isotropy to magnetic fourfold anisotropy may be influenced by film thickness and lattice strain induced by the substrate.
The second part of this thesis features the thickness dependence of the structural quality of Fe_3O_4/NiO bilayers. Each film of the Fe_3O_4/NiO bilayer on MgO(001) have been successfully grown by RMBE. LEED and XPS experiments have proven that the surface near regions of the distinct films have high structural and stoichiometric properties.
Here, too, the detailed 'bulk' structural characterization of Fe_3O_4/NiO bilayers were carried out using XRD. It was shown that the Fe_3O_4 films grow homogeneously and smoothly on NiO films if the NiO film thickness is below 24 nm. Above this NiO film thickness the structural quality of the magnetite films gets distinctly worse. This behavior can be attributed to the fact that the interface roughness between NiO and Fe_3O_4 depends on the NiO film thickness. The roughness of the 3 nm NiO film is rather small and it is rising obviously with increasing NiO film thickness. Thus, the structural quality of the magnetite films grown on 30 nm NiO films is constantly reduced with increasing magnetite film thickness since the quality of the Fe_3O_4 films is influenced by the quality of the Fe_3O_4/NiO interface.
In the third study the influence of initial iron buffer layers on the magnetic properties of magnetite grown on MgO(001) substrates has been investigated. *In situ* XPS and LEED indicate

that the structural and stoichiometric properties of the surface near region of the magnetite films are not influenced by the iron buffer layer. However, the structural and magnetic properties of the whole film have changed compared to magnetite grown directly on MgO as shown by XRD and MOKE. The crystalline quality is poor and the magnetic easy axis of the magnetic in-plane anisotropy is rotated by 45° compared to magnetite films grown directly on MgO. Both crystalline quality and the rotation of the magnetic in-plane anisotropy show no dependence on the film thickness. However, the strength of the magnetocrystalline anisotropy decreases with increasing film thickness. XPS and XRD measurements have indicated that the iron buffer layer is completely oxidized during the second growth stage of the magnetite. The small Kerr rotation in the MOKE experiments of the samples with film thicknesses up to 28 nm confirms this result since a remaining iron film would cause a higher Kerr rotation. In the last part of this thesis the structural and magnetic properties of a partially oxidized, a completely oxidized and a metallic iron film are analyzed. The partially oxidized iron film is a bilayer with a metallic iron film and an iron oxide film. The surface near stoichiometry of both oxidized iron films correspond to magnetite as proven by XPS. The structural analysis by XRD reveals that though these magnetite films are crystalline, they have an inhomogeneous thickness. The magnetization curves of the partially oxidized film (bilayer) measured by MOKE exhibit a magnetic saturation which is comparable to the magnetic saturation of the single metallic iron film. However, the coercive field is higher compared to the single metallic iron film due to the high interface roughnesses. Considering the coercive field as a function of the sample rotation α the bilayer exhibits a fourfold anisotropy with eight maxima. However, the angular dependence of the magnetic remanence features a simple fourfold anisotropy with easy axes in $\langle 110 \rangle$ directions of MgO(001). Vector MOKE analysis displays that the magnetic reversal processes of the bilayer are similar to single metallic iron films. Thus, the bilayer exhibits mostly the magnetic properties of a single iron film. The bilayer has the same magnetic easy axis and a similar magnetic saturation. The magnetic easy axis of the magnetic in-plane anisotropy of the completely oxidized iron film is rotated by 45° compared to magnetite films grown directly on MgO as already observed in Ref. [98]. The completely oxidized iron film exhibits also a significantly increased coercive field due to high surface roughness.

A magneto-dynamic investigation of the exchange-coupling of the Fe_3O_4/Fe bilayer system was carried out to yield all relevant magnetic parameters, such as anisotropies, as well as the coupling constant J_1. Here, also a complex fourfold anisotropy was observed, which might be due to a coupling of a perpendicular spin-wave mode in the magnetite layer with the acoustical coupling mode. We have also successfully calculated the angular dependence of the resonance field of all films using the eighth order of the magnetocrystalline anisotropy. Although we have applied many measurement methods, we have found no explanation for the complex fourfold angular dependence of the coercive field of the bilayer. Nevertheless, this bilayer provides interesting properties for application in MTJs due to its enhanced magnetic properties like complex fourfold magnetic anisotropy and higher coercive field and remanence.

All in all, we have shown that the structural and magnetic properties of magnetite films are strongly influenced by interlayers between film and substrate. While magnetite films directly deposited on MgO exhibit a homogeneous film thickness, both NiO interlayers with a thickness above 24 nm and initially grown iron films deteriorate the structural quality of the on top grown magnetite films. In addition, the magnetic fourfold anisotropy is rotated by 45° in comparison to magnetite films grown directly on MgO for the structurally disturbed magnetite on iron pre-covered MgO substrates. Here, further investigations are necessary to under-

stand why this anisotropy rotation occurs and how we can improve the structural quality of magnetite on iron and NiO. The growth of magnetite by oxidizing previously deposited iron films leads to crystalline magnetite films but with inhomogeneous film thicknesses. In case of a Fe_3O_4/Fe bilayer, the magnetic properties are drastically changed due to the magnetic coupling between the iron and the magnetite film.
In this study, we used solely MgO substrates which are modified by additional layers. Further investigation should focus on the growth of magnetite on other substrates like $SrTiO_3(001)$ (perovskite structure), $Al_2O_3(0001)$ (corundum structure), and $MgAl_2O_4(001)$ (spinel structure) as already shown in literature [118–122]. $SrTiO_3(001)$ and $Al_2O_3(0001)$ substrates have a distinct smaller lattice constant than magnetite resulting in a large lattice misfit of 7.5 % and 8 %, respectively. Thus, a high strain could be induced in magnetite films grown on $SrTiO_3(001)$ and $Al_2O_3(0001)$ substrates and leads to altered structural and magnetic properties of the film [118]. $MgAl_2O_4(001)$ has a similar lattice constant to magnetite (lattice misfit 4 %) and crystallizes also in spinel structure. Thus, the formation of APBs could be reduced, which might have a huge inpact on the magnetic properties of magnetite films. Here, it would be also interesting to know how additional interlayers on $SrTiO_3$, Al_2O_3 and $MgAl_2O_4$ influence the properties of the on top grown magnetite.

10 List of publications

Peer-reviewed publications

- F. Bertram, C. Deiter, O. Hoefert, M. Suendorf, T. Schemme, F. Timmer, B. Zimmermann, and J. Wollschläger
"X-ray diffraction study on size effects in epitaxial magnetite thin films on MgO(001)"
Journal of Physics D: Applied Physics **45**, 395302 (2012)
doi:10.1088/0022-3727/45/39/395302
- F. Bertram, C. Deiter, T. Schemme, S. Jentsch, and J. Wollschläger
"Reordering between tetrahedral and octahedral sites in ultrathin magnetite films grown on MgO(001)"
Journal of Applied Physics **113**, 184103 (2013)
doi:10.1063/1.4803894
- D. Bruns, S. R. Lindemann, K. Kuepper, T. Schemme, and J. Wollschläger
"Fe_3O_4 films on Ag(001)-Generation of high-quality epitaxial ferrimagnetic metal oxide films"
Applied Physics Letters **103**, 052401 (2013)
doi:10.1063/1.4816787
- D. Bruns, I. Kiesel, S. Jentsch, S. R. Lindemann, C. Otte, T. Schemme, T. Kuschel, and J. Wollschläger
"Structural analysis of FeO(111)/Ag(001): undulation of hexagonal oxide monolayers due to square lattice metal substrates"
Journal of Physics: Condensed Matter **26**, 315001 (2014)
doi:10.1088/0953-8984/26/31/315001
- T. Schemme, N. Pathé, G. Niu, F. Bertram, T. Kuschel, K. Kuepper, and J. Wollschläger
"Magnetic anisotrophy related to strain and thickness of ultrathin iron oxide films on MgO(001)"
Material Research Express **2**, 016101 (2015)
doi:10.1088/2053-1591/2/1/016101
- L. Marnitz, K. Rott, S. Niehörster, C. Klewe, D. Meier, S. Fabretti, M. Witziok, A. Krampf, O. Kuschel, T. Schemme, K. Kuepper, J. Wollschläger, A. Thomas, G. Reiss, and T. Kuschel
"Sign change in the tunnel magnetoresistance of Fe3O4/MgO/Co-Fe-B magnetic tunnel junctions depending on the annealing temperature and the interface treatment"
AIP Advances **5**, 047103 (2015)
doi:10.1063/1.4917018
- T. Schemme, O. Kuschel, F. Bertram, K. Kuepper and J. Wollschläger
"Structure and morphology of epitaxially grown Fe_3O_4/NiO bilayers on MgO(001)"

Thin Solid Films **589**, 526 (2015)
doi:10.1016/j.tsf.2015.06.018

- T. Kuschel, C. Klewe, J.-M. Schmalhorst, F. Bertram, O. Kuschel, T. Schemme, J. Wollschläger, S. Francoual, J. Strempfer, A. Gupta, M. Meinert, G. Götz, D. Meier, and G. Reiss
"Static magnetic proximity effect in $Pt/NiFe_2O_4$ and Pt/Fe bilayers investigated by x-ray resonant magnetic reflectivity"
Physical Review Letters **115**, 097401 (2015)
doi:10.1103/PhysRevLett.115.097401

- T. Schemme, A. Krampf, F. Bertram, T. Kuschel, K. Kuepper, and J. Wollschläger
"Modifying magnetic properties of ultra-thin magnetite films by growth on Fe precovered MgO(001)"
Journal of Applied Physics **118**, 113904 (2015)
doi:10.1063/1.4930998

- J. Wollschläger, T. Schemme, O. Kuschel, M. Witziok, T. Kuschel, K. Kuepper
"Structural, magnetic and magneto optical properties of Fe_3O_4/NiO bilayers on MgO(001)"
Proc. SPIE 9749, Oxide-based Materials and Devices VII, **974917** (2016)

- K. Kuepper, O. Kuschel, O. Pathé, T. Schemme, J. Schmalhorst, A. Thomas, E. Arenholz, M. Gorgoi, R. Ovsyannikov, S. Bartkowski, G. Reiss, and J. Wollschläger
"Electronic and magnetic structure of epitaxial Fe_3O_4(001)/NiO heterostructures grown on MgO(001) and Nb-doped $SrTiO_3$(001)"
Physical Review B **94**, 024401 (2016)
doi:10.1103/PhysRevB.94.024401

- O. Kuschel, R. Buß, W. Spiess, T. Schemme, J. Wöllermann, K. Balinski, A. T. N'Diaye, T. Kuschel, J. Wollschläger, and K. Kuepper
"From Fe_3O_4/NiO bilayers to $NiFe_2O_4$-like thin films through Ni interdiffusion"
Physical Review B **94**, 094423 (2016)
doi:10.1103/PhysRevB.94.094423

Submitted publications

- M. Suendorf, T. Schemme, A. Thomas, J. Wollschläger, and K. Kuepper
"Link between local iron coordination, Fe 2p XPS core level line shape and Mg segregation into thin magnetite films grown on MgO(001)"
submitted (2015), arxiv: 1501.07443

- O. Kuschel, N. Pathé, T. Schemme, K. Ruwisch, J. Rodewald, R. Buß, F. Bertram, T. Kuschel, K. Kuepper, J. Wollschläger
"Impact of strain and morphology on magnetic properties of Fe_3O_4/NiO bilayers grown on Nb:$SrTiO_3$(001) and MgO(001)"
submitted (2015), arxiv: 1611.04402

Non reviewed publications

- F. Bertram, C. Deiter, S. Jentsch, T. Schemme, and J. Wollschläger
  "Disorder on tetrahedral sites of ultra thin magnetite films grown on MgO(001)"
  HASYLAB Annual Report (2011)
- T. Schemme, F. Bertram, D. Bruns, T. Kuschel, and J. Wollschläger
  "XRR and XRD studies on magnetic iron oxide films on MgO(001)"
  HASYLAB Annual Report (2011)
- T. Schemme, O. Schuckmann, F. Bertram, J. Strempfer, S. Francoual, and J. Wollschläger
  "Epitaxial Fe_3O_4/NiO bilayers grown on MgO(001)"
  HASYLAB Annual Report (2012)
- F. Bertram, C. Deiter, T. Schemme, and J. Wollschläger
  "Post-deposition annealing induced reordering of tetrahedral sites in ultra thin magnetite films grown on MgO(001)"
  HASYLAB Annual Report (2012)
- T. Schemme, D. Bruns, J. Wöllermann, O. Schuckmann, K. Kuepper, and J. Wollschläger
  "Thermal stability of epitaxial Fe_3O_4/NiO bilayers on MgO(001)"
  SLS Beamtime Report (2013)
- T. Schemme, J. Bosse, O. Schuckmann, F. Bertram, J. Strempfer, T. Kuschel, K. Kuepper, S. Francoual, and J. Wollschläger
  "Epitaxial Fe_3O_4/NiO bilayers grown on MgO(001)"
  HASYLAB Annual Report (2013)
- O. Schuckmann, T. Schemme, N. Pathé, F. Timmer, F. Bertram, T. Kuschel, O. Gutowsky, U. Rütt, and J. Wollschläger
  "HESXRD studies on ultrathin magnetite films grown on Nb doped $SrTiO_3$(001)"
  HASYLAB Annual Report (2013)
- T. Kuschel, C. Klewe, J.-M. Schmalhorst, F. Bertram, E. Lundgren, O. Schuckmann, T. Schemme, J. Wollschläger, S. Francoual, J. Strempfer, and G. Reiss
  "Epitaxial Fe_3O_4/NiO bilayers grown on MgO(001)"
  HASYLAB Annual Report (2013)
- T. Schemme, A. Krampf, J. Bosse, F. Timmer, K. Kuepper, O. Seeck, and J. Wollschläger
  "Cubic magnetocrystalline anisotropies in ultrathin epitaxial magnetite films grown on MgO(001)"
  HASYLAB Annual Report (2013)

Literature

[1] E. R. Hedin and Y. S. Joe (Editors). *Spintronic in Nanoscale Devices.* CRC Press Taylor & Francis Group, 2014.

[2] S. A. Wolf, D. D. Awschalom, R. A. Buhrman, J. M. Daughton, S. von Molnar, M. L. Roukes, A. Y. Chtchelkanova and D. M. Treger. "Spintronics: A Spin-Based Electronics Vision for the Future". *Science*, 294, 1488, 2001.

[3] Y. Peng, C. Park, J. Zhu, R. M. White and D. E. Laughlin. "Characterization of interfacial reactions in magnetite tunnel junctions with transmission electron microscopy". *Journal of Applied Physics*, 95, 6798, 2004.

[4] J. Moodera, L. Kinder, T. Wong and R. Meservey. "Large Magnetoresistance at Room Temperature in Ferromagnetic thin Film Tunnel Junctions". *Physical Review Letters*, 74, 3273, 1995.

[5] M. Bibes and A. Barthelemy. "Oxide Spintronics". *Electron Devices, IEEE Transactions*, 54, 1003, 2007.

[6] I. Žutić, J. Fabian and S. D. Sarma. "Spintronics: Fundamentals and applications". *Reviews of Modern Physics*, 76, 323, 2004.

[7] M. Julliere. "Tunneling between ferromagnetic films". *Physics Letters A*, 54, 225, 1975.

[8] E. Y. Tsymbal, O. N. Meyasov and P. R. LeClair. "Spin-dependent tunnelling in magnetic tunnel junctions". *Journal of Physics: Condensed Matter*, 15, R109, 2003.

[9] Z. Zhang and S. Satpathy. "Electron states, magnetism, and the Verwey transition in magnetite". *Physical Review B*, 44, 13319, 1991.

[10] W. Wang, J.-M. Mariot, M. C. Richter, O. Heckmann, W. Ndiaye, P. D. Padova, A. Taleb-Ibrahimi, P. L. Fèvre, F. Bertran, F. Bondino, E. Magnano, J. Krempaský, P. Blaha, C. Cacho, F. Parmigiani and K. Hricovini. "Fe t_{2g} band dispersion and spin polarization in thin films of Fe_3O_4(001)/MgO(001): Half-metallicity of magnetite revisited". *Physical Review B*, 87, 085118, 2013.

[11] S. Ikeda, J. Hayakawa, Y. M. Lee, F. Matsukura, Y. Ohno, T. Hanyu and H. Ohno. "Magnetic tunnel junctions for spintronic memories and beyond." *IEEE Xplore: IEEE Transactions on Electron Devices*, 54, 991, 2007.

[12] F. Bertram, C. Deiter, K. Pflaum, M. Suendorf, C. Otte and J. Wollschläger. "In-situ x-ray diffraction studies on post-deposition vacuum-annealing of ultra-thin iron oxide films". *Journal of Applied Physics*, 110, 102208–102208–5, 2011.

[13] F. Bertram, C. Deiter, O. Hoefert, T. Schemme, F. Timmer, M. Suendorf, B. Zimmermann and J. Wollschläger. "X-ray diffraction study on size effects in epitaxial magnetite thin films on MgO(0 0 1)". *Journal of Applied Physics D: Applied Physics*, 45, 395302, 2012.

[14] F. Bertram, C. Deiter, T. Schemme, S. Jentsch and J. Wollschläger. "Reordering between tetrahedral and octahedral sites in ultrathin magnetite films grown on MgO(001)". *Journal of Applied Physics*, 113, 184103, 2013.

[15] N. W. Ashcroft and D. N. Mermin. *Festkörperphysik*. Oldenbourg Wissenschaftsverlag, 2001.

[16] C. Kittel. *Einführung in die Festkörperphysik.* Oldenbourg Wissenschaftsverlag, 2006.

[17] K. Oura, V. Lifshits, A. Saranin and M. Katayama. *Surface Science.* Springer, 2003.

[18] A. Bravais. "Mémoire sur les systèmes formés par les points distribués régulièrement sur un plan ou dans l'espace." *Journal de l'École polytechnique*, 19, 1, 1850.

[19] K. Kopitzki and P. Herzog. *Einführung in die Festkörperphysik, 5. ed.* Teubner, 2004.

[20] S. Hashimoto, J.-L. Peng, W. Gibson, L. J. Schowalter and R. W. Fathauer. "Strain measurement of epitaxial CaF_2 on Si(111) by MeV ion channeling". *Applied Physical Letter*, 47, 1071, 1985.

[21] P. M. Marcus. "Epitaxial strain and epitaxial bending." *Surface Science*, 366, 219, 1996.

[22] T. Hammerschmidt, P. Kratzer and M. Scheffler. "Elastic response of cubic crystals to biaxial strain: Analytic results and comparison to density functional theory for InAs." *Physical Review B*, 75, 235328, 2007.

[23] A. G. Every and A. K. McCurdy. *Table 7. Cubic system. Binary Compounds.* Springer Berlin Heidelberg, 1992.

[24] G. E. Sterbinsky, J. Cheng, P. T. Chiu, B. W. Wessels and D. J. Keavney. "Investigation of heteroepitaxial growth of magnetite thin films". *Journal of Vacuum Science & Technology, B*, 25, 1389, 2007.

[25] L. Horng, G. Chern, M. Chen, P. Kang and D. Lee. "Magnetic anisotropic properties in Fe_3O_4 and $CoFe_2O_4$ ferrite epitaxy thin films". *Journal of Magnetism and Magnetic Materials*, 270, 389, 2004.

[26] T. Schemme, N. Pathé, G. Niu, F. Bertram, T. Kuschel and J. Wollschläger. "Magnetic anisotropy related to strain and thickness of ultrathin iron oxide films on MgO(001)". *Materials Research Express*, 2, 016101, 2015.

[27] D. M. Lind, S. D. Berry, G. Chern, H. Mathias and L. R. Testardi. "Growth and structural characterization of Fe_3O_4 and NiO thin films and superlattices grown by oxygen-plasma-assisted molecular-beam epitaxy". *Physical Review B*, 45, 1838, 1992.

[28] T. Fujii, F. M. F. de Groot, G. A. Sawatzky, F. C. Voogt, T. Hibma and K. Okada. "In situ XPS analysis of various iron oxide films grown by NO2-assisted molecular-beam epitaxy". *Physical Review B*, 59, 3195, 1999.

[29] X. W. Li, A. Gupta, G. Xiao, W. Qain and V. P. Dravid. "Fabrication and properties of heteroepitaxial magnetite (Fe_3O_4) tunnel junctions". *Applied Physics Letters*, 73, 3282, 1998.

[30] D. T. Margulies, F. T. Parker, F. E. Spada, R. S. Goldman, J. Li, R. Sinclair and A. E. Berkowitz. "Anomalous moment and anisotropy behavior in Fe_3O_4 films". *Physical Review B*, 53, 9175, 1996.

[31] K. Balakrishnan, S. K. Arora and I. V. Shvets. "Strain relaxation studies of the Fe_3O_4/MgO (100) heteroepitaxial system grown by magnetron sputtering". *Journal of Physics: Condensed Matter*, 16, 5387, 2004.

[32] W. Friedrich, P. Knipping and M. Laue. "Interferenz-Erscheinungen bei Röntgenstrahlen". *Die Naturwissenschaften*, 16, 361, 1952.

[33] W. H. Bragg and W. L. Bragg. "The Reflection of X-rays by Crystals". *Proceedings of the Royal Society of London A: Mathematical, Physical and Engineering Sciences*, 88, 428, 1913.

[34] R. Feidenhans'l. "Surface structure determination by X-ray diffraction". *Surface Science Reports*, 10, 105, 1989.

[35] I. K. Robinson and D. J. Tweet. "Surface X-ray diffraction". *Reports on Progress in Physics*, 55, 599, 1992.

[36] C. Deiter. *Röntgenstrukturanalyse von Halbleiter-Isolator-Schichtsystemen.* Ph.D. thesis, Universität Bremen, 2005.

[37] F. Bertram. *The structure of ultrathin iron oxide films studied by X-ray diffraction.* Ph.D. thesis, Universität Osnabrück, 2012.

[38] Birmingham. *International tables for X-ray crystallography 3. Edition.* Kynoch Press for the International Union of Crystallography, 1976.

[39] B. T. M. Willis and A. W. Pryor. *Thermal vibration in crystallography.* Cambridge University Press, 1975.

[40] B. E. Warren. *X-ray Diffraction.* Dover Publications, Inc., New York, 1990.

[41] M. Ladd and R. Palmer. *Structure determination by x-ray crystallography.* Kluwer Academic Publishers, 2003.

[42] F. Bertram. *The structure of ultrathin iron oxide films studied by x-ray diffraction.* Ph.D. thesis, Universität Osnabrück, 2012.

[43] J. Als-Nielsen and D. McMorrow. *Elements of Modern X-Ray Physics.* John Wiley & Sons Inc., 2000.

[44] M. Tolan. *X-Ray Scattering from Soft-Matter Thin Films - Materials Science and Basic Research.* Springer-Verlag, 1999.

[45] L. Parratt. "Surface studies of solids by total reflection of x-rays". *Review of Modern Physics*, 95, 359, 1954.

[46] L. Névot and P. Croce. "Caractérisation des surfaces par réflexion rasante de rayons X. Application à létude du polissage de quelques verres silicates". *Revue de Physique Appliquée*, 15, 761, 1980.

[47] C. Kittel. "Physical theory of ferromagnetic domains." *Review of Modern Physics*, 21, 541, 1949.

[48] A. Barbier, C. Mocuta and G. Renaud. "Structure, transformation, and reduction of the polar NiO(111) surface." *Physisical Review B*, 62, 16056, 2000.

[49] C. Gatel, E. Snoeck, V. Serin and A. R. Fert. "Epitaxial growth and magnetic exchange anisotropy films$_3O_4$/NiO bilayers grown on MgO(001) and Al_2O_3(0001)". *The European Physical Journal B*, 45, 157, 2005.

[50] A. P. Malozemoff. “Heisenberg-to-Ising crossover in a random-field model with uniaxial anisotropy”. *Physical Review B*, 37, 7673, 1988.

[51] A. P. Malozemoff. “Random-field model of exchange anisotropy at rough ferromagnetic-antiferromagnetic interfaces”. *Physical Review B*, 35, 3679, 1987.

[52] J. Kerr. “On rotation of the plane of polarization by reflection from the pole of a magnet.” *Philosophical Magazine*, 3, 321, 1877.

[53] C. Robinson. “Longitudinal Kerr magneto-optic effect in thin films of iron, nickel, and permalloy.” *Journal of the Optical Society of America*, 53, 681, 1963.

[54] W. Reim and J. Schoenes. “Chapter 2 Magneto-optical spectroscopy of f-electron systems”. *Handbook of Ferromagnetic Materials*, 5, 133, 1990.

[55] R. Jones. “A new calculus for the treatment of optical systems.” *Journal of the Optical Society of America*, 31, 488, 1941.

[56] J. Hamrle, S. Blomeier, O. Gaier, B. Hillebrands, H. Schneider, G. Jakob, K. Postava, and C. Felser. “Huge quadratic magneto-optical Kerr effect and magnetization reversal in the Co_2FeSi Heusler compound.” *Journal of Physics D: Applied Physics*, 40, 1563, 2007.

[57] G. Metzger, P. Pluvinage and R. Torguet. “Termes linéaires et quadratiques dans l’effet magnéto-optique de Kerr.” *Annales de Physique (Paris)*, 10, 5, 1965.

[58] Q.-M. Zhong, A. Arrott, B. Heinrich and Z. Celinski. “Surface magneto-optical Kerr effect for ultrathin Ni-Fe bilayers.” *Journal of Applied Physics*, 67, 4448, 1990.

[59] Š. Višňovský. “Magneto-optical permittivity tensor in crystals.” *Czechoslovak Journal of Physics*, 36, 1424, 1986.

[60] T. Kuschel, H. Bardenhagen, H. Wilkens, R. Schubert, J. Hamrle, J. Pištora and J. Wollschläger. “Vectorial magnetometry using magnetooptic Kerr effect including first- and second-order contributions for thin ferromagnetic films”. *Journal of Physics D: Applied Physics*, 44, 265003, 2011.

[61] P. Grünberg, R. Schreiber, Y. Pang, M. Brodsky and H. Sowers. “Layered magnetic structures: Evidence for antiferromagnetic coupling of Fe layers across Cr interlayers”. *Physical Review Letters*, 57, 2442, 1986.

[62] L. Landau and E. Lifshitz. “On the theory of magnetic permeability in ferromagnetic bodies.” *Physikalische Zeitschrift der Sowjetunion*, 8, 153, 1935.

[63] J. Smit and H. Beljers. “Ferromagnetic resonance absorption in $BaFe_{12}O_{19}$ a highly anisotropic crystal”. *Philips Research Reports*, 10, 113, 1955.

[64] H. Suhl. “Ferromagnetic Resonance in Nickel Ferrite Between One and Two Kilomegacycles”. *Physical Review*, 97, 555, 1955.

[65] T. L. Gilbert. “A Lagrangian formulaform of the gyromagnetic equation of the magnetization field.” *Physical Review*, 100, 1243, 1955.

[66] A. Venter and J. R. Botha. “Optical and electrical properties of NiO for possible dielectric applications”. *South African Journal of Science*, 107, 6, 2011.

[67] R. Cornell and U. Schwertmann. *The Iron Oxides: Structure, Properties, Reactions, Occurences and Uses*. Wiley-VCH GmbH & Co. KGaA, 2003.

[68] P. Weiss and R. Forrer. “The absolute saturation of ferro-magnetic and laws of approach according to the field and the temperature”. *Annalen der Physik*, 12, 279, 1929.

[69] M. Jackson, J. Bowles and S. Banerjee. “Interpretation of Low-Temperature Data Part V: The Magnetite Verwey Transition (Part B): Field-Cooling Effects on Stoichiometric Magnetite Below T_V”. *The IRM Quarterly*, 21, 1, 2011.

[70] R. Dronskowski. “The Little Maghemite Story. A Classic Functional Material”. *Advanced Functional Materials*, 11, 27, 2001.

[71] D. J. Dunlop and O. Özdemir. *Rock Magnetism: Fundamentals and Frontiers*. Cambridge University Press, 1997.

[72] R. Grau-Crespo, I. S. A. Y Al-Baitai and N. H. D. Leeuw. “Vacancy ordering and electronic structure of γ-Fe_2O_3 (maghemite): a theoretical investigation”. *Journal of Physics: Condensed Matter*, 22, 255401, 2010.

[73] W. Eerenstein, T. T. M. Palstra, T. Hibma and S. Celotto. “Origin of the increased resistivity in epitaxial Fe_3O_4 films.” *Physical Review B*, 66, 201101, 2002.

[74] T. Hibma, F. Voogt, L. Niesen, P. van der Heijden, W. de Jonge, J. Donkers and P. van der Zaag. “Anti-phase domains and magnetism in epitaxial magnetite layers”. *Journal of Applied Physics*, 85, 5291, 1999.

[75] W. Eerenstein, T. T. M. Palstra, T. Hibma and S. Celotto. “Diffusive motion of antiphase domain boundaries in Fe_3O_4 films.” *Physical Review B*, 68, 014428, 2003.

[76] S. Celotto, W. Eerenstein and T. Hibma. “Characterization of anti-phase boundaries in epitaxial magnetite films”. *The European Physical Journal B*, 36, 271, 2003.

[77] J.-B. Moussy, S. Gota, A. Bataille, M.-J. Guittet, M. Gautier-Soyer, F. Delille, B. Dieny, F. Ott, T. D. Doan, P. Warin, P. Bayle-Guillemaud, C. Gatel and E. Snoeck. “Thickness dependence of anomalous magnetic behavior in epitaxial Fe_3O_4(111) thin films: Effect of density of antiphase boundaries”. *Physical Review B*, 70, 174448, 2004.

[78] T. Yamashita and P. Hayes. “Analysis of XPS spectra of Fe^{2+} and Fe^{3+} ions in oxide materials”. *Applied Surface Science*, 254, 2441–2449, 2008.

[79] J. F. Anderson, M. Kuhn and U. Diebold. “Surface structure and morphology of Mg-segregated epitaxial Fe_3O_4(001) thin films on MgO(001)”. *Physical Review B*, 56, 9902, 1997.

[80] J. Korecki, B. Handke, N. Spiridis, T. Ślęzak, I. Flis-Kabulska and J. Haber. “Size effects in epitaxial films of magnetite”. *Thin Solid Films*, 412, 14–23, 2002.

[81] R. Pentcheva, W. Moritz, J. Rundgren, S. Frank, D. Schrumpf and M. Scheffler. “A combined DFT/LEED-approach for complex oxide surface structure determination: Fe_30_4(001)”. *Surface Science*, 602, 1299, 2008.

[82] K. Balinski. *Entwicklung einer Ansteuerungssoftware fÃ¼r eine magneto-optische Messapparatur.* Master’s thesis, Universität Osnabrück, 2010.

[83] H. Wilkens. *Röntgen- und Vektor-MOKE-Untersuchung ferromagnetischer Fe-Schichten.* Master’s thesis, Universität Osnabrück, 2010.

[84] D. K. Ball. *From 2D CoCrPt:SiO_2 films with perpendicular magnetic anisotropy to 3D nanocones - A step towards bit patterned media* -. Ph.D. thesis, Technische Universität Dresden, 2012.

[85] O. H. Seeck, C. Deiter, K. Pflaum, F. Bertam, A. Beerlink, H. Franz, J. Horbach, H. Schulte-Schrepping, B. M. Murphy, M. Greve and O. Magnussen. "The high-resolution diffraction beamline P08 at PETRA III". *Journal of Synchroton Radiation*, 19, 30–38, 2012.

[86] HASYLAB. http://photon-science.desy.de/facilities/petra_iii/beamlines/p08_highres_diffraction/index_eng.html.

[87] K. Wille. *Physik der Teilchenbeschleuniger und Synchrotronstrahlungsquellen., 2. edition.* Teubner, 1996.

[88] W. Scharf and F. T. Cole. *Particle ccelerators and their uses.* Harwood Academic Publishers, 1991.

[89] J. Als-Nielsen and D. McMorrow. *Elements of Modern X-Ray Physics.* John Wiley & Sons Inc., 2000.

[90] T. Möller and J. F. (Editors). *Forschung mit Synchrotronstrahlung: Eine Einführung in die Grundlagen und Anwendungen.* Vieweg+Teubner Verlag, 2010.

[91] H. You. "Angle calculations for a '4S+2D' six-circle diffractometer". *Journal of Applied Crystallography*, 32, 614, 1999.

[92] B. Schmitt, C. Brönnimann, E. Eikenberry, F. Gozzo, C. Hörmann, R. Horisberger and B. Patterson. "Mythen detector system". *Nuclear Instruments and Methods in Physics Research Section A: Accelerators, Spectrometers, Detectors and Associated Equipment*, 501, 267, 2003.

[93] S. Yuasa, T. Nagahama, A. Fukushima, J. Suzuki and K. Ando. "Giant roomtemperature magnetoresistance in single-crystal Fe/MgO/Fe magnetic tunnel junctions". *Nature Materials*, 3, 868, 2004.

[94] C. Klewe, M. Meinert, J. Schmalhorst and G. Reiss. "Negative spin polarization of Mn_2VGa probed by tunnel magnetoresistance". *Journal of Physics: Condensed Matter*, 25, 076001, 2013.

[95] D. V. Dimitrov, A. S. Murthy, C. P. Swann and G. C. Hadjipanayis. "Magnetic properties of exchange-coupled Fe/FeO bilayers". *Journal of Applied Physics*, 79, 5106, 1996.

[96] M. Ziese, R. Höhne, H. Semmelhack, H. Reckentin, N. Hong and P. Esquinazi. "Mechanism of grain-boundary magnetoresistance in Fe_3O_4 films". *European Physical Journal B: Condensed Matter Physics*, 28, 415, 2002.

[97] J. Goodenough, W. Gräper, F. Holtzberg, D. Huber, R. Lefever, J. Longo, T. McGuire, S. Methfessel, K.-H. Hellwege and A. M. Hellwege. *Magnetic and Other Properties of Oxides and Related Compounds, Landolt Börnstein, New Series, Group III Pt. b*, volume 4. Springer-Verlag, 1970.

[98] T. Schemme, A. Krampf, F. Bertram, T. Kuschel, K. Kuepper and J. Wollschläger. "Modifying magnetic properties of ultra-thin magnetite films by growth on Fe precovered MgO(001)". *Journal of Applied Physics*, 118, 113904, 2015.

[99] T. Kuschel, T. Becker, D. Bruns, M. Suendorf, F. Bertram, P. Fumagalli and J. Wollschläger. "Uniaxial magnetic anisotropy for thin Co films on glass studied by magnetooptic Kerr effect". *Journal of Applied Physics*, 109, 093907, 2011.

[100] C. Daboo, J. A. C. Bland, R. J. Hicken, A. J. R. Ives, M. J. Baird and M. J. Walker. "Vectorial magnetometry with the magneto-optic Kerr effect applied to Co/Cu/Co trilayer structures". *Physical Review B*, 47, 11852, 1993.

[101] P. C. Graat and M. A. Somers. "Simultaneous determination of composition and thickness of thin iron-oxide films from XPS Fe 2p spectra". *Applied Surface Science*, 100/101, 36, 1996.

[102] G. Bhargava, I. Gouzman, C. Chun, T. Ramanarayanan and S. Bernasek. "Characterization of the "native" surface thin film on pure polycrystalline iron: A high resolution XPS and TEM study". *Applied Surface Science*, 253, 4322, 2007.

[103] D. D. Hawn and B. M. DeKoven. "Deconvolution as a correction for photoelectron inelastic energy losses in the core level XPS spectra of iron oxides". *Surface and Interface Analysis*, 10, 63, 1987.

[104] M. Muhler, R. Schlögl and G. Ertl. "The nature of the iron oxide-based catalyst for dehydrogenation of ethylbenzene to styrene 2. Surface chemistry of the active phase". *Journal of Catalysis*, 138, 413, 1992.

[105] H. Oka, A. Subagyo, M. Sawamura, K. Sueoka and K. Mukasa. "Scanning Tunneling Spectroscopy of c(2×2) Reconstructed Fe Thin-Film Surfaces". *Japanese Journal of Applied Physics*, 40, 4334, 2001.

[106] C. M. Boubeta, J. L. Costa-Krämer and A. Cebollada. "Epitaxy, magnetic and tunnel properties of transition metal/MgO(001) heterostructures". *Journal of Physics: Condensed Matter*, 15, R1123, 2003.

[107] D. T. Margulies, F. T. Parker and A. E. Berkowitz. "Magnetic anomalies in single crystal Fe_3O_4 thin films". *Journal of Applied Physics*, 75, 6097, 1994.

[108] J. Cheng, G. Sterbinsky and B. Wessels. "Magnetic and magneto-optical properties of heteroepitaxial magnetite thin films". *Journal of Crystal Growth*, 310, 3730, 2008.

[109] T. Kuschel, J. Hamrle, J. Pištora, K. Saito, S. Bosu, Y. Sakuraba, K. Takanashi and J. Wollschläger. "Magnetic characterization of thin $Co_{50}Fe_{50}$ films by magnetooptic Kerr effect". *Journal of Physics D: Applied Physics*, 45, 495002, 2012.

[110] J. Hamrle, S. Blomeier, O. Gaier, B. Hillebrands, R. Schäfer and M. Jourdan. "Magnetic anisotropies and magnetization reversal of the $Co_2Cr_{0.6}Fe_{0.4}Al$ Heusler compound". *Journal of Applied Physics*, 100, 103904, 2006.

[111] L. Baselgia, M. Warden, F. Waldner, S. L. Hutton, J. E. D. , Y. Q. He, P. E. Wigen and M. Maryško. "Derivation of the resonance frequency from the free energy of ferromagnets". *Physical Review B*, 38, 2237, 1988.

[112] J. Lindner and K. Baberschke. "Ferromagnetic resonance in coupled ultrathin films". *Journal of Physics: Condensed Matter*, 15, S465, 2003.

[113] P. E. Tannenwald and M. H. Seavey. "Ferromagnetic Resonance in Thin Films of Permalloy". *Physical Review*, 105, 377, 1957.

[114] M. H. Seavey and P. E. Tannenwald. "Direct Observation of Spin Wave Resonance". *Journal of Applied Physics*, 30, 227, 1959.

[115] S. O. Demokritov, B. Hillebrands and A. N. Slavin. "Brillouin light scattering studies of confined spin waves: Linear and nonlinear confinement". *Physics Reports*, 348, 441, 2001.

[116] B. A. Kalinikos and A. N. Slavin. “Theory of dipole-exchange spin wave spectrum for ferromagnetic films with mixed exchange boundary conditions”. *Journal of Physics C: Solid State Physics*, 19, 7013, 1986.

[117] R. Aragón. “Cubic magnetic anisotropy of nonstoichiometric magnetite”. *Physical Review B*, 46, 5334, 1992.

[118] M. Monti, M. Sanz, M. Oujja, E. Rebollar, M. Castillejo, F. J. Pedrosa, A. Bollero, J. Camarero, J. L. F. C. nado, N. M. Nemes, F. J. Mompean, M. Garcia-HernÃ¡ndez, S. Nie, K. F. McCarty, A. T. N’Diaye, G. Chen, A. K. Schmid, J. F. Marco and J. de la Figuera. “Room temperature in-plane ⟨100⟩ magnetic easy axis for $Fe_30_4/SrTiO_3$(001):Nb grown by infrared pulsed laser deposition”. *Journal of Applied Physics*, 114, 223902, 2013.

[119] S. G. G.-B. Moussy, M. Henriot, M.-J. Guittet and M. Gautier-Soyer. “Atomic-oxygen-assisted MBE growth of Fe_3O_4(111) on α-Al_2O_3(0001)”. *Surface Science*, 482-485, 809, 2001.

[120] M. Lübbe, A. M. Gigler, R. W. Stark and W. Moritz. “Identification of iron oxide phases in thin films grown on Al_2O_3(0001) by Raman spectroscopy and X-ray diffraction”. *Surface Science*, 604, 679, 2010.

[121] K. P. McKenna, F. Hofer, D. Gilks, V. K. Lazarov, C. Chen, Z. Wang and Y. Ikuhara. “Atomic-scale structure and properties of highly stable antiphase boundary defects in Fe_3O_4”. *Nature Communications*, 2014.

[122] W. Eerenstein, L. Kalev, L. Niesen, T. Palstra and T. Hibma. “Magneto-resistance and superparamagnetism in magnetite films on MgO and $MgAl_2O_4$”. *Journal of Magnetism and Magnetic Materials*, 258, 73, 2003.

List of Figures

List of Tables

Acknowledgments

At this point i would like to thank all of those people who supported me during my time as PhD student and the production of my thesis.
First, I would like to thank my doctoral adviser Prof. Dr. Joachim Wollschläger for giving me the opportunity to write my dissertation in his group. I am certainly grateful for his tireless support and his enduring patience for an exceptional long time. I would also like to thank the other three members of my examination board Prof. Dr. Jochen Gemmer, Dr. Karsten Küpper and especially Prof. Dr. Heinz-Jürgen Steinhoff, who adopt the secondary advisory part of my thesis.
Special thanks go to my former Bachelor students Nico Pathé and Andreas Krampf who contribute a huge part to my thesis by doing their own research. This thesis would not be the same without your personal and scientific engagement and it was a pleasure to work with you.
My research also benefited from the help of several other members and ex-members of my workgroup. Especially, Frederic Timmer, Olga Kuschel, Dr. Timo Kuschel, Dr. Daniel Bruns, Christian Otte, Dr. Karsten Küpper, and Dr. Florian Bertram should be mentioned here. Besides the assistance during measurements and helpful disussions, i am also grateful for your help with repairs of the UHV chambers and some after work activities. You make my workplace a second home.
Thanks to Dr. Timo Kuschel who handed over to me his MOKE setup and knowledge which lay the foundation for my scientific research. I also thank Manuel Langer from the HZDR who also contribute some valuable FMR calculation to understand the magnetic anisotropy of my samples. For their excellent technical support in Osnabrück i would like to thank Gregor Steinhoff from our group as well as the mechanical and electrical workshops for their excellent technical support.
In the end, I would like to thank my family and friends, especially Corinna, for their support during the time of my thesis.

Erklärung

Hiermit erkläre ich an Eides statt, die vorliegende Abhandlung selbstständig und ohne unerlaubte Hilfe verfasst, die benutzen Hilfsmittel vollständig angegeben und noch keinen Promotionsversuch unternommen zu haben.

Osnabrück, 16.11.2016
Tobias Schemme